Studies on Magnetically Actuated Droplets for Digital Microfluidic

Author

Khaw, Mei Kum

Published

2017

Thesis Type

Thesis (PhD Doctorate)

School

Griffith School of Engineering

DOI

10.25904/1912/1837

Studies on magnetically actuated droplets for digital microfluidic

A Ph.D. thesis

submitted to

Griffith School of Engineering

Griffith University

Brisbane, Australia

by

Mei Kum Khaw

B.Sc., M.Eng.Sc.

Submitted in fulfilment of the requirements of the degree of

Doctor of Philosophy

December 2016

To my husband, daughter and the little one in my tummy

Acknowledgements

First and foremost, I would like to thank my principal supervisor, Dr Faisal Mohd-Yasin. It has been an honour to be his student for both my Masters and Ph.D. I am thankful for his guidance, encouragement and useful critiques of my research work. The positiveness in him was motivational for me, especially during tough times during my candidature. Thank you so much for opening up my mind to look at my research in different ways.

I also would like to express my appreciation and gratitude to my associate supervisor, Professor Dr Nam-Trung Nguyen. I appreciate all his contributions of time, ideas and feedbacks to help me with the experiments and paper writing. He has taught me how to collect meaningful experimental data and the right way to write a research paper. With his tight schedule, he managed to slot me in for a one-to-one meeting every week to motivate and help with my research progress. I want to thank you again and again from the bottom of my heart.

To my friends in Room 1.11 at Queensland Micro- and Nanotechnology Centre (QMNC), thank you for listening, advising, supporting me and most importantly keeping me sane throughout our Ph.D. journey. You know who you are. Special thanks to Chin Hong Ooi for helping me with the Matlab software, camera settings and providing feedbacks in my floating marble experiment.

Next, I would like to thank the staffs at QMNC for providing me support in terms of administrative paper works, help with equipment, health and safety documentation and the social gatherings. Thank you Lacey Shaw, Kerryn Iacopi, Kien Chaik (Danny), Anthony and Alan Iacopi.

Heartfelt thanks to Penny & Mark Deards and also Vandy & Frances Mau for their love, kindness, support and motivation during my years in Brisbane. Thanks for checking on me from time to time and also to shower me with home-cooked food and warm welcome to their homes.

Last but not least, I would like to thank my beloved family: my husband, daughter, parents and in-laws. Thank you for supporting me emotionally and mentally during my pursuit of Ph.D. It has been a tough time being away from home. Sorry for not being able to perform my full duties as a wife, mother and daughter while being here in Brisbane. But we strived through it all. I owe it to all of you.

Statement of Originality

This work has not previously been submitted for a degree or diploma in any university. To the best of my knowledge and belief, the thesis contains no material previously published or written by another person except where due reference is made in the thesis itself.

Author's signature

14th December 2016

Date

Table of contents

Abstract

Digital microfluidic is an emerging liquid handling technique where discrete droplets are manipulated on a substrate. For the past decades, conventional microfluidic applications are based on continuous flow concept. They require complicated networks of channels, pumps and valves to manage the flow of droplets in microchannels. In digital microfluidics, droplets are moved individually on an open surface. The droplets have the flexibility to move in various directions, making a single device flexible for diverse reaction designs and applications. The manipulation of discrete droplets allows reduction in sample size, faster heat transfer and reaction rates and easier collection of samples. The droplets can be manipulated via electrostatic force, magnetic force, gravitational force, pressure gradient, pH change, surfactant concentration, temperature change, Marangoni propulsion and light-induced surface tension gradient.

Magnetic actuation is an excellent candidate for digital microfluidic applications because of the simplicity of using external magnetic field for a non-contact and non-invasive control over magnetised droplets. The magnetic field can penetrate through substrates and biological materials. There is also a wide variety of available magnetic particles and it is easy to control the amount of magnetic particles loaded into the carrier liquid. Some magnetic particles can absorb nucleic acids and other biomolecules making it possible for biomolecular separation. Magnetic manipulation is not affected by factors such as surface charges, pH and ion concentration. In most cases, magnetic manipulation does not induce heating.

One of the major concerns of manipulating droplet on solid surfaces is the wetting phenomena of liquid. Droplets are formed on solid surface using the surface tension properties of fluid. Most liquids wet the surface. When the stationary droplet moves, it leaves a trail on the surface causing a loss in its volume and content. To prevent the wetting phenomena on the solid surface, methods such as producing superhydrophobic surfaces and liquid marbles are introduced. Liquid marbles even allow for manipulation on a liquid based platform. In this thesis, we coated the solid surface with a layer of polytetrafluoroethylene (PTFE) that repels water. The modification of the solid surface promotes air trapping between the droplet and the surface. A liquid marble is typically an aqueous solution encapsulated by a coating of hydrophobic microparticles such as PTFE powder. The microparticles are attracted to the liquid-air interface and form a coating that isolates the liquid in a marble from the external surface it is resting on by an air layer. On a solid surface, a liquid marble can roll or slide around without wetting the surface. On a liquid surface, the liquid marble floats and slides with minimum friction. A liquid marble has a lower evaporation rate as compared to a non-coated free droplet.

Although the gas exchange within the liquid marble and surrounding environment cannot be avoided, the volume of a liquid marble can be maintained by changing the humidity and temperature of its surrounding. This characteristic makes liquid marbles suitable to serve as a cell culture platform and sensing applications. In this thesis, we studied the magnetic actuation of reactive microdroplets on the hydrophobic solid surface and also unreactive floating liquid marbles on various aqueous solutions.

In our first work, a microdroplet containing hydrochloric acid (HCl) solution mixed with iron oxide was magnetically-actuated by an external permanent magnet to merge with a sessile droplet containing a sodium hydroxide (NaOH) solution on a hydrophobic surface. Magnetically-controlled optimized actuation of those reactive microdroplets that allows faster mixing is needed for the detection of the heat released from an exothermic reaction. The coalescence of both droplets produces an exothermic reaction, which releases a detectable heat of neutralisation. We studied the effects of volume of the droplets, the speed and the concentration of iron oxide to the mixing time and the amount of the heat being released. The experimental results indicated that a lower volume of droplet and a higher speed of magnet led to a shorter mixing time. We also calculated the enthalpy values based on the measured peak temperature of the heat. Finally, we found the suitable operating conditions of this system for microcalorimetric measurement of exothermic HCl-NaOH droplets.

The next part of our work was on the magnetic-actuation of floating liquid marbles filled with iron oxides. Controlled actuation of a floating liquid marble is a potential digital microfluidics platform for the transportation of aqueous solution with minimal volume loss. Despite this potential, the capability and the dynamic behaviour of the magnetic actuation of liquid marbles on liquid surfaces has not been fully investigated. First, we investigated the sliding motion of the marble. The magnetic force and the frictional force acting on the floating liquid marble determined the horizontal movement of the marble. We varied the magnetic flux density, flux density gradient, concentration of iron oxides and the speed of the marble to elucidate the relationship between the acting forces. We subsequently determined the suitable operating conditions for the actuation and derived the scaling laws for the actuation parameters.

In our further work on the floating liquid marble, we investigated how the frictional force, inertia and effective surface tension of the marble affect the damping of the marbles when the driving magnetic force was removed. We varied the viscosity of the medium where the marble floated on, speed and the volume of the marble. We related our findings to the underdamped harmonic oscillation model. We used the experimental results to determine the viscous damping coefficient and magnetic force constant which were then used to evaluate the friction correction factor to the Stokes drag. We also estimated the value of the driving magnetic force. We

correlated the friction correction factor and frequency of damping to the effect of viscous force to the surface tension of the medium and the marble.

Chapter 1: Introduction

1.1 Digital Microfluidics

Microfluidic is a field of fluid handling technique for samples in the range of picoliter to microliter-size. There are 3 main types of microfluidic system. Conventional microfluidic systems are based on continuous liquid flow through microfabricated channels as shown in Figure 1.1(a). This system requires external mechanical pumps and valves to actuate the flow in a closed-channel. The microchannel is typically 10 – 100 µm in diameter and fabricated mainly using soft-lithography method [1]. This conventional type of microfluidic is suitable for biochemical applications which do not require a high degree of flexibility.

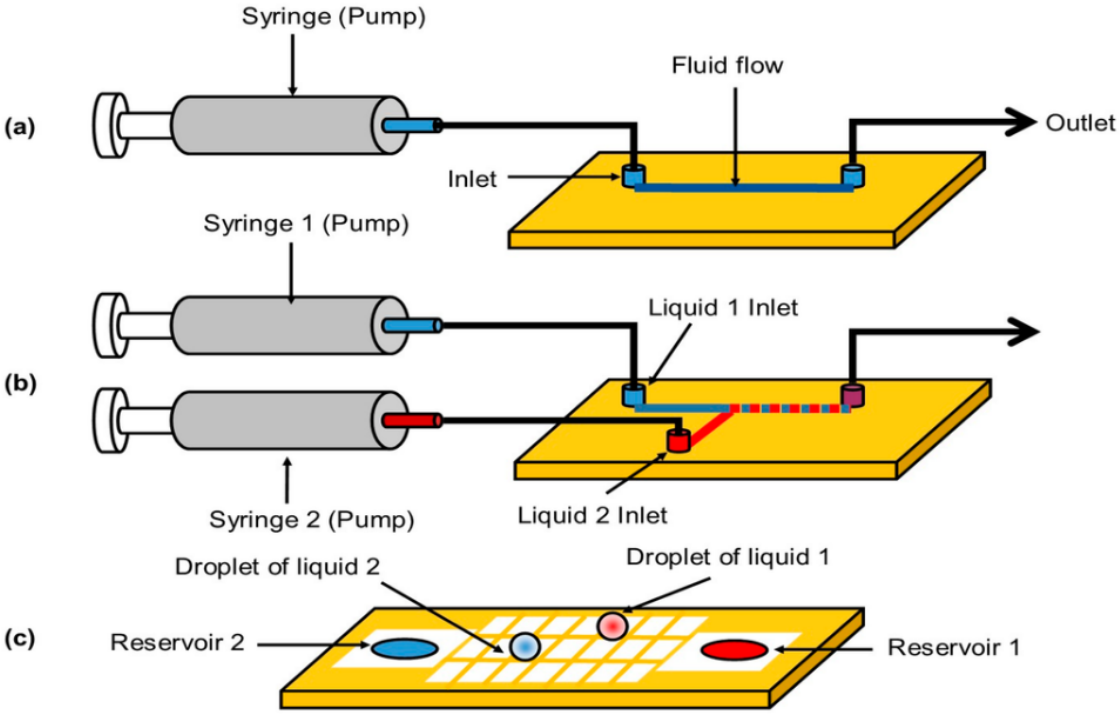

Figure 1.1: Types of microfluidic system, (a) continuous flow (b) droplet-based and (c) digital [2]

The second type is the droplet-based microfluidic system. It is also implemented in a microchannel device. The first generation of this system utilized the continuous flow of two or more fluid interconnected at a junction to produce individual droplets which are isolated from one another using immiscible fluid as shown in Figure 1.1(b). In order to eliminate the need for continuous flow, the programmable external pump is now capable of generating discrete droplets which are separated by immiscible oil. Microdroplets can be brought together in a specific sequence, mixed and dispersed under the control of the channel network by using electrokinetic and hydrodynamic pump. The benefit of droplet-based microfluidic is the

reduction in volume consumption, improvement in mixing and is suitable for high throughput experiments.

Digital microfluidic is the new emerging technique of the droplet-based microfluidic system. Instead of having continuous flow of droplets in microchannels, digital microfluidic offers an open concept of the manipulation of discrete droplets. Droplets are moved individually to mix, split, merge and dispense from its reservoir as shown in Figure 1.1(c). There is not a need for complicated networks of channels, pumps and valves. Since droplets are not confined in a closed channel, the droplets have the flexibility to move in various directions, making a single device flexible for diverse reaction designs and applications.

The manipulation of discrete droplets allows for further reduction in sample size, faster heat transfer and reaction rates and easier collection of samples. Digital microfluidic also can be performed in a simple and compact design. The most common digital microfluidic systems actuate the droplets on an array of electrodes using the electrowetting-on-dielectric (EWOD) technique [3-5] as shown in Figure 1.2. This system has been used for biosensing and microcalorimetric application because it is possible to achieve high throughput through parallel processing of numerous samples on the same chip at the same time.

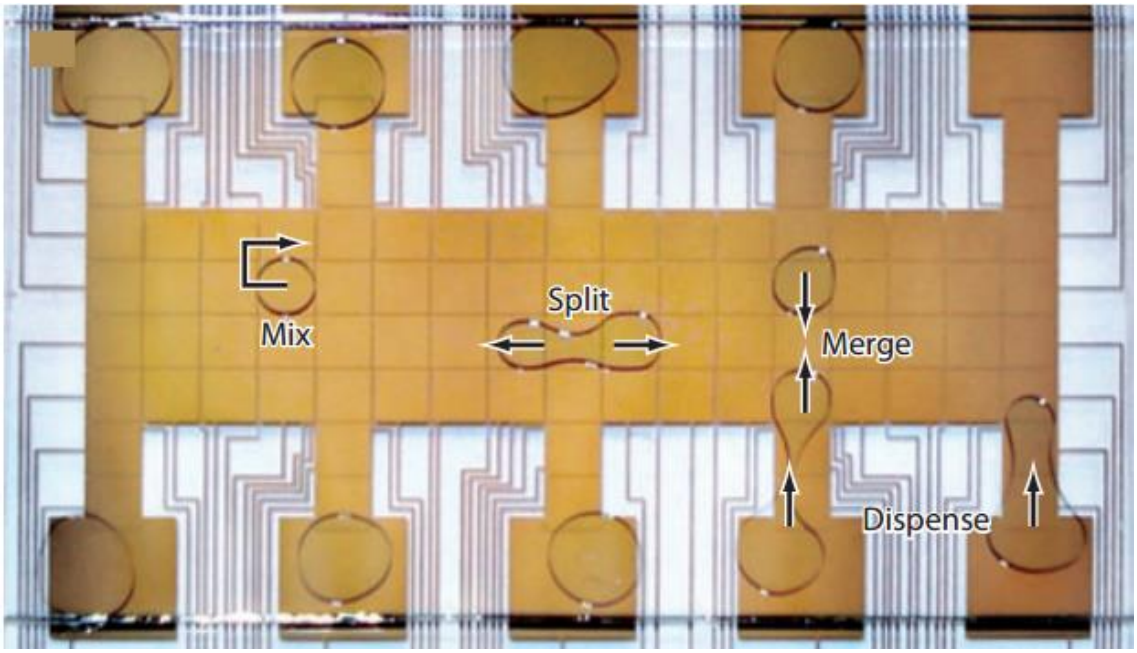

Figure 1.2: Manipulation of droplets using electric field [3]

Forces that contribute to the droplet's movement are the driving force and the resistive force. The droplets can be manipulated via electromagnetic schemes, mechanical schemes or chemical schemes such as pH change, surfactant concentration and temperature change.

One of the main concerns of manipulating droplets on solid surfaces is the wetting phenomena of liquid. Droplets are formed on solid surface using the surface tension properties

of fluid. Most liquids wet the surface. When the stationary droplet moves, it leaves a trail on the surface causing a loss in its volume and content. The EWOD technique as seen in Figure 1.2 involves modifying the surface tension of liquids on a solid surface using a voltage. For other types of manipulation schemes, there are methods suggested to prevent the wetting phenomena on the solid surface. The method includes producing superhydrophobic surfaces and liquid marbles.

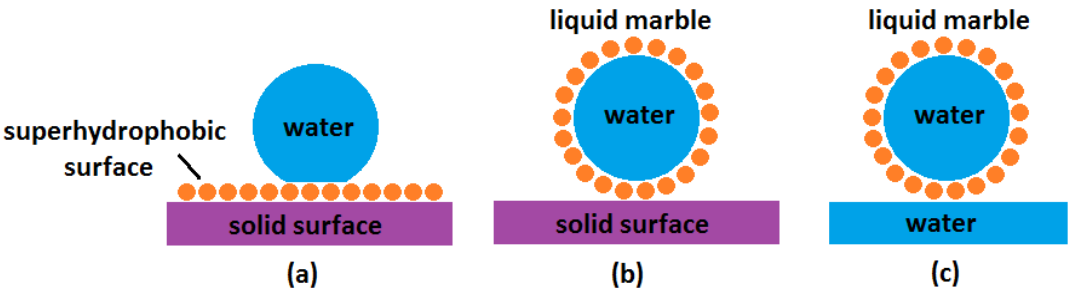

Figure 1.3: (a) Water droplet on superhydrophobic surface and water coated with hydrophobic microparticles (liquid marble) on (b) solid surface, (c) water

A superhydrophobically modified surface is coated with a layer that repels water. A study on the natural water-repelling surface of the lotus leaf [6] gives insight to the engineering of this anti-wetting surface. The modification of the solid surface promotes air trapping between the droplet and the surface as shown in Figure 1.3(a). This results in an increase in the apparent contact angle between the droplet and the surface. Numerous methods are available for producing superhydrophobic surfaces [7-9] which will be explained in detailed in Section 2.3. As an example, Koh et. al. [10] spin-coated a sterilised and treated Pyrex glass wafer with non-wetting polytetrafluoroethylene (Teflon) solution to create a thin layer of approximately 200 nm Teflon coated wafer.

A liquid marble is typically an aqueous solution encapsulated by a coating of hydrophobic colloidal microparticles. The microparticles are attracted to the liquid-air interface and form a coating that isolates the liquid in a marble from the external surface it is resting on by an air layer [11, 12]. The surface can be a solid surface as shown in Figure 1.3(b) or the free surface of another aqueous solution as shown in Figure 1.3(c). On a solid surface, a liquid marble can roll or slide around without wetting the surface [13]. On an aqueous free surface, the liquid marble floats and slides with minimum friction [12, 14, 15]. Figure 1.4 shows the coating of a water droplet with the Teflon powder.

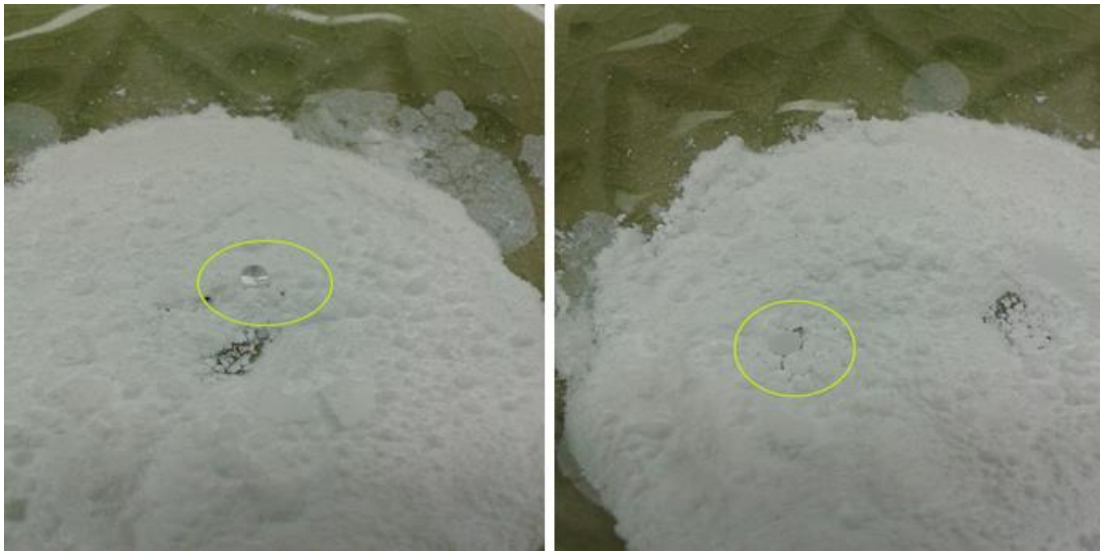

Figure 1.4: Left: A droplet is micro pipetted in a bowl of Teflon powder and rolled around. Right: Droplet after thorough coating with the powder

1.2 Motivation of this study

Based on the different manipulation schemes of fluid in the digital microfluidic system, we have picked to study the magnetically-actuated scheme of droplets on hydrophobic surface and liquid marbles floating on water and aqueous solutions of various viscosities.

A liquid marble has a lower evaporation rate as compared to a non-coated free droplet [16, 17]. Although the gas exchange within the liquid marble and surrounding environment cannot be avoided, the volume of a liquid marble can be maintained by changing the humidity and temperature of its surrounding. This characteristic makes liquid marbles suitable to serve as a cell culture platform [18-21] and sensing applications [22, 23]. Vadivelu et al. used a floating liquid marble as a bioreactor for growing three-dimensional cell spheroids [19]. The floating liquid marble allows the cells to freely associate and interact to produce uniform sized spheroids. The quality of the spheroids depends on the internal mixing process, which in turn depends on the motion of the marble over the surface of the supporting liquid. Moving the marble around would induce internal flow and mixing. One of the motivations for this work is the development of a controllable magnetic actuation scheme for the floating liquid marble leading to a practical digital microfluidics platform.

Furthermore, the development of digital microfluidic system is a promising trend in the design of open chamber microcalorimeters. Microcalorimeters are efficient tools to measure the heat of chemical reactions of small biological samples. Most protein samples are costly and often not available or reproducible. In the pharmaceutical industry, microcalorimeters are used

in the early stages of the small molecule drug discovery process, also known as the fragment-based drug discovery (FBDD). Microcalorimeters determine whether the process heat from the binding interactions between the small molecules of the drug candidate and the target proteins from the disease corresponds with the assumed metabolic pathways. Detection of unknown reactions is also possible. In the drug discovery laboratory, microcalorimetry sensing of the protein (disease) and ligand (drug) is one of the initial steps to determine the enthalpy, entropy, free Gibbs energy and binding affinity. Subsequently, the merged samples are picked up by a micropipette to be sent to a mass spectrometer to verify the binding affinity. A suitable microcalorimeter for this application should be a simple and flexible array setup that could perform the calorimetry function and also easily picked up by a micropipette. Thus, the study of heat transfer of two reacting coalesced droplets is important for the design of such system. In the study of heat transfer, the mixing time of the samples is an important consideration. The sample droplets should be completely mixed within a specified time frame to allow the sensitive detection of the total heat release. Therefore, rapid mixing between the two fluids is required. A controlled magnetic actuation of the droplets will determine the optimum mixing speed with the highest amount of heat released.

1.3 Research Objectives

The main objective of this work is to study the manipulation of magnetic-actuated microdroplets on hydrophobic solid surface and also floating on an aqueous solution possible for applications in microbioreactors for three-dimensional cell cultures and microcalorimetric measurement. The breakdown of the objectives includes:

- Investigate the mixing time and enthalpy of magnetically-actuated reacting droplets on a hydrophobic surface. We experimentally investigate the effect of the volume of droplets, the speed of the driving permanent magnet and the volume concentration of magnetic particles towards the mixing time and the amount of the exothermic heat. Finally, the enthalpy values are evaluated based on the measured peak temperature. The outcome of this study will be used as a basis for the design of a low-cost droplet-based polymeric microcalorimeter.

- Investigate the sliding motion of a magnetically actuated floating marble on water. We experimentally evaluate the parameters that affect the motion of a floating liquid marble in terms of displacement and velocity such as the volume concentration of magnetic particles, the speed and the flux density of the driving permanent magnet. With these data, we can then determine the suitable operating conditions for the actuation as well as the critical

points where the liquid marble no longer follows the permanent magnet. The scaling relationship of the operation parameters is determined.

- Investigate how the frictional force, inertia and effective surface tension of a floating liquid marble affect the damping of the marbles when the horizontal driving magnetic force is removed. The variable parameters are the viscosity of the medium in which the marble floats on, speed and the volume of the marble. We can relate our findings to the underdamped harmonic oscillation model. From the experimental results, we determine the viscous damping coefficient and magnetic force constant which can then be used to evaluate the friction correction factor to the Stokes drag and the damping ratio. From the value of the magnetic force constant, the driving magnetic force can be estimated quantitatively.

1.4 Thesis outline

Types of microfluidic system were introduced in this chapter. We have further discussed about the emergence of digital microfluidic system that is well-suited for high-throughput applications such as bioreactors, biosensing and microcalorimeters. Chapter 2 of this thesis will review in more detailed the manipulation schemes of the microdroplets particularly the magnetic actuation methods that are reported in the literature. Literature review on the magnetic actuations on solid hydrophobic platform and liquid marbles on hydrophobic platform and aqueous solution are discussed.

Chapter 3 outlines the experimental setups and design methods for magnetic actuation of 2 main types of platforms. We start with the magnetic actuation of uncoated droplets on a solid hydrophobic surface. The droplets are chemically reactive and also non-chemically reactive. This is followed by the investigation of the sliding motion of a magnetically actuated floating liquid marble on water. Subsequently, we do a further work on the floating liquid marble by varying the viscosities of the medium the marble floats on by adding in various concentrations of glycerol. We will investigate the effects of frictional force, inertia and effective surface tension of the marble on the damping of the marble when the driving magnetic force is removed.

We will analyse and discuss the results in Chapter 4 and 5 respectively. We will conclude in Chapter 6 with the key findings from the Ph.D. study, together with recommendations for future work.

1.5 Publications and conference presentations related to the thesis

Journal articles/manuscripts:

1. Khaw, M. K., Mohd-Yasin, F., & Nguyen, N. T. (2016). Microcalorimeter: Design considerations, materials and examples. *Microelectronic Engineering*, *158*, 107-117.

2. Khaw, M. K., Ooi, C. H., Mohd-Yasin, F., Vadivelu, R., St John, J., & Nguyen, N. T. (2016). Digital microfluidics with a magnetically actuated floating liquid marble. *Lab on a Chip*, *16*(12), 2211-2218.

3. Mei Kum Khaw, Chin Hong Ooi, Faisal Mohd-Yasin, Anh V. Nguyen, Geoffrey M. Evans and Nam-Trung Nguyen. Dynamic behaviour of a magnetically actuated floating liquid marble. (has been accepted for publication in Microfluidics and Nanofluidics journal).

4. Khaw, M. K., Mohd-Yasin, F., & Nguyen, N. T. Micro calorimetric measurement of an exothermic reaction in magnetically actuated droplets. (To be resubmitted after revision)

Conference presentations:

1. M.K. Khaw, C.H. Ooi, R. Vadivelu and N.T. Nguyen, "Magnetic Actuation of Floating Liquid Marble", 7th ANZNMF 2016 Symposium, 21st-23rd March 2016, Brisbane, Australia. Poster presentation.
2. M.K. Khaw, F. Mohd-Yasin, N.T. Nguyen, "Optimization of a mixing time of a magnetically actuated acid-base microdroplets for microcalorimetric measurement", Biosensors 2016, 25th-27th May 2016, Gothenburg, Sweden. Poster presentation.

Chapter 2: Literature review

2.1 Introduction

In this chapter, we first briefly discuss about the types of droplet manipulation schemes and the mixing techniques in the digital microfluidic technology. Then we will review specifically of the past works done on magnetically actuated schemes on superhydrophobic surfaces in Section 2.3. We include a review paper of the microcalorimeter's basic structures, design considerations, materials used and the design examples from the literature because part of our proposed work is a proof of concept for an open chamber polymer microcalorimeter employing magnetically actuated droplets. In Section 2.4, we will introduce the liquid marble. As there is not much intensive work done on the magnetically actuated liquid marble, we first review the development of the liquid marble on solid surfaces and aqueous solution. Then, we proceed to the works done on liquid marble under the influence of the magnetic field for the past 10 years.

2.2 Overview of manipulation/mixing techniques

In Section 1.1, digital microfluidic was introduced as an emerging liquid handling technology. The digital microfluidic platforms that will be highlighted in this work are droplet on superhydrophobic surface (Figure 2.1 (a)) and droplet coated with hydrophobic microparticles (liquid marble) on aqueous solution of different viscosity (Figure 2.1(b)).

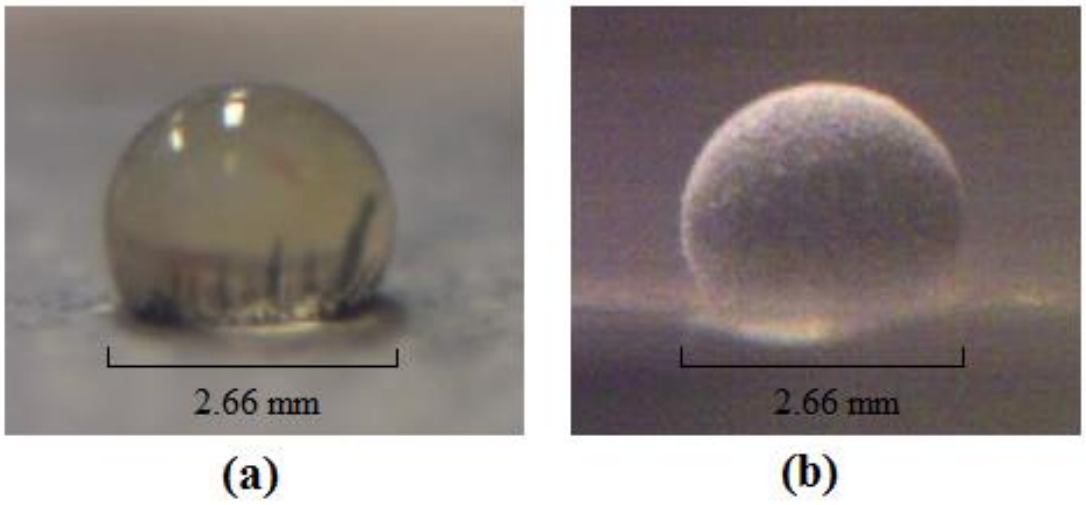

Figure 2.1: Images of (a) droplet with magnetic particles on a superhydrophobic surface and (b) liquid marble with magnetic particles coated with PTFE powder floating on an aqueous solution.

2.2.1 Types of manipulation

The discrete droplets can be manipulated via electrostatic force, magnetic force, gravitational force, pressure gradient, pH change, surfactant concentration, temperature change, ultrasonic, organic solvents, Marangoni propulsion [24] and light-induced surface tension gradient [25]. The first 3 schemes are the common ones that have been actively implemented on droplets on the digital microfluidic platforms. We will discuss about the manipulations and its development in Section 2.3 and 2.4.

2.2.2 Mixing techniques

Mixing techniques are introduced in this section because they play an important role in digital microfluidics where chemical reactions are involved such as in a microcalorimeter. Mixing that is induced entirely by merging of droplets leads to a rather large mixing time because diffusive mixing dominates. This method would only be suitable and adequate for simple measurement of the total enthalpy for some biological reactions. In order to perform the full kinetic characterization of enzymatic reactions, their droplets must be thoroughly mixed to substantially reduce the mixing time. There are two basic types of mixing: active and passive. Active mixing relies on the energy supplied by external sources to enhance the mixing rate, whereas passive mixing relies on improved geometric features to accomplish the same objective. In order to quantify and to have full control of the manipulation of the droplets, an active mixing is preferred. In terms of active mixing in microdroplets, the most notable concepts include electrostatically-actuated mixing, magnetically-actuated mixing and magnetic micro-stirring.

2.2.2.1 Electrostatically actuated droplet mixing

Electrostatic method [26, 27] employs two electrodes to mix the droplets. Droplets of different samples are separately micropipetted into the reaction chamber. When the droplets come to thermal equilibrium, the two samples merge and mix isothermally. The separation of the sample delivery and mixing can minimise heat losses during delivery. Further uncertainty can happen due to the additional heat from the kinetic energy of the samples during delivery. Figure 2.2 is the specific example of electrostatic mixing by Torres et al. [26]. It showed the electrostatic merging of two 500 nL droplets of water at three different times. Initially, the undyed droplet was placed asymmetrically across a 50 μm gap (shown as a white line in the figure) between two electrodes on the device surface. A voltage of 100 V was applied across the gap to move the droplet until it covered equal amount of both electrodes. The dyed droplet was placed within the range of this motion and merged with the first droplet upon contact. 33 ms after applying the voltage, the droplets were merged. By 66 ms, the final mixture was formed. The combination of

the electrostatic force and the inertial force caused by the surface tension of the moving droplet provided a thorough mixing of the sample.

In order to eliminate effects of heat dilution and variations in the surroundings, a differential temperature measurement can be incorporated using adjacent reference mixing droplets. The reference droplets should be chosen to be equal in volume to the measured droplets. With this arrangement, the temperature of the samples under study is measured relative to the reference samples.

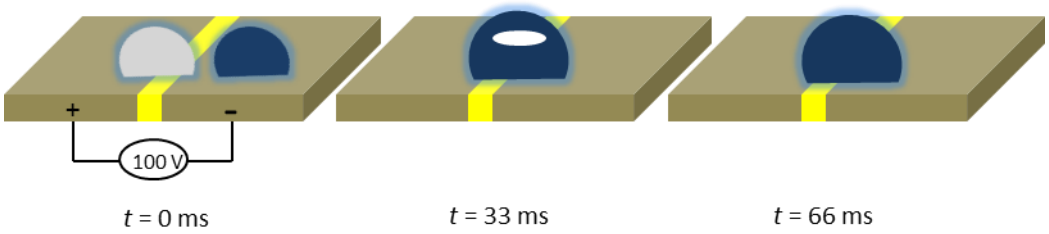

Figure 2.2: Electrostatic mixing and merging of two droplets [26]

2.2.2.2 Magnetically actuated droplet mixing

Magnet-actuated mixing [28, 29] utilises a droplet with embedded magnetic particles for mixing. The movement of this droplet is controlled by an external magnet. Figure 2.3 shows an example of this mixing concept, which was performed by Long et al. [29]. The oil-coated droplet with magnetic beads was transferred onto the glass slide through precise pipetting. First, the suspended magnetic particles in the aqueous droplet were attracted to the bottom of the droplet by the magnetic force. The magnet was moved horizontally by a motorised linear stage. The particles follow the magnet until the two droplets merged. The magnet and the merged droplets were subsequently moved back and forth to mix the two liquids.

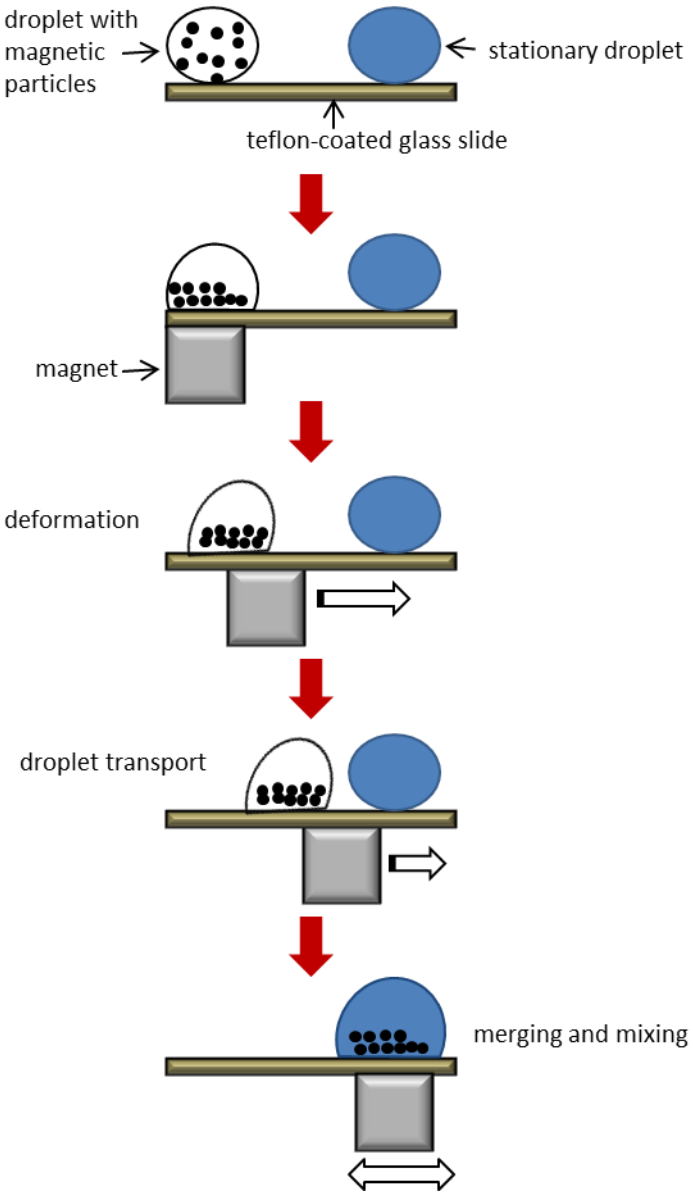

Figure 2.3: Magnetically-actuated mixing and merging of two droplets [29]

2.2.2.3 Magnetically actuated stirring

Magnetic micro-stirring [30, 31] is a combination of electrostatic-actuated mixing and magnetic stirring. Figure 2.4 shows the setup of the magnetic stirring, which was performed by De Bruyker et al. [30]. The stir bar was fabricated using laser micromachining. The bar was placed on the surface of the microcalorimeter's membrane. The stir bar was remotely activated by an externally rotating magnetic field at the bottom of the membrane. Initially, the droplets were merged by electrostatic mixing. Once both droplets merged, the stir bar was activated. The axis of rotation of the magnet was centred below the stir bar to reduce unwanted lateral motion of the bar and to prevent spreading of the droplets. In this particular work, the mixing times were 1.8 s

and 2.1 s with the stirring rate of 600 rpm and 1500 rpm, respectively. It was found that the stirring rate yield minimum difference in the mixing time. However, the difference in the mixing time using magnetically-actuated stirring and using electrostatic actuated mixing was large. The mixing time was 29.5 s with the latter method [30].

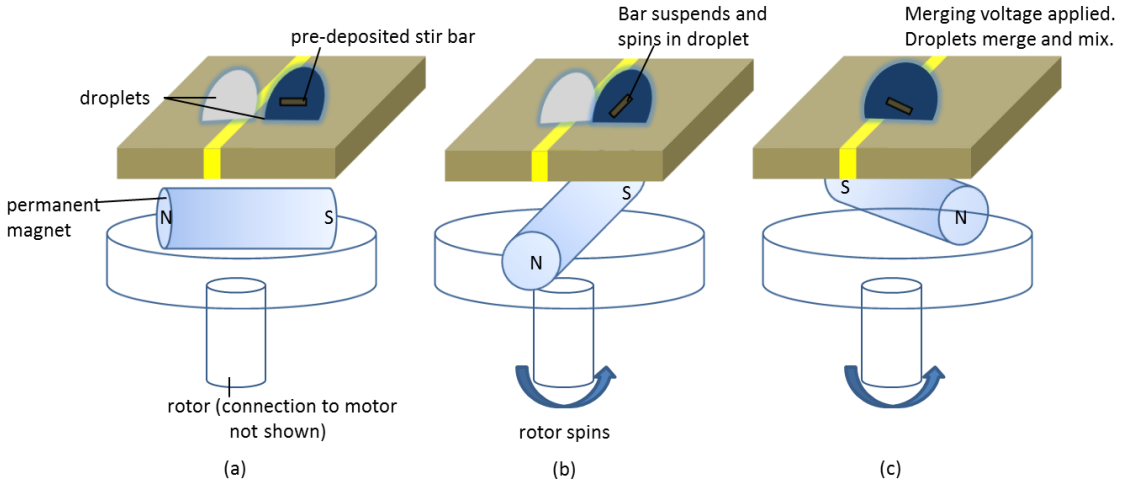

Figure 2.4: Magnetically- and electrostatically-actuated stirring of two droplets [30]

2.3 Magnetic actuation of the droplets on superhydrophobic surfaces

2.3.1 Non-reactive droplets

Several previous works have been reporting the kinematics and dynamics of the magnetically-actuated sessile droplet on an open hydrophobic planar surface. Egatz-Gomez et al. [32], Garcia et al. [33] and Schneider et al. [34] investigated the movement, coalescence and splitting of droplets on a hydrophobic surface. Magnetically-actuated droplets with size ranging from 5 µL to 35 µL were inserted with carbonyl iron particles coated with polysiloxane (to prevent oxidation). These studies varied the viscosity of the fluid, droplet volume and iron particles concentration. In another study, Long et al. [29] investigated the effects of particle type, droplet size, surrounding oil layer, surface tension and viscosity of a magnetic-actuated droplet on a Teflon-coated glass plate. The aqueous droplet was coated with silicon oil and contained magnetic beads. In a similar study around the same time, Roy et al. [28] investigated the effects on the rotational speed of the magnetic field, fluid viscosity and magnetic particle concentration on mixing of a dyed droplet. In the most recent work [35], the magnetically-actuated droplet was controlled by cyclic magnetic field created by four electromagnets using polystyrene/silica beads coated with a layer of super paramagnetic iron oxide. The mixing time decreased with the increasing current and frequency up to a critical frequency. Ohashi et al. [36]

developed a droplet-based polymerase chain reaction (PCR) device based on magnetic actuation of droplets containing magnetic beads in oil medium on top of a Teflon sheet.

Nguyen et al. [37, 38] and Beyzavi et al. [39, 40] had performed studies on the kinematics and deformation of sessile water-based non-reactive ferrofluid droplets under magnetic actuation. The ferrofluid droplets were liquid magnets and they were controlled by external magnetic field driven by planar microcoils. In their experiments, the ferrofluid was immersed in silicone oil on top of a thin Teflon layer. Using the same concept, Sun et al. [41] constructed a novel circular-motion closed-loop ferrofluid driven microchip for PCR. Nguyen et al. [42] further investigated the sliding motion of the ferrofluid droplets on Teflon-coated glass plate using a moving external magnet. This work provided the critical velocities of the actuated droplets with different the magnetic flux density induced by different permanent magnets. Furthermore, Koh et al. [10] demonstrated the use of magnetically actuated ferrofluid droplets as actuators for the key functions in digital microfluidics such as merging and mixing of other non-magnetic liquid droplets. The drawback of this work was that the whole droplet should be magnetic, for example using ferrofluid, such that the magnetic force is large enough to overcome the friction with the solid surface. Ferrofluid is not compatible with biological applications such as cell culture, thus using a minute number of magnetic particles mixed in the liquid could provide sufficient magnetic force for actuation and at the same time does not affect other components in the liquid.

2.3.2 Reactive droplets

To our best knowledge, no attempt has been made to study the coalescence of magnetically actuated reactive droplets. There were however previous studies on the passive mixing of chemically reactive droplets. Almarcha et al. [43] studied the chemical reaction of HCl and NaOH droplets and elucidated their reactions using the reaction-diffusion-convection model. Tsuji and Muller [44] studied the early stage of the chemical reaction of sodium hydroxide (NaOH) and Bromothymol Blue (a pH indicator) droplets. They reported the formation of fingers during the initial coalesced stage, which suggests that some type of instability of the chemical front occurs on the surface of the merged droplets. Heat conduction from the acid-base neutralisation caused the instability.

Recently, Yeh et al. [45] compared the mixing time of chemically-reactive droplets (alkaline solution and pH indicator) and non-reactive droplets. The droplets were passively mixed, and the experiment was performed on a surface with different wettability gradients. The mixing time of the latter is more than 100 times slower than the former. The evolution of the chemical reaction during the coalescence of the droplets was also studied.

2.3.3 Calorimeter for reactive droplets

(Adapted from review paper: Khaw, M. K., F. Mohd-Yasin, and N. T. Nguyen. "Microcalorimeter: Design considerations, materials and examples." *Microelectronic Engineering* 158 (2016): 107-117.)

This review paper was initially written to deepen our knowledge in the microcalorimeter's basic structures, design considerations, materials used and the design examples in the literature. Our experimental setup for this work is only a proof of concept for an open chamber polymer microcalorimeter employing our magnetically actuated droplets.

Calorimetry is an analytical science for determining the changes in heat of a system with its surroundings. Calorimeter devices measure the quantity of heat transferred to or from an object. It is an essential tool to characterise the thermodynamics of chemical reactions of a sample. A microcalorimeter is a miniaturized calorimeter, which makes possible the detection of the temperature changes of a small sample volume in the order of nanoliters (nL) down to picoliters (pL) regions. In order to take advantage of this capability, researchers normally employ an array of microcalorimeters, which consists of a number of parallel microcalorimeters. This system promises benefits such as high-throughput measurement, portability and low power consumption [46, 47].

One potential usage will be in the pharmaceutical industry, where an array of microcalorimeters can be used in the early stages of the small molecule drug discovery process, also known as the fragment-based drug discovery (FBDD). The detailed thermodynamic characterization is needed to screen drug candidates. A microcalorimeter can determine whether the process heat from the binding interactions between the small molecule (drug candidate) and the target proteins (disease) corresponds with assumed metabolic pathways. Detection of unknown reactions is also possible. Such system is sometimes referred to as an enthalphy array. It has potential to test tens of thousands of chemical compounds, while significantly shorten the screening time. Another advantage is in term of cost. Biological samples could be very expensive and are often not available or reproducible in large quantities [46, 47].

Calorimetric measurement can be categorised in term of temperature change (adiabatic or isoperibol), power compensation (isothermal) and heat conduction. The temperature-change microcalorimeter is the most direct way of measuring heat. The temperature sensor records the heat released (or absorbed) by the chemical reaction of the samples in the reaction chamber. The recorded calorimetric signal is the temperature of the reaction chamber as a function of time. With an appropriate electrical or chemical calibration, the energy equivalent to the reaction chamber can be determined. The measured temperature change is converted to a heat change by

multiplying the energy equivalent of the microcalorimeter (in cal/K) with the measured temperature change (in K) [48].

In a power compensation microcalorimeter, a heater controller keeps the temperature of the reaction chamber constant at all times. When a chemical reaction occurs in the microcalorimeter, the heater controller senses the temperature difference and applies power to regulate the chamber back to the initial temperature. The recorded power change (µcal/sec) is stored as a function of time. The heat change is calculated by integrating the power change of the heater over the time of measurement.

In a heat conduction microcalorimeter, a controlled heat sink keeps the reaction chamber at a constant temperature. The heat sink is coupled to the heat flow sensors. When the temperature changes due to a chemical reaction, the heat flow sensors will generate a voltage that is proportional to the temperature change.

2.3.3.1 Design Considerations

Four major components should be considered for the design of a microcalorimeter: reaction chamber, thermal insulation, fluid handling including mixing techniques, and temperature sensing. These components can be integrated in a single prototype.

A microcalorimeter is built on a membrane as the main structural and thermally insulating component (Figure 2.5). The choice of material for the membrane is often a thin film with low heat capacitance. A silicon or stainless steel rim supports the membrane. For temperature sensing, the thermometer is embedded within the membrane and is placed beneath the reaction chamber. The samples are delivered and mixed in the reaction chamber.

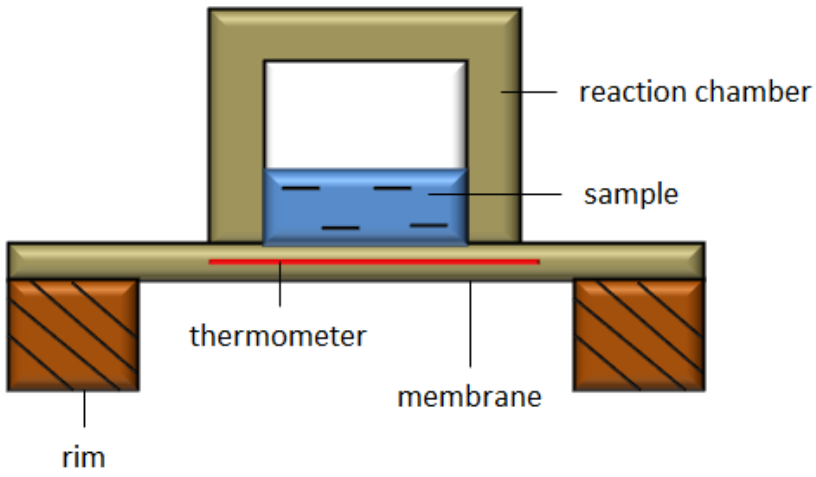

Figure 2.5: An illustration of a generic microcalorimeter [49]

The reaction chamber can be classified into two categories; open chamber [26, 27, 50-53] and closed chamber [54-60] as shown in Figure 2.6. The key difference is the method of fluid transfer. In the open chamber configuration, droplets of sample are directly delivered into the chamber via a micropipette or inkjet. In the closed chamber configuration, microfluidic channels are built-in to deliver the fluid sample. Conventional microfluidic channels are often bulky and are used to encapsulate the reaction chamber. Polymer thin film microfluidic channels are micromachined with the reaction chamber, giving an edge to miniaturisation and better thermal isolation.

Microcalorimeter can also be characterized in term of the delivery and treatment of the samples. There are three types: batch, flow and scanning microcalorimeter. For batch or titration microcalorimeters [51, 61], specific amount of samples are deposited to the reaction chamber and the change in temperature is measured. Therefore, microcalorimeters based on this approach employ the open reaction chamber. They are well-suited for measuring heat of reaction for protein-ligand binding, enzymatic activities and chemical mixture. On the other hand, flow microcalorimeters [54, 56-58] utilise the closed reaction chambers due to the need of microfluidic channels to deliver a continuous flow of samples. This is suited for continuous and real time monitoring of a chemical compound or heat production of living organisms. The scanning microcalorimeters, or better known as differential scanning calorimeter (DSC) [62-65] measure the heat capacity change of the sample through temperature scanning. In this third approach, the difference in the amount of heat required to increase the temperature of a sample and reference is measured as a function of temperature. This is important for the investigation of the internal structure or stability of samples in their original state. A DSC needs to be implemented in a closed chamber to avoid the evaporation of the sample while heating.

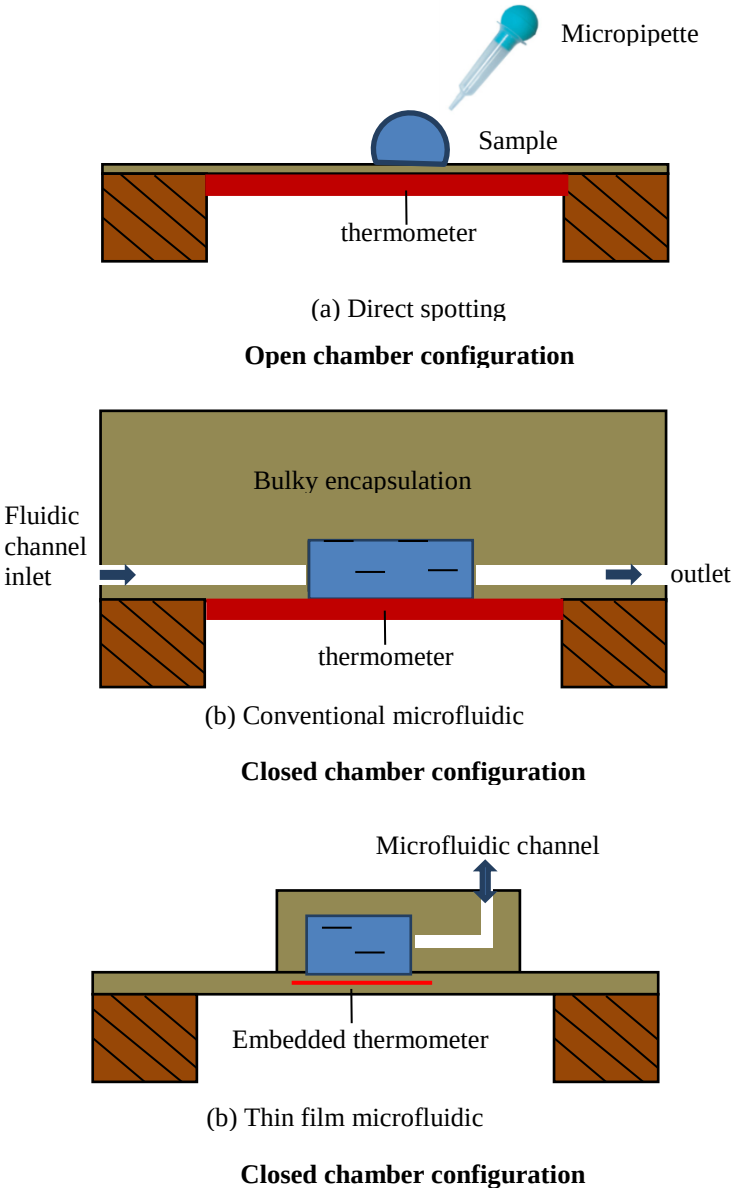

Figure 2.6: Two types of reaction chamber; open and closed [47]

Thermal insulation shields the heat of the reaction from the unwanted heat of its surroundings. In the case of a microcalorimeter, the reaction chamber is vulnerable to a substantial heat loss because of the larger surface-to-volume ratio. Furthermore, a small volume sample produces a very small amount of heat to be measured.

The four modes of heat transfer in a reaction chamber are conduction, evaporation, convection and radiation. Conduction is the dominant mode for all microcalorimeters. The thermal conduction path for the reaction chamber includes the air, membrane and electric leads in the temperature sensor circuitry [47]. Heat loss from the sample surface to the surrounding air is the main heat transfer path for the microcalorimeter. This type of heat loss contributes to more than 90% of the total thermal conductance. One solution for minimizing the heat conduction is to incorporate a vacuum chamber. However, a vacuum is only effective for solid

samples. Liquid samples in a vacuum will suffer significant mass loss due to evaporation [47]. This issue can be overcome by employing a microfluidic channel embedded in vacuum [54]. There are also microcalorimeters that incorporate the thermal shielding system [52] using low thermal conductivity materials [54, 56], which include polydimethylsiloxane (PDMS), polymethylmethacrylate (PMMA), parylene-C, SU-8 and polyimide.

The choice of the material and the structural design for the membrane are important to increase the thermal insulation, and hence, the sensitivity of the device. Sensitivity in this context means the ability to measure the actual heat released from the samples excluding the thermal influence from the surroundings. The comparison of materials in terms of their thermal properties is discussed in details in Section 2.3.3.2. The electric lead used in some temperature sensing device, for example the Wheatstone bridge, also provides heat loss that can be eliminated by reducing the cross-section of the electric leads.

Evaporation of sample is more evident in the open chamber microcalorimeters because of the lack of physical confinement. For the closed chamber configuration, the added microfluidic structure helps to prevent evaporation. Unfortunately, microfluidic designs have larger thermal conductance to their surroundings and have greater device heat capacity compared with the open chamber configuration. Microcalorimeters with microchannels are often moulded with PDMS [56, 57] or etched on bulk Si or SiO_2 substrates. The large heat capacity of the structure will absorb the heat from the small volume sample through conduction, leading to sensitivity reduction [47]. Heat loss through convection and radiation are usually not as significant as conduction and evaporation in microcalorimeters, and hence, will not be discussed in detail [47].

Fluid handling involves the methods of transferring sample to the reaction chamber. For the open-chamber configuration, samples are directly supplied to the reaction chamber through micropipettes or inkjet. Sample droplets range from a few μL to hundreds of pL. Micropipettes [50-52] are commonly used, but they are relatively slower than inkjets and cannot handle multiple samples simultaneously. Inkjets [53] can deliver batch-samples and is very fast. However, the speed causes large kinetic energy onto the samples, which generate additional heat. In an open chamber configuration, the inaccuracy of the temperature measurement due to evaporation and kinetic energy of the samples often reduces the performance of the system.

For the closed-chamber configuration, samples are transported via microfluidic channels. The advancement of microfluidic technologies allows microchannels and chambers to be embedded in the membrane. The example by Lee et al. is referred [54]. Their prototype handled fluid of 700 pL in volume with an accuracy of 50 pL. This was made possible by interfacing the parylene microfluidics channels on the calorimetry chip with pneumatically controlled PDMS

microfluidics chip for accurate reaction control. Figure 2.7(a) shows the overview of the microfluidic layout of the PDMS control chip and the calorimetry chip. Figure 2.7(b) shows the top view of the microfluidic channel on the membrane. The PDMS control chip contained valves and peristaltic pumps (red) to pump air for pneumatic control. The PDMS flow layer (blue) containing the fluid sample was connected to the parylene channel (black) of the membrane through an SU-8 via. Injection of the sample was done by sequentially closing adjacent valves to facilitate peristaltic pumping of the fluid. Parylene, PDMS and SU-8 are polymer materials often being used in microcalorimeter.

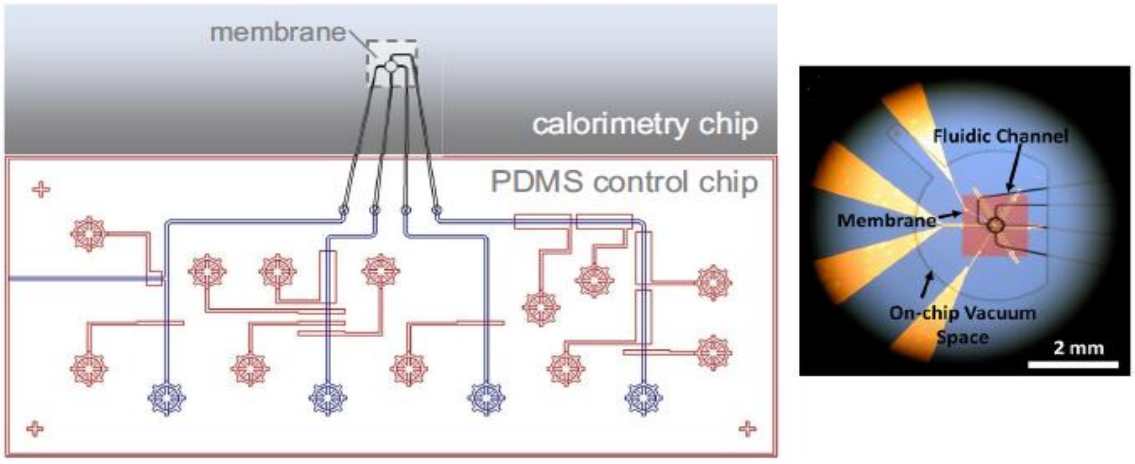

(a) (b)

Figure 2.7: (a) Microfluidic layout, (b) optical microscopy image of the reaction chamber and microfluidic channel [54]

Temperature sensing provides the mean for accurate temperature measurement in the reaction chamber. The sensitivity of the microcalorimeter is measured by the minimum thermal energy or power detected through the thermometer. The two common types of thermometers are thermistors and thermopiles. These thermometers are usually fabricated directly on the membrane. Three types of temperature sensor that have been implemented for microcalorimeters are discussed i.e. thermistor, thermopile and resistive-temperature detector.

Thermistors are temperature sensitive resistors that detect the change in temperature and convert to electrical resistance. The main advantage is the fact that thermistors can measure absolute temperature. Since thermistors rely on electric current to measure resistance, precautions must be taken to avoid overheating that will cause the rise of the temperature in the reaction chamber. This heating effect must be offset when calibrating the chip calorimeter. There are three notable works [26, 27, 66] that employed thermistors in their microcalorimeters.

On the other hand, thermopiles measure temperature difference between two areas at thermocouple junctions and convert it to electric voltage. Although they can only measure relative temperature, thermopiles have higher sensitivity than thermistors because of the absence of an electrical current. Due to this factor, thermopiles have excellent common-mode thermal noise rejection ratio and zero offset. Many groups that design microcalorimeters used thermopiles in their implementation [51, 53-56, 58, 60, 67-72]. The sensitivity and the signal-to-noise ratio can be further improved by increasing the number of thermocouples connected in series. However, an array of microcalorimeters has to limit the numbers of thermocouple junctions that can be placed due to the limited size. Nevertheless, thermopiles are more suited for miniaturization compared to thermistors. Thermocouples can be formed from bimetallic microjunctions. They allow low temperature processing, which is suitable for polymer membranes. Common bimetallic microjunctions are Au-Ni [50, 54], Cr/Ni [58], Ti/Bi [53] and Cr/Cu [71].

Davaji et. al [59] used a resistive temperature detector (RTD) in their microcalorimeter. RTD works on the similar principle as thermistor. The difference between RTD and thermistor is that the former uses metallic element such as platinum, nickel, copper and nickel-iron. Thermistor generally uses ceramic or semiconductor devices. The RTD temperature sensor's advantages over thermocouples are high accuracy, stability, linearity, reproducibility and ease of fabrication [59]. However, thermistors typically achieve a higher precision within a smaller range of temperature compare to RTD.

Device sensitivity indicates how precise the output is able to detect the changes when the temperature of the sample-under-test varies. In general, the sensitivity of the microcalorimeter increases when it can avoid heat loss in its reaction chamber. Also, a temperature sensor embedded into the microcalorimeter must be able to accurately measure the heat reaction by minimising unwanted noise. Several groups [26, 27, 58, 59, 72] reduced the common-mode noise of their prototypes by employing a differential scheme. The temperature sensors on both the measurement and reference areas are connected in a Wheatstone bridge configuration. Using this scheme, the measured temperature change of the sample reaction was compared against the reference temperature. This method effectively cancelled out associated background drifts in temperature since the reference sample interacted with the surroundings and underwent mixing simultaneously with the sample-under-test.

2.3.3.2 Materials

Table 2.1: Comparison of materials commonly used in microcalorimeters in terms of processing methods, mechanical stability, biocompatibility and chemical resistance

Materials	**Representative processing methods** [73]	**Mechanical stability**	**Biocompatibility**	**Chemical resistance**
Si	Bulk micromachining and surface micromachining	High Young's modulus but brittle	Good [74]	Excellent
Si_3N_4	Low Pressure Chemical Vapour Deposition (LPCVD)	Superior resistance to mechanical stress	Good [75]	Excellent
PDMS	Replica Moulding [76]	Low Young's modulus	Excellent	Not for organic solvents
PMMA	Laser machining, Injection moulding, x-ray exposure, hot embossing	High Young's Modulus	Excellent	Good [77]
Parylene-C	Chemical Vapour Deposition (CVD)	High mechanical strength.	Excellent	Excellent
SU-8	Photolithography [78], spin coating [56]	Low Young's modulus	Excellent	Excellent
Polyimide	Spin coating, extrusion	High tensile strength	Excellent	Excellent

Table 2.2: Thermal properties of the materials commonly used in microcalorimeters, compared with other materials. [47, 79]

Materials	**Thermal conductivity (W/m.K)**	**Specific heat (J/g.K)**
Si	130	0.71
Si_3N_4	15-30	0.70
PDMS	0.15	1.46
PMMA	0.19 – 0.24	1.46 – 1.47
Parylene-C	0.082	0.71
SU-8	0.20	1.50
Polyimide	0.12	1.09
Water	0.58	4.20
Air	0.026	1.01
Stainless steel, austenitic grade	11-16	0.45-0.55

Gold	315	0.13
Nickel	90.7	0.44

Table 2.1 lists the material candidates for making microcalorimeters and their processing methods, mechanical stability, biocompatibility and chemical resistance. Table 2.2 shows their thermal properties.

Generally, the membrane of a microcalorimeter is made of silicon (Si) or other silicon dielectric materials such as silicon nitride (Si_3N_4). These materials have relatively high thermal conductivities, small thicknesses (a few hundred nm) and relatively good insulation. Furthermore, silicon nitride (Si_3N_4) has excellent mechanical properties with good corrosion and oxidation resistance. It also has good thermal stress resistance due to the low coefficient of thermal expansion.

However, in terms of thermal insulation, polymer membranes are better. The polymers that are commonly used in microcalorimeters are PDMS, PMMA, parylene-C, SU-8 and polyimide. These polymer membranes have around 100 times lower thermal conductivities and are 10 times thicker than the Si-based materials [47].

The use of polymers as the substrate materials for the microcalorimeter also originated from the need of incorporating microfluidics as an automated fluid handling component. Industries and academia working on microfluidics have long seen the potential benefits in employing polymers, mainly due to its flexibility, low cost per unit area and simplified manufacturing processes. Compared to silicon and glass, polymer is cheaper. For instance, a PMMA sheet of 1.5 mm ×1.2 m×1.8 m costs about $17, while a silicon wafer with a 100 mm in diameter costs $14. The costs comparison is simplified by ignoring the cost of cutting and milling PMMA sheet into wafer shape [80]. Furthermore, the processing of certain polymers can be accomplished outside of the cleanroom, thus lowering the cost of fabrication.

Many polymer materials provide greater mechanical yield strain than silicon. Although silicon with a large Young's modulus is mechanically strong, this material is relatively brittle. Polymers can sustain greater degree of deformation and provide chemical, structural and biological functionalities, as shown in Table 2.1. Several types of polymers are explained next.

Parylene is a variety of chemical-vapour-deposited poly (p-xylylene) polymers. Parylene is an excellent material for the thermal insulation of the reaction chamber. Traditionally, parylene is used to form an insulating thermoplastic coating on electronic devices. Recently, this material has been used as a substrate for the membrane of a microcalorimeter [54]. Parylene-C is more

often the popular choice in microcalorimeter. It can be formed into very thin and conformal layers, and has a good chemical resistance and biocompatibility, which are favourable for fluid handling [81]. The low thermal conductivity of parylene decreases the heat loss. Furthermore, parylene has very low gas permeability and high mechanical strength allowing vacuum encapsulation [54].

PDMS is a polymer consisting of inorganic siloxane backbone with methyl groups attached to the silicon [76]. It is a potential material for the fluid handling component. It has been the popular material for microfluidics [58] [54, 71] due to its low cost, robustness, excellent proven biocompatibility [82], non-permeability to liquids, optical transparency and ability to withstand very big distortions without deteriorating features. PDMS can be micromachined using replica moulding. It is best to replicate structures on the surface of the mould as it can be cast at room temperature and thermally annealed. Despite these advantages, PDMS suffers from swelling in most organic solvents. The swelling makes handling organic solvents impossible in these PDMS devices.

PMMA is a thermoplastic polymer with high mechanical strength, high chemical resistance, high Young's modulus and low elongation at break. It is one of the hardest thermoplastics, exhibits low moisture absorbing capacity and has good resistance to extreme temperature changes. PMMA can be micromachined through x-ray exposure, hot embossing, laser machining and injection moulding. In a recent comparison of mechanical behaviour of PMMA and PDMS [83], the latter is better than the former in terms of maximum deformation. In a microcalorimeter, the PMMA is normally used as the structural material for the reaction chamber and the PDMS is normally used as the microfluidic channels.

The negative thick-film photoresist SU-8 was patented by IBM in 1989 [84]. This photoresist consists of EPON Resin SU-8 (from Shell Chemicals) as a main component. SU-8 has been used as the structural material in labs-on-chip devices [85] and also in microcalorimeters [56, 58]. It has good chemical compatibility and biocompatibility, and is suitable for coating conformal surfaces for protection. For instance, SU-8 was used to planarize the surfaces of the microcalorimeter with a parylene membrane [54]. The cost of SU-8 photolithography is considerably lower than other techniques such as LIGA process (for other photoresist) and the deep reactive ion etching (for silicon).

2.3.3.3 Design examples

In this section, we highlight several microcalorimeter designs with recent breakthroughs in device performances. The key to the improvements are good thermal insulation, efficient fluid handling mechanism and clever use of materials and fabrication processes. Different reaction

chamber designs (closed and open) and thermal detectors (thermopiles, thermistors and other temperature sensors) are also explored.

The researchers from Palo Alto Research Centre and the Scripps Research Institute [26, 27, 86, 87] developed an enthalpy array. It was a microcalorimeter in an array format that allows parallel measurement of the thermodynamics parameters such as enthalpy, entropy, Gibbs free energy and stoichiometry, which promises higher throughput for FBDD screening. This enthalpy array required small sample volume in the sub-microlitre and increases throughput by executing measurements in parallel. The use of micromachining technology enabled the miniaturisation of the temperature detectors, thus reducing the volume of sample significantly. Sample volume was reduced from 190 µl [88] using a commercial Isothermal Titration Calorimeter (ITC) to 500 nL [26] of a droplet in these microcalorimeters. The system consisted of an array of individual thermal detectors, built on a thermally insulating thin plastic membrane. Figure 2.8 shows an individual detector and Figure 2.9 shows the entire array.

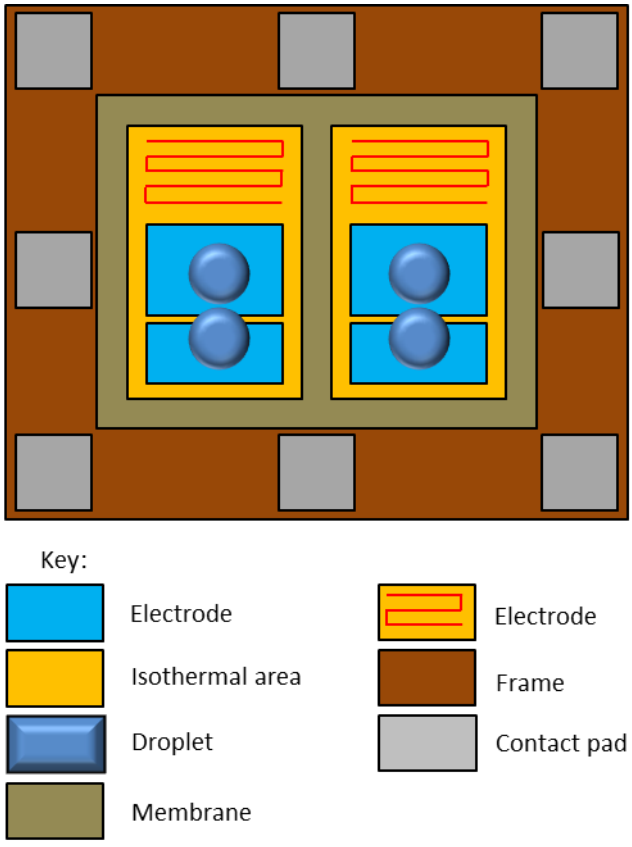

Figure 2.8: Schematic view of an individual detector [26]. It has two sensing regions: the reference and the measurement chamber. Two reacting droplets are placed on the left region, and the non-reacting droplets are placed on the right region.

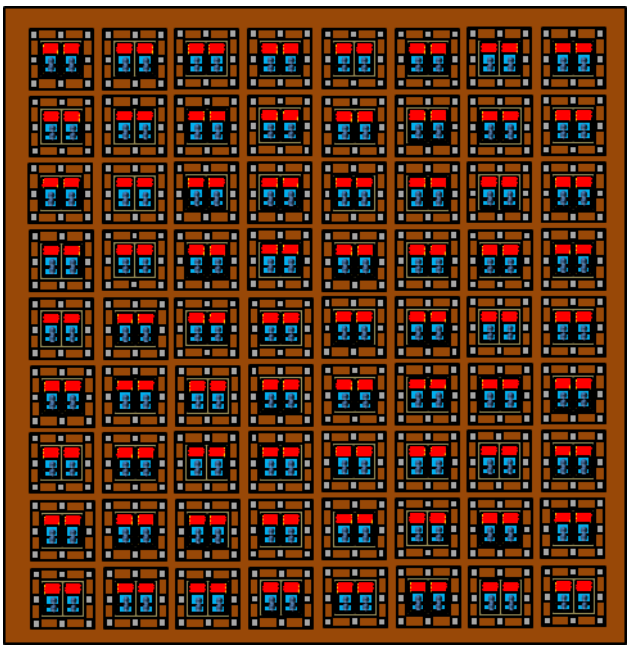

Figure 2.9: Enthalpy array with 72 individual detectors [87]

Each individual detector was fabricated on a thin film membrane suspended over a cavity in a rigid stainless-steel support plate. The type of membrane varied from polyimide [26] to polyethylene naphthalate (PEN) [27]. Two rectangular thermal equilibration regions consisted of 9 µm thick copper islands etched on the bottom of the membrane. This design employed differential method to measure the temperature. Therefore, the device had two similar sensing regions: the reference and the measurement chamber. The sensing regions were enclosed by electrical contact pads located on top of the support plate. Each region contained two thermistors.

The thermistors in both regions were connected to a Wheatstone bridge to reduce the common-mode noise. The thermistors were fabricated from an n+ amorphous silicon film [26] deposited by plasma enhanced chemical vapour deposition (PECVD) using silane and phosphine. As part of thermal insulation, a polymer cap layer enclosed the array in order to minimize drop evaporation, as shown in Figure 2.10. Device sensitivity had improved by almost an order of magnitude when the thermistor material was changed from amorphous silicon [26] to vanadium oxide [27], and finally to the use of the cantilever microprobes [89].

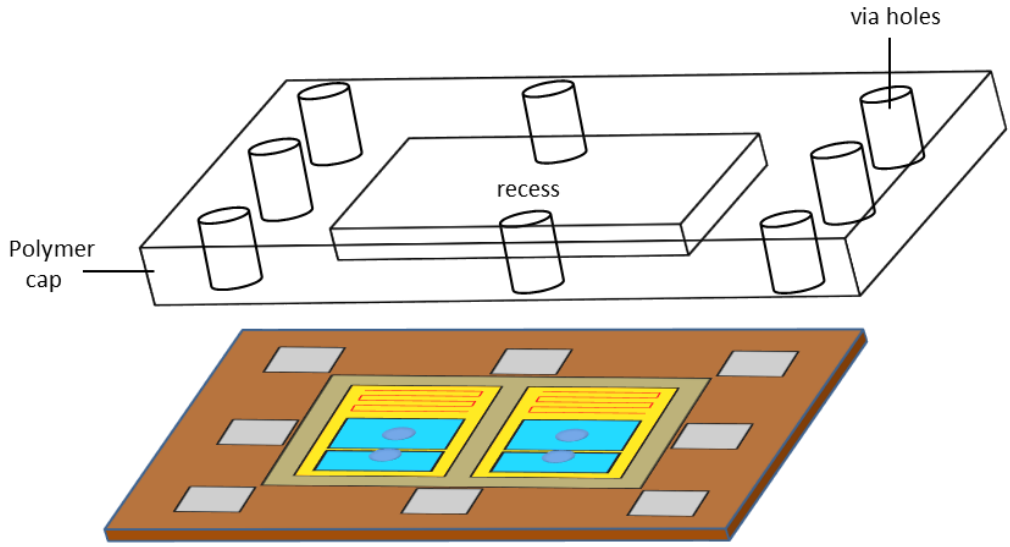

Figure 2.10: Schematic view of an individual detector with the polymer cap to minimize drop evaporation [27].

During measurement, two droplets of 250 nl samples were initially merged electrostatically on the sensing region. Two identical non-reacting droplets were merged on the reference sensing region at the same time to provide a reference for the differential measurement. Upon merging, the output voltage of the Wheatstone bridge was recorded. The signal was amplified by an analogue amplifier, and then sent to a digitization and lock-in detection stage. The entire process of array manipulation, drop deposition, detector encapsulation, contacting and data recording were performed using a fully automated measurement system. With this method, any temperature rise in the sample under test will be precisely recorded. All measurements were performed at a fix temperature. The thermal dissipation time of the system was 1.3 s. Each detector in the enthalpy array was able to detect a 500 µK of temperature change with a signal-to-noise ratio of 6 [26].

Zieren et. al [57] developed the first generation of silicon microcalorimeter with integrated thermopiles. The thermopile consisted of 4 x 118 BiSb/Sb thermocouples. The total thermopower (or Seebeck coefficient [90]) of the thermopile was 63.7 mV/K. The microcalorimeter was formed by a silicon chip and a PMMA chip, which were bonded with chemically inert epoxy glue. Two layers of silicon nitride of 1 µm thickness were deposited onto the silicon chip to form the free-standing membrane. Thin film of platinum and aluminium were deposited to form heaters for calibration and contact pads, respectively. The thermocouples were patterned in a way that the active junctions were located on the free-standing membrane. Reference junctions were in close contact with the silicon frame. Through this method, the membrane maximized the thermal resistance between the hot and cold junctions. The silicon also acted as a heat sink. Although this microcalorimeter achieved a rather high sensitivity, it's membrane showed chemical and mechanical instabilities.

Baier et al. [56] found the solution to improve the chemical and mechanical stabilities of the previous work by Zieren et al. Previously, silicon nitride membrane caused micro-cracks in the structure. They coated the silicon nitride membrane with thin layers of SU-8 epoxy photoresist. Coating SU-8 on the membrane stabilized the mechanical and chemical stability of the microcalorimeter. The SU-8 resist deposited on silicon was tested in different acids and bases ranging from a pH of 5-10 and showed no detectable corrosion over a period of more than 1000 hours.

Figure 2.11 shows the integration of dual thermopiles and a microchannel by Kwak et al. [71]. The dual thermopiles system effectively measured the heat generated by the biochemical reaction, and monitored the thermal equilibrium of the microcalorimeter in a self-compensation mode, without the need for adiabatic condition. This system was fabricated with chromium (Cr) and copper (Cu) using the MEMS technique (Process 1). The microchannel was fabricated using polymers (Process 2). The thermopiles were embedded into a silicon wafer using conventional wet chemical etching technique and photolithography. Four photomasks were prepared to make the Cr and Cu electrodes and also the SU-8 and PDMS microchannels.

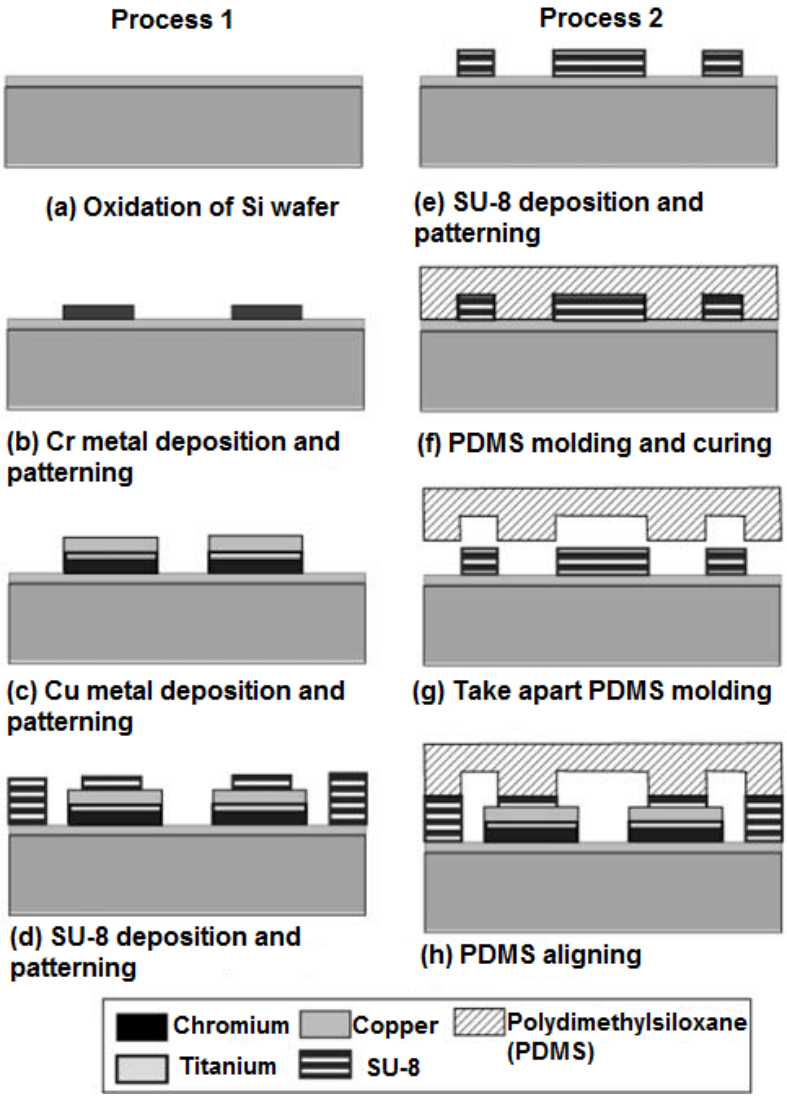

Figure 2.11: Fabrication of the dual thermopiles (Process 1) and microchannel (Process 2) [32]

Wang et al. [58] introduced a MEMS thermal biosensor in Figure 2.12, specially designed for detecting heat release from enzymatic reactions from glucose or other metabolite solutions. Enzymes were first immobilized on the microbeads packed in the reaction chambers before the glucose solution was flowed into the chamber. The calorimeter was integrated with polymer-based microfluidic channels. The reaction chambers were based on free-standing polymer diaphragms with low thermal conductivity and surrounded with air gaps incorporated in the microfluidic system. The design helped to increase the thermal isolation and reduced the thermal mass of the chambers.

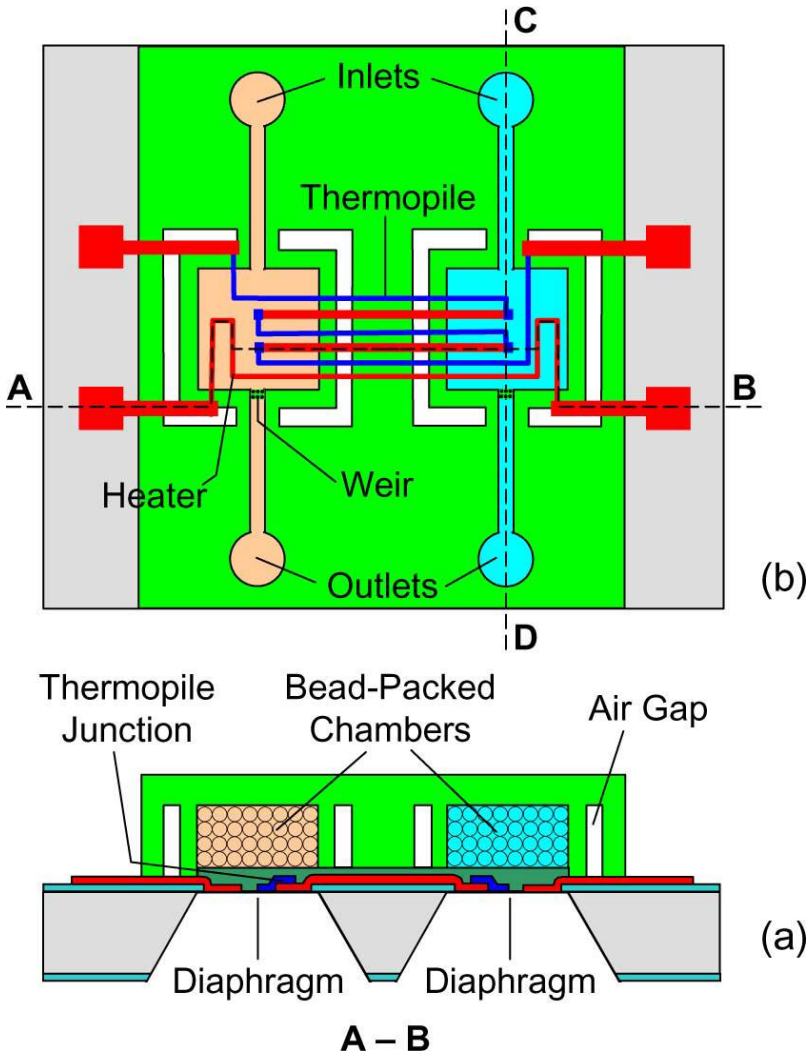

Figure 2.12: MEMS thermal biosensor: (a) top view as defined by the line A-B (b) Cross-section [58]

Xu et. al [52] presented a system for delivering sub-nL droplets of chemical reactants while avoiding evaporation via two layers of thermal shielding. The authors modified a commercial, suspended-membrane, thin film thermopile infrared sensor to integrate it into their microcalorimeter. A 50 nL droplet was initially placed directly on the sensor followed by a second droplet through a micropipette by means of a pressure driven droplet injector. The thermal shieldings were designed as follows. A Cu tube acted as an outer shield for a good electrical and convection shielding. A glass cover slide acted as an inner shield to protect the sensor from the external thermal noise. Sample evaporation was avoided by positioning the micropipette through a tiny hole in a cover glass, which was sealed with a drop of oil. Surface tension prevented the oil from leaking into the reaction chamber.

Lee et al. [54] developed a closed-chamber microcalorimeter as shown in Figure 2.13, with high sensitivity and accurate sample handling capabilities. Excellent thermal insulation was obtained by fabricating an on-chip vacuum encapsulation. This work also combined the use of PDMS and parylene-C. Parylene-C was used to build the measurement and vacuum chambers.

The flexible PDMS was used to form the microfluidic valves and pumps and was interfaced with the parylene-C channels and chambers to allow for an injection of samples of less than 1 nL. The chip was capable of characterising the heat reaction of the hydrolysis of urea, as well as the enthalpy of a mixture of water with methanol.

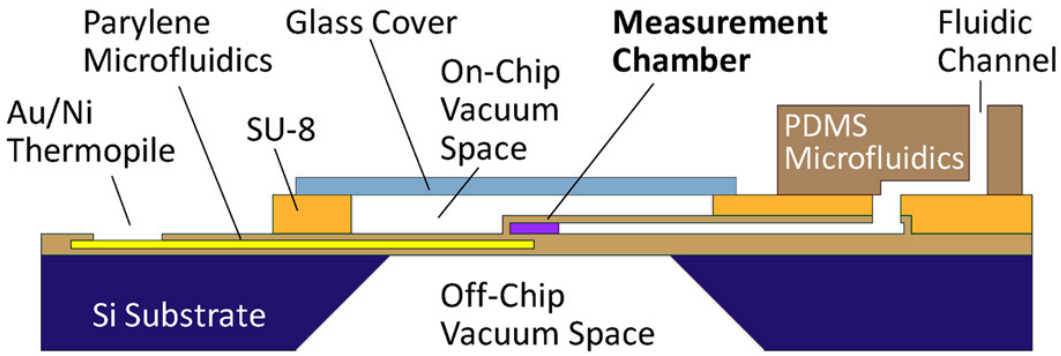

Figure 2.13: On-chip vacuum encapsulation calorimeter [11]

In a more recent work, Davaji et al. [59] constructed a microcalorimeter with a closed reaction chamber. The reaction chamber was 3D-micromachined using an anisotropic wet chemical etching process. This fabrication method eliminated the off-chip wafer bonding processes by direct integration of the thermal heater and temperature sensor onto the reaction chamber, as shown in Figure 2.14. The silicon nitride membrane was used to build the reaction chamber, and the chamber was suspended by the narrow tethers. This membrane reduced the thermal mass and increased the sensitivity of the system. Each microcalorimeter had two identical chambers for differential measurements. Samples were transferred via two microfluidic inlets. The heater and temperature sensor were on the opposite sides of the reaction chamber. This configuration allowed efficient coupling and detection of heat from the thermal elements. The prototype measured thermal diffusivity and specific heat of liquid samples. Other analysis can be carried out on the device without reconfiguration such as differential scanning calorimetry (DSC) [22-25], thermal wave analysis (TWA) [91, 92], 3-ω technique [93] and titration [51, 61].

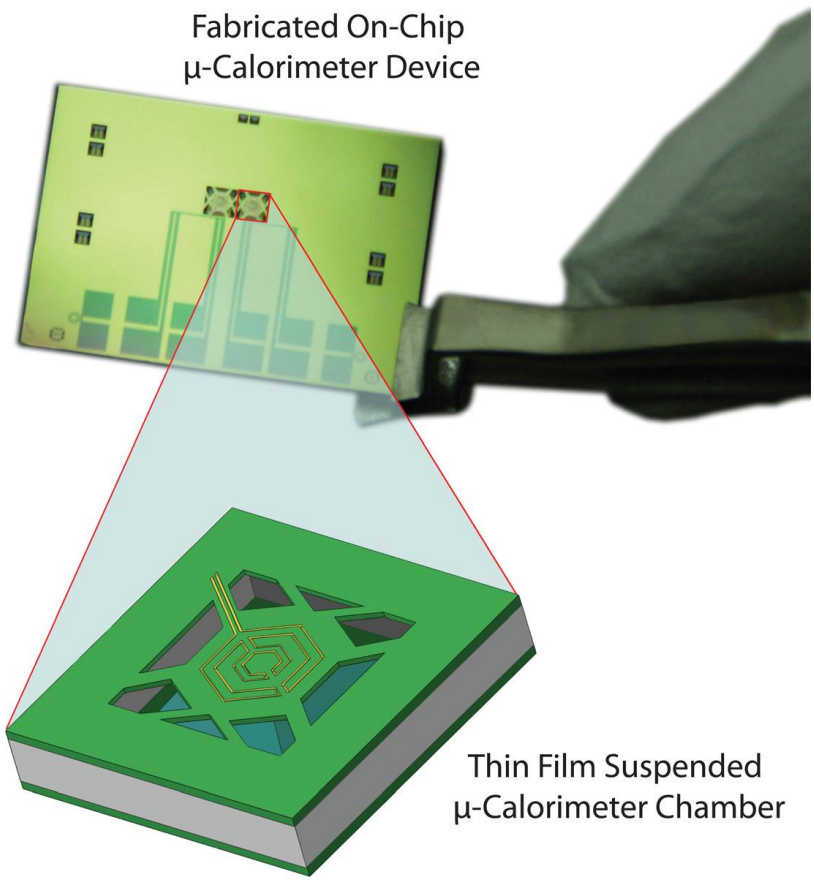

Figure 2.14: A 3D microcalorimeter with suspended reaction chamber [59]

Davaji et al. [16] also developed a metal patterning process to place the temperature sensors and heaters on the 3D structures of the SiN chamber. The process started with the symmetrical embossing of serpentine grooves on both sides of the wafer using a double-sided mask aligner. Then, the SiN and silicon dioxide (SiO_2) layers were etched by reaction ion etching (RIE) and buffered oxide etching (BOE) isotropic wet etching, respectively. The exposed silicon was then undercut using the poly etch. Subsequently, a SiN film was deposited to protect the exposed silicon via low pressure chemical vapour deposition (LPCVD).

Figure 2.15 shows the process flow for the 3D microfabrication of the microcalorimeter. Figure 2.15(a) shows the electrode patterns (heater and sensor) that were already printed symmetrically on both sides of the wafer as described in the previous process. Then the first anisotropic wet chemical (KOH) etching (figure 2.15(b)) was performed on the bottom surface of the wafer to create the reaction chambers. In Figure 2.15(c), a second KOH etching was then applied to define the suspended tethers of SiN on the top surface. Lastly, the sensor and heater components were integrated on the device by a blanket deposition of nickel on both sides of the wafer. After metallization, a polyimide film was use to seal the bottom of the wafer to form fully enclosed reaction chamber.

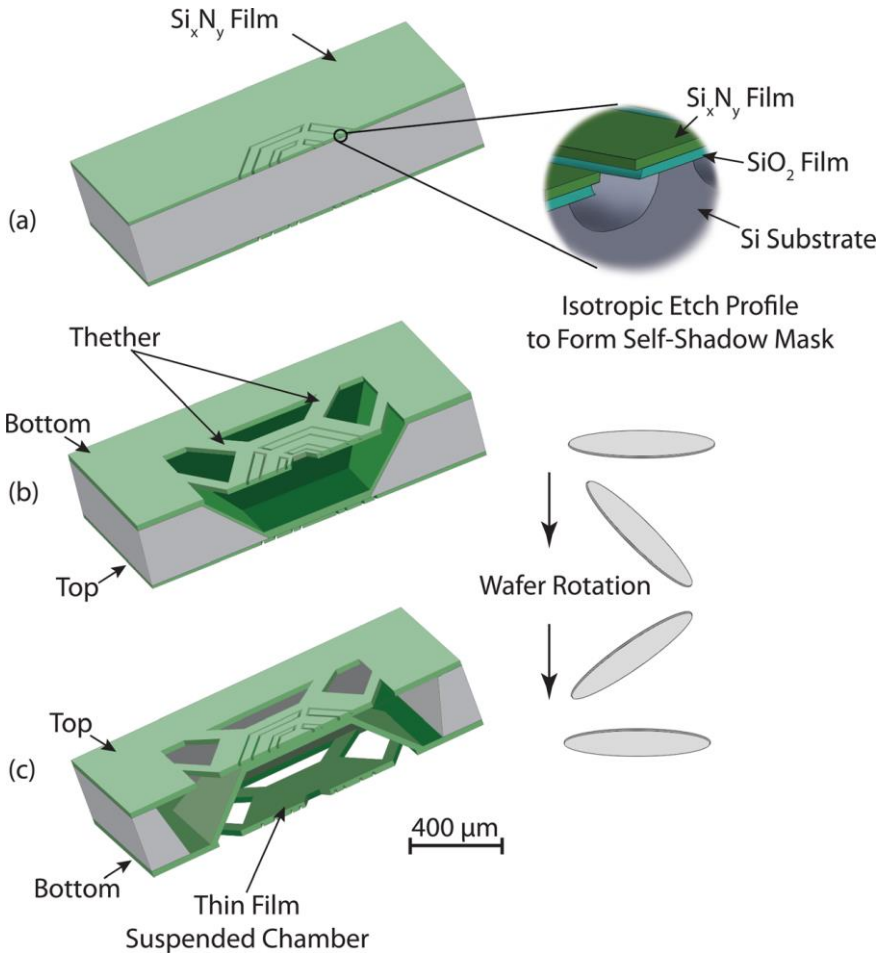

Figure 2.15: The process flow for 3D microfabrication of the calorimeter device [59]

Tables 2.3 and 2.4 summarize the previous works on the microcalorimeter. Table 2.3 compares the works in term of the type of chamber, fluid handling mechanisms, types of fluid-on-test, output resolution and power sensitivity. Table 2.4 compares these works in term of membrane material, temperature sensing, fluid handling material and the design novelty.

Table 2.3: Comparison of works in the literature on the types of chamber and fluid handling with their results. [54]

Source	Reaction chamber		Fluid handling	Fluid on test	Thermal conduct-ance, µW/K	Resolution		Power sensitivity (V/W)
	Type	Volume, nL				Power, nW	Practical energy, nJ	
Lee et. al [54]	closed	3.5	Multilevel microfluidics	Urea, Water with methanol	16	4.2	10	NA
Zhang et. al [55]	closed	15	Syringe pump	Glucose oxidase, catalase, urease on glucose, hydrogen peroxide and urea	5000	300	10^5	0.94
Baier et. al [56]	closed	6000	Syringe pump	Enzyme	10000	30	1000	4 -6
Wang et. al [58]	closed	800	Syringe pump	Glucose oxidase	1500	50	5000	0.87 – 1.2
Davaji et. al [59]	closed	200	Microfluidics	Water, glycerol, ionic liquids	NA	NA	NA	NA
Torres et. al [26]	open	500	Electrostatic merging	Protein ligand binding interaction	1000	50	750	NA
Recht et. al [27]	open	500	Electrostatic merging	Protein, Enzyme	1000	50	750	NA
Johan-nessen et. al[50]	open	0.75	Micropipette	Reagents, brown adipocytes ,cardiomyocytes, mitochondria	100	13	100	NA
Lerchner et. al[51]	open	6000	Micropipette	Enzyme catalysed reactions (urea and glucose)	30000	50	5000	NA

Xu et. al [52]	open	5-50	Micropipette	Protein	170	22	132	2.90(4)
Chancellor et. al [53]	open	0.05	Inkjet	Enthalpies in chemical or biological reaction	90	150	500	6.34
Kwak et. al [60]	Closed	70000	Microfluidic channel	Enzyme-substrate reaction	-	-	-	-

Table 2.4: Comparison of works in the literature on the types of material used in the production of the membrane, thermometry, microfluidics and the distinctiveness of the works.

Source	**Membrane Material**	**Thermometry**		**Microfluidics material**	**Novelties**
		Type	**Material**		
Lee et. al [54]	Parylene-C	Thermopile	Au/Ni	PDMS and parylene	Combination of parylene-C and PDMS microfluidics, on-chip vacuum encapsulation, thermopile has a meandering shape to increase its longitudinal thermal resistance. Five Au/Ni thermocouple junctions that are connected in series to produce a total Seebeck coefficient of 110 μV/K.
Zhang et. al [55]	Si_3N_4-SiO_2-Si_3N_4	Thermopile	gold (Cr/Au) on p-type polysilicon	Pyrex 7740 or PDMS	Pyrex wafer is anodically bonded on the polysilicon layer
Baier et. al [56]	SU-8 on Si	Thermopile	Thin film BiSb/Sb	PMMA	Based on SU-8 technology. Each system consists of 118 thermocouples.
Wang et. al [58]	SU-8 on Si	Thermopile	Cr/Ni	PDMS	Reaction chamber is filled with microbeads to immobilize the enzymes that react with the glucose fluids. The chambers are on a freestanding SU-8 polymer diaphragm base. Air gaps to increase thermal isolation.
Davaji et. al [59]	Silicon nitride	Integrated resistive temperature detector (RTD)	Nickel	NA	Fabrication of 3D reaction chamber with integrated heater and temperature sensor. Can perform several measurements including batch and scanning

					calorimetry.
Torres et. al [26]	Polyimide	Thermistor	Amorphous silicon	NA	An enthalpy array with the 96 microcalorimeter in parallel.
Recht et. al [27]	Polyethylene naphthalate (PEN)	Thermistor	Vanadium oxide (VO_x)	NA	Improvement of [5] by replacing the polymide membrane with PEN, and using VO_x thermopile.
Johan-nessen et. al [50]	SiN	Thermopile	Ni/Au	NA	Temperature sensing consists of 10 Ni/Au thermocouple junctions that are connected in series to produce a total Seeback coefficient of 220 µV/K.
Lerchner et. al [51]	Si	Thermopile	Silicon	NA	Pure silicon-based microcalorimeter.
Xu et. al [52]	SiO_2/Si_3N_4	Thermopile	Silicon (commercial)	NA	Double thermal shielding system.
Chancellor et. al [53]	SiN	Thermopile	Ti/Bi	NA	Temperature sensing consists of 7 Ti/Bi thermocouple junctions that are connected in a series to produce a total Seeback coefficient of 574 µV/K.
Kwak et. al [60]	Si	Thermopile	Cr/Cu	PDMS	Temperature sensing consists of 26 Cr/Cu thermocouple junctions that are connected in a series to produce Seeback coefficient of 519.2 µV/K.

2.4 Magnetically actuated liquid marble on solid surface and aqueous solution

2.4.1 The development of liquid marble

Liquid marble was first introduced by Aussillous and Quere [11] and Mahadevan [94] in 2001 as an alternative to achieve non-wetting property on solid surfaces. Liquid marble is obtained by rolling small amount of liquid, in range of 1 µL to 10 µL, in a chemically inert hydrophobic powder. Aussillous and Quere [11] used lycopodium grains of average size 20 mm covered with fluorinated silanes. Over the years, other types of hydrophobic powder have been used

such as silica powder [95, 96], oligomeric tetrafluoroethylene (OTFE) [97] or polytetrafluoroyethylene (PTFE) powder [98, 99], polyvinylidene fluoride (PVDF) nanobeads [12], polyethylene (PE) [100], hydrophobized copper [101] and iron oxide (Fe_3O_4) nanoparticles [102]. Interestingly, hydrophilic powder can also be used to coat the liquid such as graphite [16] and carbon black [103]. These particle coatings are separated by water clearings and they do not form a uniform shell as shown in Figure 2.16(b) and 2.16(c).

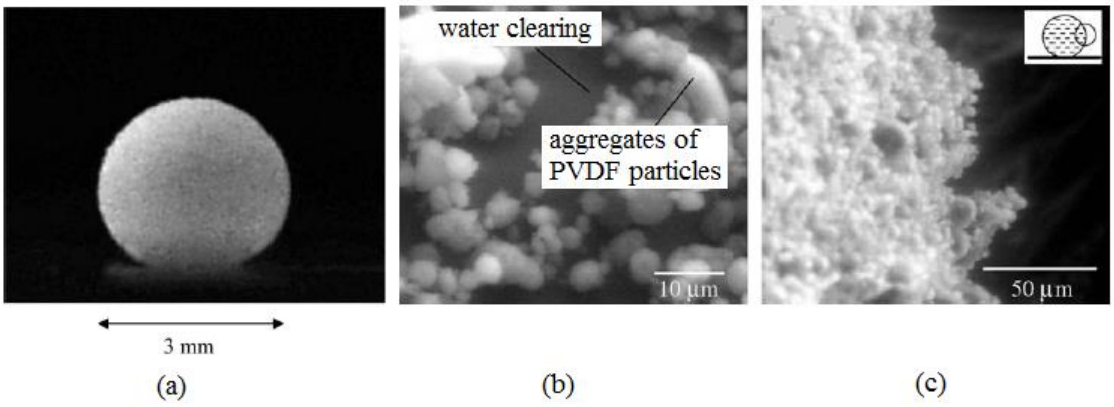

Figure 2.16: (a) Liquid marble coated with polyvinylidene fluoride (PVDF) at a volume of 10 μL. ESEM images of a liquid marble taken from the (b) surface of the marble, (c) upper view of the marble's boundary [12]

Liquid marble behaves like a soft solid and can be moved around. The encapsulated droplet forms a spherical shape when transferred on a solid surface or a container of fluid. Liquid marble reduces adhesion to solid surface. The non-wetting feature of liquid marbles allows the transportation of liquid without significant volume loss and energy loss due to the low friction with the platform surface. The useful properties of a liquid marble have been detailedly mentioned in several excellent review papers [95, 104-107]. A recent review by Ooi and Nguyen [108] demonstrated that a liquid marble can be actuated through electrostatic force [109], magnetic force [102], gravitational force [95], pressure gradient [110] and chemical schemes [111]. A review reported by Fujii et al [112] shows that liquid marbles can also be manipulated through stimuli responsive liquid marbles such as pH, temperature, light, ultrasonic and organic solvents.

In 2006, Aussillous and Quere [95] followed up their initial studies with investigation of the physics, properties and manipulation of the lycopodium-coated and silica coated liquid marble. They showed that the liquid marbles can be merged, separated, spread, burst and actuated by gravitational, electrostatic and magnetic fields. A year later, McHale et al. [96] studied about the electrowetting of silica coated liquid marbles. Within the same year, Gao and McCarthy [97] proposed the use of OTFE-coated liquid marble which is non-reactive and suitable to coat ionic liquids. They commented that the hydrophobized lycopodium and silica in the previous works

were only suitable for water and glycerol. The OTFE can coat a wide range of organic chemistry liquids. They also argued that OTFE-based water marbles were more robust and not easily evaporated.

From 2008, Bormashenko and co-workers have done many works on liquid marbles. Bormashenko et al. [13] investigated ferrofluidic liquid marbles and actuated these marbles with magnetic forces on superhydrophobic surfaces. They also reported comprehensive studies on the mechanisms of the floating and sliding of liquid marbles for manipulation purposes [12]. Then, these researchers studied the floating of liquid marbles in terms of critical density, shape, response to vibration, and surface tension [15, 100, 113]. At the same time, they were the first to report the new technique of preparation of liquid marbles with PVDF nanobeads [12]. It was also demonstrated that liquid marbles can be used for revealing water surface pollution with organic contaminants [114].

In 2010, Bormashenko et al. introduced the janus droplet [103]. Janus droplet consists of a hydrophobic hemisphere co-join with a hydrophilic hemisphere. In their case, they coated the liquid marble with two different powders; carbon black (hydrophilic material) and PTFE (hydrophobic material). By combining a semiconductor (carbon black) and a dielectric (PTFE), the janus droplet remained stable on solid and liquid substrates. The droplet could be activated with an electric field and showed potential for microfluidic applications, microsensors and actuators and stabilization of emulsions.

In the review paper by Bormashenko et al. in 2011 [106], works done on the static and dynamic properties and applications of liquid marbles over the years were discussed. They noted that the behaviour of liquid marbles under influence of the magnetic and electric field have yet to be thoroughly explored. Bormashenko and co-workers proceeded to study about the deformation of liquid marbles when a uniform electric field was applied and came up with a scaling law linking the radius of the contact area of the liquid marble to the applied electric field [115]. Works on liquid marbles have also progress towards magnetically controlled liquid marble with Zhao et al. extending previous magnetic actuation works [102, 116].

Liquid marbles containing living cells was first introduced by Arbatan et.al [20]. They presented how the liquid marbles containing cancer cell spheroids forming new spheroids. They further explained the features of liquid marbles that make it suitable for cells to live in. The porous shell allows the exchange of oxygen and carbon dioxide between the cell culture medium and the surrounding environment. Since it can be suspended in a medium, evaporation can be minimised by changing the humidity and temperature of the surrounding. In the confined

liquid marble, cells contacts with each other effectively that leads to enhanced aggregation. Besides, contamination of the encapsulated liquid can be avoided because the inner liquid is isolated from any substrates. Bormashenko et al. [12] provided experimental evidence that there was no direct contact between the liquid inside the liquid marble and the solid surface as well as the liquid the marbles floated on. They used chemically reactive liquids to verify the hypotheses.

Vadivelu et al. [19] had successfully used a floating liquid marble as a bioreactor platform to grow three-dimensional (3D) cell spheroids. The floating liquid marble allowed the cells to freely associate and interact to produce uniform sized spheroids. They compared their results with growing cells on a sessile liquid marble on a solid surface. The sessile liquid marble suffered from evaporation and also produced irregular sized spheroids. In their floating liquid marble model, the buoyancy enabled liquid flow within the marble. Thus, the effect of gravity that forces the cells to aggregate at the bottom of the liquid marble is minimized. They concluded that the quality of the spheroids depended on the internal mixing of the liquid marble. Moving the marble around will induce internal flow and mixing. Evaporation rate of liquid marbles [17, 117] have also been studied as this effect is inevitable and will be of great impact to cells as they can take from a few days to a week to grow the new spheroids.

Recently, Ooi et al. reported the kinematics and dynamics of a floating self-propelling liquid marble containing ethanol [24]. A floating object can move by itself if a gradient of surface tension is generated in the vicinity of the object. This phenomenon is known as the Marangoni solutocapillary effect. This self-driven movement was also reported by Bormanshenko et al. [14]. Self-propelling is difficult to control and depends on the availability of ethanol acting as the fuel inside the marble. Thus, a controlled manipulation of liquid marbles is still deemed as potentially useful for digital microfluidics.

2.4.2 Magnetic actuation of liquid marble on solid surface and aqueous solution

Magnetic actuation provides a non-contact and non-invasive control over magnetised liquid marbles. Permanent magnets can provide a large and long-range force on the magnetised liquid marble allowing the droplet to change its shape and motion. The magnetic field can penetrate through substrates and biological materials, enabling it to be potentially used in a variety of digital microfluidic application. Magnetite can be introduced to the liquid marble either by coating on the surface of the liquid or embedded into the liquid.

Aussillous and Quere [95] were the first to demonstrate magnetic liquid marbles. The idea of coating droplet with magnetic particles was obtained from Dorvee et al. [118]. They

investigated the influence of external magnet on a mixture of lycopodium with iron powder coating liquid marble and also iron powder inside a lycopodium coated liquid marble as shown in Figure 2.17. In both scenarios, the magnetised liquid marbles were attracted to the magnet. However, the liquid marble was released from the magnet after a short time because the iron particles were transferred to the magnet as shown in Figure 2.17(a). In Figure 2.17(b), the non-magnetic marble was subsequently released, leaving behind the iron particles on the magnet.

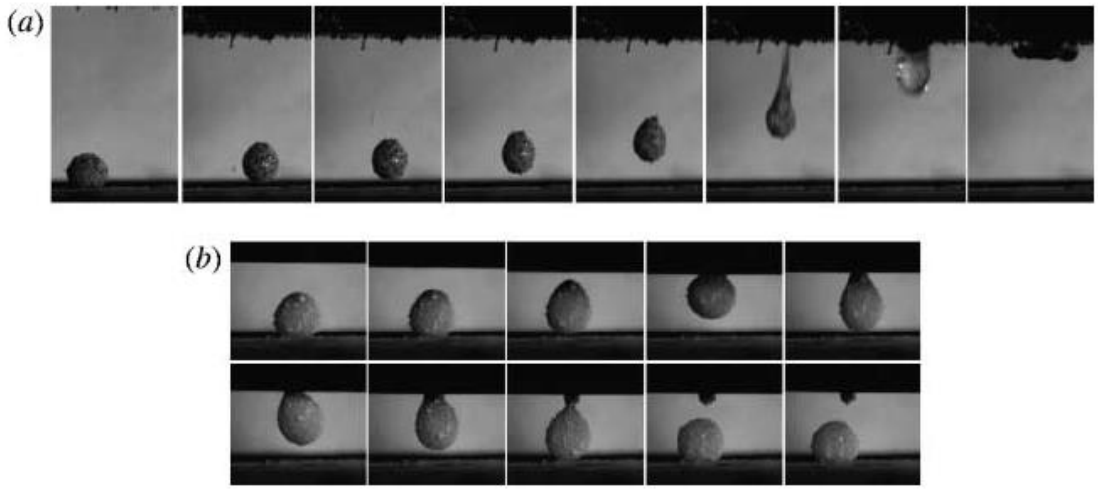

Figure 2.17: Influence of the magnet on (a) liquid marble coated with a mixture of lycopodium and iron powder, (b) liquid marble containing iron particles coated with lycopodium [95]

The threshold magnetic field strength needed to induce droplet movement has been experimentally investigated by Zhao et al. [116] using a magnetite coating and Bormashenko et al. [13] using a ferrofluid droplet. Both reported that the threshold magnetic force was equal to the frictional force between the marble and its carrier surface. Bormashenko et al. prepared ferrofluidic marbles using an aqueous dispersion containing γ-modification of Fe_2O_3 nanoparticles and polyvinylidene fluoride (PVDF) particles as the stabilizer. In their investigation, a 20 μL liquid marble could be moved on a flat polymer surface at a velocity as high as 25 cms^{-1} under the magnetic field strength of 0.5 T. This group used the liquid marbles as an actuator for a bearing device consisting of one ferrofluidic marble and two pure water marbles sandwiched between polyethylene (PE) and polypropylene (PP) films as shown in Figure 2.18(a). Activation of an external magnetic field allowed the controlled rotation of the upper PP film arising from movement of the ferrofluidic marble as shown by the arrows in Figure 2.18(b).

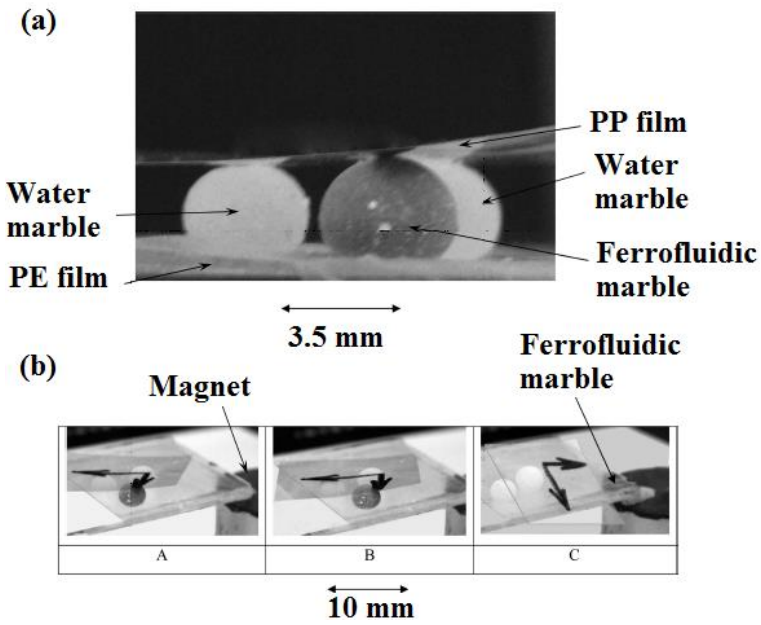

Figure 2.18: (a) Microfluidic bearing device, (b) rotation of the upper PP film.[13]

Zhao et al. [102] demonstrated that liquid can be extracted or added to a liquid marble coated with hydrophobic magnetic particles enabling the liquid marble to be used in micro reactor and micro mixer. Liquid marbles coated with magnetic powder can have their shells opened and closed reversibly [102, 116, 119] or even moved around [116, 118, 120] using a permanent magnet. Zhao et al. [121] coated a dopamine droplet with Fe_3O_4 nanoparticles. Figure 2.19 shows the electrochemical detection process. The marble rested on a glass surface. The magnetic liquid marble was actuated by a magnet which was initially located quite a distance that was sufficient to facilitate the movement. During the electrochemical detection, the magnet was moved nearer to the droplet to "open" the top surface of the marble by attracting the top nanoparticles towards the magnet at the bottom. An electrode was probed into the top part of the droplet to facilitate the measurement. After detection, the magnet was moved back to its original position and the nanoparticles coated the entire marble again. Subsequently, the marble was moved away from the detection area. For optical absorbance detection [116], a stronger magnet was used to fully open the marble. However, actuation with a small number of larger magnetic particles in a droplet would not work because the small magnetic force cannot overcome the friction force or would be too large so that the particle was removed from the droplet. The solution for reducing the friction was to float the liquid marble on a liquid surface and then dragged it with a minute number of magnetic particles and an external magnet.

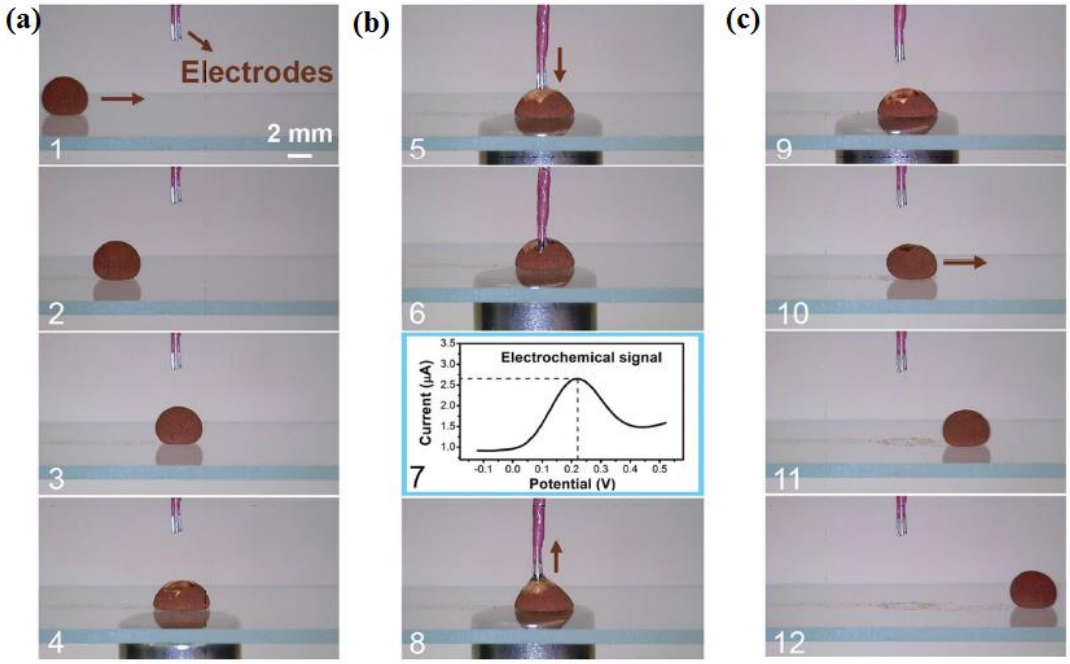

Figure 2.19: Electrochemical detection. (a) Movement (Steps 1–3) of a magnetic liquid marble on glass substrate, opening (Step 4) with a magnet (10 mm diameter × 12 mm length) (b) Three-electrode probe immersed into the droplet (Steps 5–6), recording of signal (Step 7), moving probe out of the droplet (Step 8). (c) Closing (Steps 9–10), moving away (Steps 11–12) liquid marble after detection. [121]

The applied magnetic field can change the shape and wettability of a liquid marble. This effect was known as magnetowetting. The liquid marble deforms under the influence of a permanent magnet. The deformation of a sessile ferrofluid liquid marble on a PTFE-coated glass substrate was studied in detailed by Nguyen [122]. Ferrofluid marbles was fabricated using a water-based ferrofluid and PTFE particles. In the sessile ferrofluid case, the radius of the contact region between the liquid marble and the glass substrate scaled with the fourth root of the magnetic Bond number. The vertical length of the marble scaled with the inverse square root of this number. This behaviour can be compared to a puddle-shaped marble deformed under gravity in the absence of the magnet versus its respective Bond number. Subsequently, the relationship between the magnetic field, movement speed and the marble shape was derived. Scaling analyses were conducted on the deformation of sessile and moving ferrofluid marbles in the presence of a permanent magnet. The scaling analysis of the moving ferrofluid showed that the dimensionless change in curvature was proportional to the capillary number. These experimental results indicated that the dimensionless contact diameter and height did not depend substantially on the speed or the capillary number. Similar to the sessile case, these geometric parameters were governed primarily by the magnetic Bond number.

Recently, Han et al. [123] demonstrated a spinning magnetically coated liquid marble. An applied rotating magnetic field measuring from 0 to 1300 rpm was used to spin the liquid

marble on a liquid surface. They claimed that their design is the world's smallest centrifuge and also a localized microviscometer.

2.5 Conclusion

Magnetic actuation is a popular manipulation scheme of liquid marbles due to its simplicity. Commercially-made small permanent magnets are conveniently available and can be incorporated into lab-on-a-chip devices. There is also a wide variety of available magnetic liquids off the shelf, and it is easy to control the amount of magnetic particles loaded into droplets and liquid marbles. These systems do not require external power supply. The speed of the droplets can be arbitrarily controlled by the speed of the external magnet. The benefits have encouraged the recent implementation of liquid marbles in digital microfluidics.

Chapter 3: Design and experimental methods

3.1 Introduction

In this chapter, the design and experimental works of the magnetic actuation of droplets are described. There are 3 types of magnetic actuation performed. First, the magnetic actuation of uncoated chemically reactive droplets on a superhydrophobic solid surface is presented. This is followed by the actuation of a floating liquid marble on water. Lastly, the magnetic actuation of the floating liquid marble on aqueous solution (medium) of different viscosity is investigated. The preparation of the droplets, experimental setups and data collections are explained.

3.2 Magnetic actuation and merging of acid-base for calorimetric measurement

Magnetically-controlled actuation of microdroplets that allows faster mixing is needed for the detection of the heat release from an exothermic reaction. In this experiment, a microdroplet containing HCl solution mixed with iron oxide was magnetically-actuated by an external permanent magnet to merge with a stationary droplet containing a NaOH solution. The coalescence of both droplets produced an exothermic reaction, which released a detectable heat of neutralisation. We studied the effects of volume of the droplets, the speed and the concentration of iron oxide to the mixing time and the amount of the heat being released. The experimental results indicated that a lower volume of droplet and a higher speed of magnet led to a shorter mixing time. We also calculated the enthalpy values based on the measured peak temperature of the heat. Finally, we found the suitable operating conditions of this system for micro calorimetric measurement of exothermic HCl-NaOH droplets.

3.2.1 Experimental setup

The experimental setup consisted of two PMMA plates, a PMMA holder, a thermocouple, a permanent magnet and a programmable x-y stage, as shown in Figure 3.1. The PMMA holder was 4.5 mm thick and had 2 slits to hold two 1.5-mm thick PMMA plates. The upper plate had a laser-cut hole (0.5 mm in diameter) to position a thermocouple through it. The thermocouple was a Class 1 Type K alloy (NiCr/NiAl). The welded end of the thermocouple had the shape of a 0.2-mm sphere. The thermocouple was suitable to measure down to a 1-µL droplet. The thermocouple was attached to a data logger (Picolog USB TC-08, Pico Technology Limited, UK). Microdroplets were placed on the lower PMMA plate. The lower plate was covered with 1200-grit sandpaper. Teflon powder (Sigma Aldrich, 1µm particle size) were coated on the sandpaper to create a hydrophobic surface for easy manipulation of the microdroplet. The

thermocouple was aligned such that its sensor touched the stationary microdroplet on the lower plate.

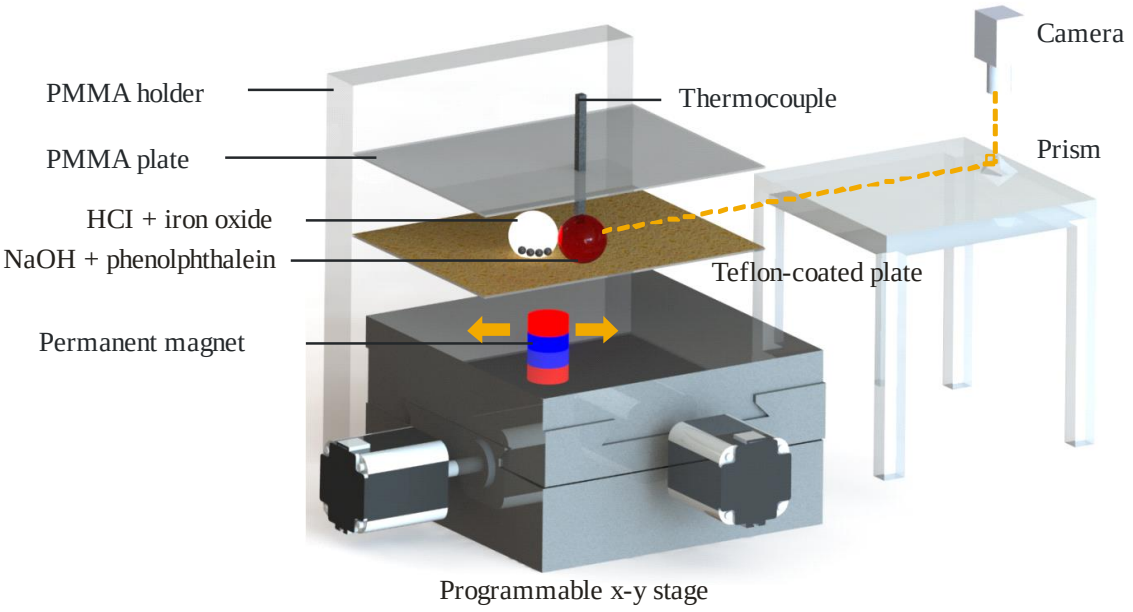

Figure 3.1: Experimental setup

A cylindrical permanent magnet (Neodymium, a diameter of 10 mm and a height of 5 mm) was fixed on a programmable x-y stage. The permanent magnet was placed below the lower plate as a tool to move the microdroplet. This magnet was positioned 2 mm away from the hydrophobic surface. We used the vernier caliper to accurately adjust the distance, taking into account the plate thickness of 1.5 mm. The magnetic flux density of the magnet was measured with a handheld gaussmeter (GM07, measurement range from 0 to 3T, Hirst Magnetic Instruments Ltd, UK). The measured flux density on the surface is 235 mT. The x-y stage (Zaber Technologies T-LS28M) was a motorized linear actuator with built-in controllers. The actuator has a travel range of 28 mm, a maximum speed of 6.5 mm/s and a minimum speed of 0.930 µm/s. The linear motion of the actuator was controlled by the Zaber Console software to provide a smooth and automated motion in both directions. Codes were programmed to define the velocity and actuation. The actuator was linked to the PC through the RS-232 port.

The experimental work included video recording and temperature recording. The images of the microdroplets were captured by a Nikon camera with an adjustable lens (AF Micro Nikkor 60 mm f/2.8D). The camera was connected to the PC through a USB camera (Edmund optics Inc, Singapore). The camera software (uEye cockpit, IDS, Germany) was set to record up to 40 frames per second in a single movie file. During image processing, the frames were separated and evaluated individually using ImageJ (NIH, USA) processing tool and a custom-written program in Matlab, to obtain the mixing times.

The side view of the microdroplets was recorded to properly examine the mixing performance. A 45^0 prism was placed below the camera to enable the capture of the side view of the microdroplets. Video recording was set at 39.2 frames per second and 82 MHz pixel clock. The experiments were carried out to determine the mixing time and the mixing index. For temperature recording, the data logger converts the electrical signal from the thermocouple to give the real-time temperature readings over time. Temperature data were sampled every 1 ms. Both image and temperature data requisition ran simultaneously.

The microdroplets were dispensed using a micropipette (Genex-Beta, UK). The micropipette can dispense volumes ranging from 0.5 to 10μL. The microdroplets on the Teflon-coated surface assumed a spherical shape. We prepared a 1.0 M solution of hydrochloric acid (AjaxFineChem, HCl 32%, MW=36.46) and a 1.0 M solution of sodium hydroxide (Chem Supply, NaOH pellet, MW=40 g/mol). This acid-base combination was chosen because they are common reagents that can produce a detectable exothermic reaction and have a known enthalpy value of -57.7 kJ/mol at room temperature [124]. The complete neutralisation of the HCl and NaOH can be observed using pH indicators such as the phenolphthalein (Scharlau, solution 1% in ethanol). The indicator helped to determine whether the mixing has been thoroughly completed. For the non-reactive droplet experiment, we used deionized water, with one droplet added with yellow food dye (Queen brand).

The microdroplet that was actuated by the permanent magnet contained iron oxide particles (Sigma-Aldrich, Iron II/III oxide, Fe_3O_4, MW = 231.53 g/mol). Since the iron oxide particles were mixed with HCl, there was a possibility for reaction (3.1) to occur.

$$Fe_3O_4 + 8HCl \longrightarrow FeCl_2 + 2FeCl_3 + 4\,H_2O \quad (3.1)$$

However, these iron oxide particles have an average diameter size of less than 5 μm and iron content of about 68.0 - 76.7 wt%. Due to the relatively large particle size and the fact that Fe_3O_4 dissolves slowly in HCl [125-127], the iron oxide particles were not reacting with diluted HCl in our experiment. We performed a reaction test (in terms of temperature) on the iron oxide particles and 1M of HCl. Figure 3.2 shows that there was no significant temperature change for HCl only and HCl with iron oxide particles for two separate tests over 40 minutes. Since the duration of our experiments only lasted up to 5 minutes, it was unlikely that the reaction (3.1) took place within the short period of time. Moreover, the Fe_3O_4 is generally inert and notably used as a magnetic carrier for catalyst or enzymes [128].

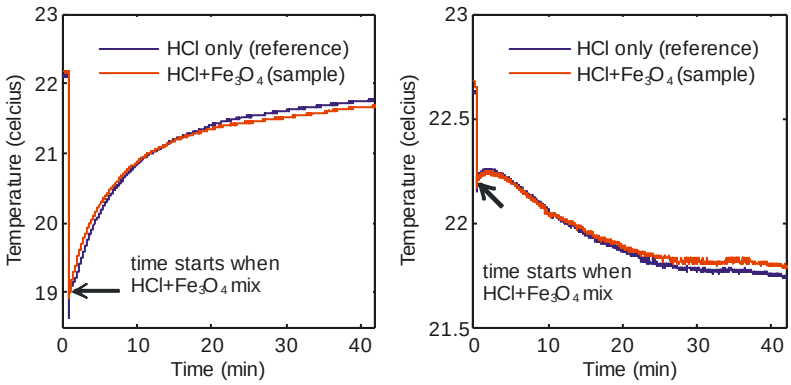

Figure 3.2: Temperature change between reference (HCl only) and sample (HCl + Fe_3O_4) for two separate tests (left and right figures). The concentration of iron oxide is 0.040 g/ml.

The concentration of iron oxide was varied in the experiment as 0.010 g/ml, 0.020 g/ml and 0.040 g/ml. The iron oxide was accurately weighed using a high precision analytical balance (Radwag, USA) with readability down to 0.1 mg. For instance, a volume of 2 ml of fluid was mixed with 20 mg of iron oxide to make the 0.010 g/ml concentration. An external magnet was used to move the microdroplet to merge and mix with another stationary microdroplet. The external magnet moved back and forth to create a shaking process and to facilitate mixing inside the merged droplet. The mixing time and the temperature response were recorded and evaluated as function of parameters such as the volume of the microdroplets, the concentration of iron oxide and the speed of the magnet.

The sandpaper coated with Teflon powder on the lower PMMA plate (Figure 3.1) served as the planar surface for the actuation of the microdroplets. We scratched off the Teflon powder in the middle of the surface to leave a small hydrophilic patch for the stationary droplet. The stationary microdroplet contained the aqueous NaOH solution mixed with phenolphthalein making the initial droplet to appear pink. The thermocouple first measured the pre-reaction temperature of the stationary droplet. The moving droplet contained HCl solution mixed with iron oxide. The magnet moved the HCl droplet towards the NaOH droplet. The droplets subsequently merged and were shaken by the periodic motion induced by the permanent magnet. Complete mixing occurred when the pink colour vanished from the merged droplet. The mixing time was determined as the period between the first contact of the droplets and complete mixing. The mixing time was evaluated from the recorded images. Concurrently, the temperature response was recorded from the pre-reaction stage to the equilibrium of the neutralization process. Figure 3.3 shows the typical frames of the merging/mixing process of the HCl and NaOH droplets with a speed of 2.79 mm/s and an iron oxide concentration of 0.010 g/ml. The discolouration of the phenolphthalein shows the end of the chemical reaction and mixing at 2.95s.

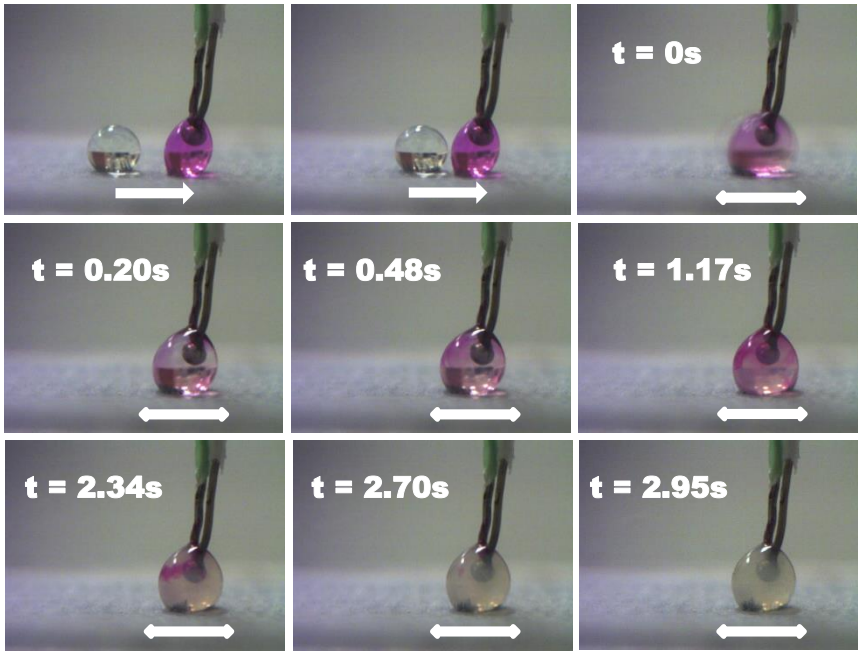

Figure 3.3: Image sequence of the merging/mixing process of the HCl droplet with the NaOH with phenolphthalein as indicator. Mixing time starts when the droplets merge. The discolouration indicates the completion of the mixing process and also the end of the reaction. Temperature was recorded via the thermocouple. The white arrow indicates the back and forth movements by magnetic actuation.

3.2.2 Mixing evaluation

Mixing can be clearly visualised using fluorescent dyes, food colour dyes or pH indicators. In our experiment, we used food colour dye (yellow) for the non-reactive droplets and phenolphthalein for the reactive droplets. We evaluated the mixing time using ImageJ, an image analysis software, followed by statistical analysis quantifying the mixing index. We then converted the 8-bit image of the droplet into a three layered RGB stack. The pixel intensity c_K is 0 for white and 255 for black. ImageJ will extract data at a particular area of the droplet. The sampling area was placed away from the iron oxide concentration. The mixing efficiency is determined as:

$$\eta = \left[1 - \sqrt{\frac{1}{N}\sum\left(\frac{c_k - \bar{c}}{\bar{c}}\right)^2}\right] \qquad (3.2)$$

where N is number of pixels in the sampling area, c_K is the intensity value of a particular pixel k and $\bar{c}$ is the average indexes in the sampling area. When the mixture is uniform, the mixing efficiency approaches 100%. Figure 3.4 shows the mixing efficiency for two 1-µL droplets with an iron oxide concentration of 0.010 g/ml at a speed of 2.79 mm/s. Once it reaches 100%, the mixing is homogenous and the time of mixing is recorded.

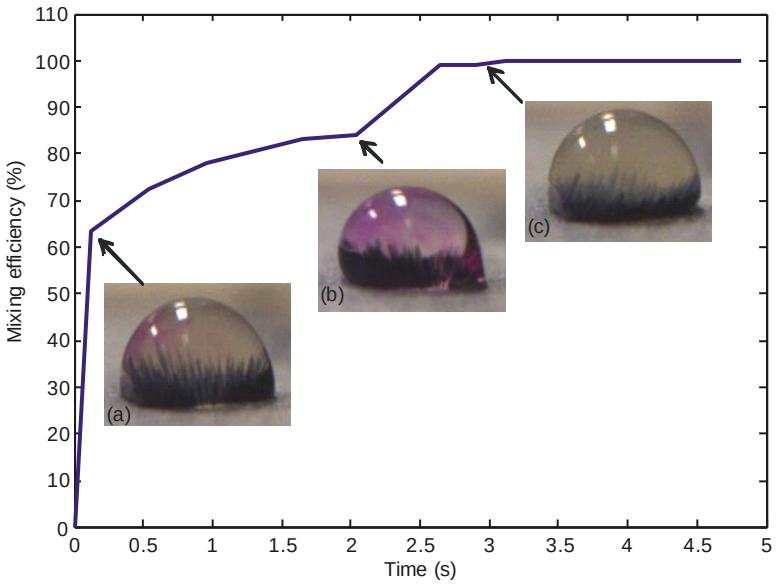

Figure 3.4: Mixing efficiency for the mixing of two 1-µL droplets with an iron oxide concentration of 0.010 g/ml at a speed of 2.79 mm/s. Inset: Image sequence for mixing at (a) 0.12s, (b) 2.04s, (c) 2.91s i.e. complete mixing.

3.3 Magnetic actuation for floating liquid marble on water

Controlled actuation of a floating liquid marble, a liquid droplet coated with hydrophobic particles floating on another liquid surface, is a potential digital microfluidics platform for the transportation of aqueous solution with minimal volume loss. In this experiment, we investigated the magnetic actuation of floating liquid marbles filled with magnetic particles. The magnetic force and the frictional force acting on the floating liquid marble determined the horizontal movement of the marble. We varied the magnetic flux density, flux density gradient, concentration of magnetic particles and the speed of the marble to elucidate the relationship between the acting forces. We subsequently determined the suitable operating conditions for the actuation and derived the scaling laws for the actuation parameters.

3.3.1 Experimental setup

Figure 3.5 depicts our experimental platform, which consisted of a holder made of poly methyl methacrylate (PMMA,) a container made of polystyrene, a permanent magnet and a programmable x-y stage. The holder was made of 4.5-mm thick PMMA plates and had a slit to hold a 1.5-mm thick PMMA plate for positioning the 10 cm×10 cm polystyrene container. The water levels to be filled were marked with a permanent marker on the polystyrene container. A cubic permanent magnet (Neodymium, 3.12 mm × 3.12 mm × 3.12 mm) was fixed on a programmable x-y stage. The permanent magnet was placed below the container as a tool to move the floating marble. This magnet was positioned at distances of 6 mm, 8 mm, 10 mm, 12 mm, 14 mm and 16 mm from the water level markings. We used a vernier caliper to

accurately adjust the distance, taking into account the combined thickness of 2.5 mm of the PMMA plate and the polystyrene container.

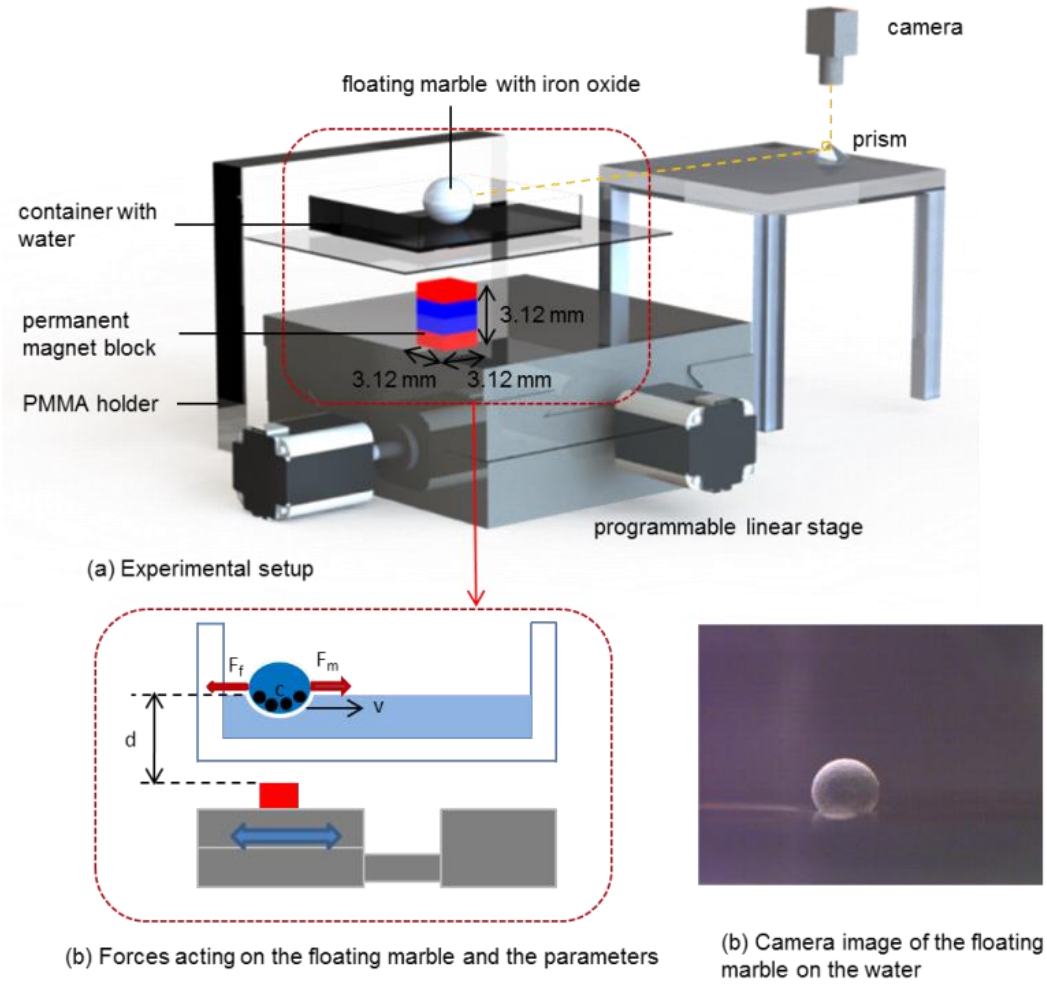

Figure 3.5: (a) The experimental setup; (b) Horizontal forces acting on the floating marble (magnetic force F_m and friction force F_f). The parameters of the experiments are the distance between the floating marble from the magnet *d*, the concentration of the iron oxide particles *c*, and the velocity of the permanent magnet *v;* (c) A typical image of the floating marble on the water surface captured with the setup.

The x-y stage was a motorized linear actuator (Zaber Technologies T-LS28M) with built-in controllers. The actuator has a travel range of 28 mm, a maximum speed of 6.5 mm/s and a minimum speed of 0.93 μm/s. The linear motion of the actuator was controlled by the Zaber Console software. Codes were programmed to define the velocity of the actuator. The actuator was linked to a personal computer (PC) through a RS-232 port. The actuator allowed a programmable and smooth motion of the permanent magnet in both directions.

The experimental setup facilitated video capturing of the moving liquid marble. The video of the floating marble was recorded and further processed to examine the motion. For this purpose, a 45˚ prism mirror was placed under the camera to capture the side view of the floating marble

without blocking the x-y stage and the container. The floating marble was backlit with a light source to create a large contrast between the marble and its surrounding. The images were captured by an USB camera (Edmund Optics Inc, Singapore) with an adjustable lens (AF Micro Nikkor 60 mm f/2.8D). The camera software (uEye cockpit, IDS, Germany) was set to record the motion with 30 frames per second (fps) in a single movie file. In the subsequent image-processing step, the frames were separated and evaluated individually using ImageJ (National Institutes of Health, USA) and a custom-written program in Matlab (Mathworks, USA), to obtain a quantitative assessment of the motion (displacement, velocity and acceleration) of the floating marble as shown in Figure 3.6.

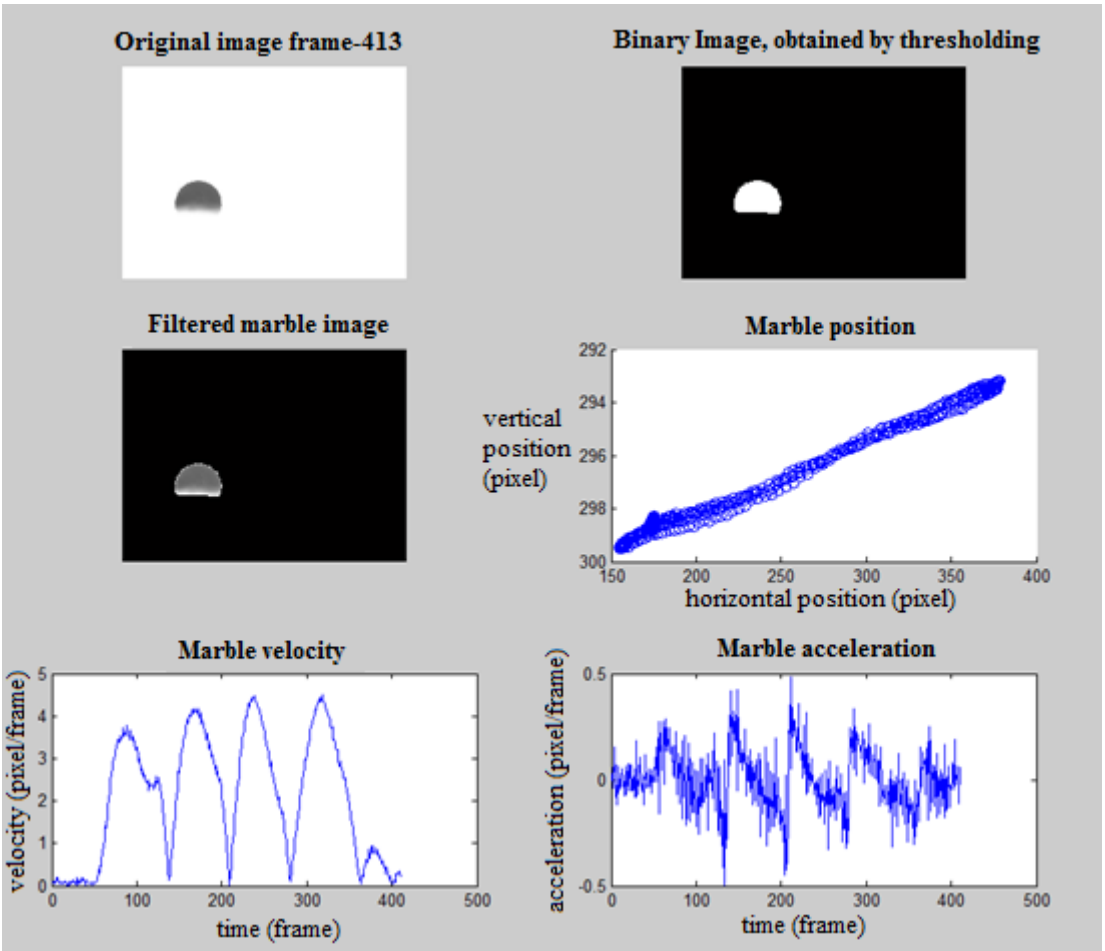

Figure 3.6: Quantitative assessment of the motion (displacement, velocity and acceleration) of the liquid marble. Datas on axes are in pixels which will then be converted to the suitable metric units.

In the experiments, deionised water was filled into the container till it reached the first marked level, representing 6 mm distance from the magnet. A 5µL magnetised liquid marble was carefully placed into the container. The floating marble automatically aligned itself to the centre of the permanent magnet. The magnet was programmed to move back and forth with a pre-set amplitude of 4.96 mm and 9 speeds ranging from 0.465 mm/s to 4.19 mm/s. Next,

0.2 ml of deionised water was drawn with a syringe and added into the container corresponding to an increase of 2 mm in the water level. The experiment was repeated for the different water levels. The motions of the floating marble are recorded and analysed for each water level or marble-magnet distance and its corresponding speed. The Matlab program then processed the video and measured and tracked the centroid of the floating marble as it moved back and forth with the permanent magnet.

3.3.2 Preparation of floating liquid marble

The liquid marble was formed by mixing deionised water with iron oxide powder (Sigma-Aldrich, Iron II/III oxide). Magnetite particles are spherical with a diameter of less than 5 μm and a density of approximately 4.8 to 5.1 g/mL at room temperature. The iron oxide was accurately weighed using a high precision analytical balance (Radwag, USA) with a resolution of 0.1 mg. For instance, a volume of 4 mL deionized water was mixed with 12 mg of iron oxide to generate a concentration of 0.003 g/mL of magnetic particles. A 5 μL droplet of the magnetic solution was dispensed into a bowl filled with polytetrafluoroethylene (Teflon) powder and rolled into a liquid marble. The Teflon powder (Sigma Aldrich) has a particle size of 1 μm and a density of approximately 2.2 g/mL. A micropipette (Genex-Beta, UK) was used to accurately dispense 5 μL of the liquid. The liquid marble was continuously rolled until completely coated. The liquid marble was then picked up with a stainless steel spoon and further rolled around to remove the excess powder. The uniformly coated liquid marble was then carefully transferred to a polystyrene container which was initially filled with deionised water as its carrier liquid (medium). The liquid marble floated on the surface and can be actuated by a moving an external permanent magnet.

To check the repeatability of the number of magnetic particles in a liquid marble, we dispensed a 5-μL droplet of the prepared solution on a glass slide and let the water evaporate. The remaining solid particles formed black spots on the slide. Then, we took a high-resolution image (2560 pixel × 1920 pixel) of the particle spots and analysed it with ImageJ by counting the pixel ratio of the magnetic particles over the area of the droplet. At the same time, we dispensed a 5 mL droplet of the prepared solution and weighed the magnetic particles after the water evaporated. The reason for dispensing a larger droplet for weighing was to increase the precision of weighing the light magnetic particles. Figure 3.7 shows the consistency of the number and weight of magnetic particles in a droplet for three different concentrations; 0.001 g/ml, 0.003 g/ml and 0.005 g/ml. The data were collected with 10 samples of each concentration. The lower concentration showed a smaller error bar for the pixel ratio because the particles have enough space to disperse. At higher concentrations, particles could have formed a three-dimensional cluster leading to a nonlinear relationship between the pixel ratio

and the concentration and a larger error bar as shown in Figure 3.7. The weight of the magnetic particles showed a linear relationship towards the concentration. The percentage of loss was about 18%-20% for each dispensed droplet.

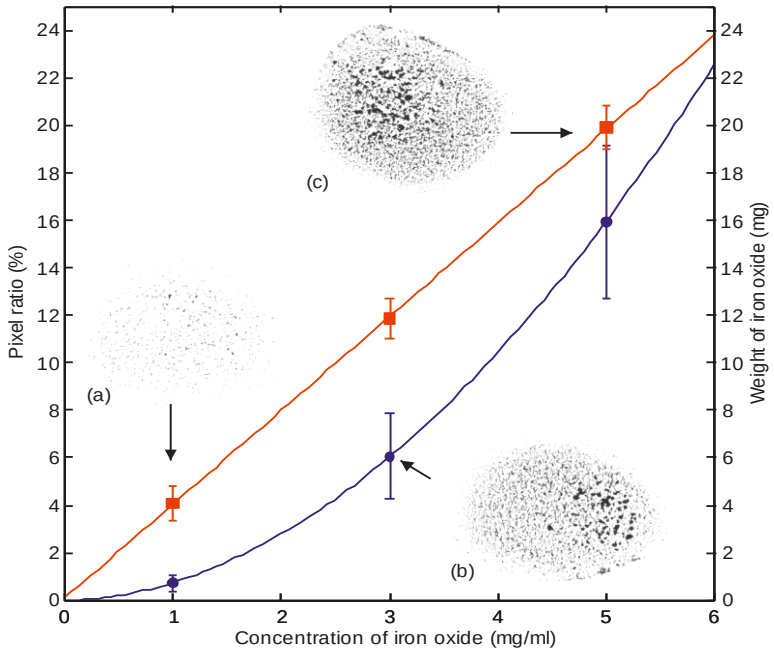

Figure 3.7: The graph depicts the consistency of the number of magnetic particles in a 5-µL droplet dispensed in 10 samples through pixel ratio percentage (blue circle) and also the weight (red square) of magnetic particles in a 5 ml droplet for 3 different concentrations. Inset: the images of magnetic particles left after the evaporation for concentration of (a) 0.001 g/ml, (b) 0.003 g/ml, (c) 0.005 g/ml.

3.4 Magnetic actuation on the damping of floating liquid marble on aqueous with different viscosity

This was a continuation work on the dynamic study of the floating liquid marble from Section 3.3. We investigated how the frictional force, inertia and effective surface tension of the marble affect the damping of the marbles when the horizontal driving magnetic force was removed. The variable parameters were the viscosity of the medium in which the marble floats on, speed and the volume of the marble. We related our findings to the underdamped harmonic oscillation model. From the experimental results, we determined the viscous damping coefficient and magnetic force constant which can then be used to evaluate the friction correction factor to the Stokes drag and the damping ratio. The driving magnetic force was estimated quantitatively.

3.4.1 Experimental setup

Figure 3.8 shows the experimental platform for the liquid marble on a solid platform. As this was a continuation of the floating liquid marble work done in Section 3.3, the setup was rather similar. The setup consisted of the PMMA holder, the polystyrene container, a bigger

permanent magnet and the programmable x-y stage. The holder was made of 4.5-mm thick PMMA plates and had a slit to hold a 1.5-mm thick PMMA plate for positioning the 10 x 10 cm polystyrene container. The water levels to be filled were marked with a permanent marker on the polystyrene container. In this work, a cylindrical permanent magnet (Neodymium, a diameter of 10 mm and a height of 5 mm) was fixed on a programmable x-y stage. The permanent magnet was placed below the container as a tool to move the floating liquid marble. This magnet was fixed at a distance of 8 mm away from the liquid marble. We used a vernier caliper to accurately adjust the distance, taking into account the combined thickness of 2.5 mm of the PMMA plate and the polystyrene container.

The x-y stage was a motorized linear actuator (Zaber Technologies T-LS28M) with built-in controllers. The actuator has a travel range of 28 mm, a maximum speed of 6.5 mm/s and a minimum speed of 0.93 μm/s. The linear motion of the actuator was controlled by the Zaber Console software. Codes were programmed to define the velocity of the actuator. The actuator was linked to a personal computer (PC) through a RS-232 port. The actuator allowed a programmable and smooth motion of the permanent magnet in both directions.

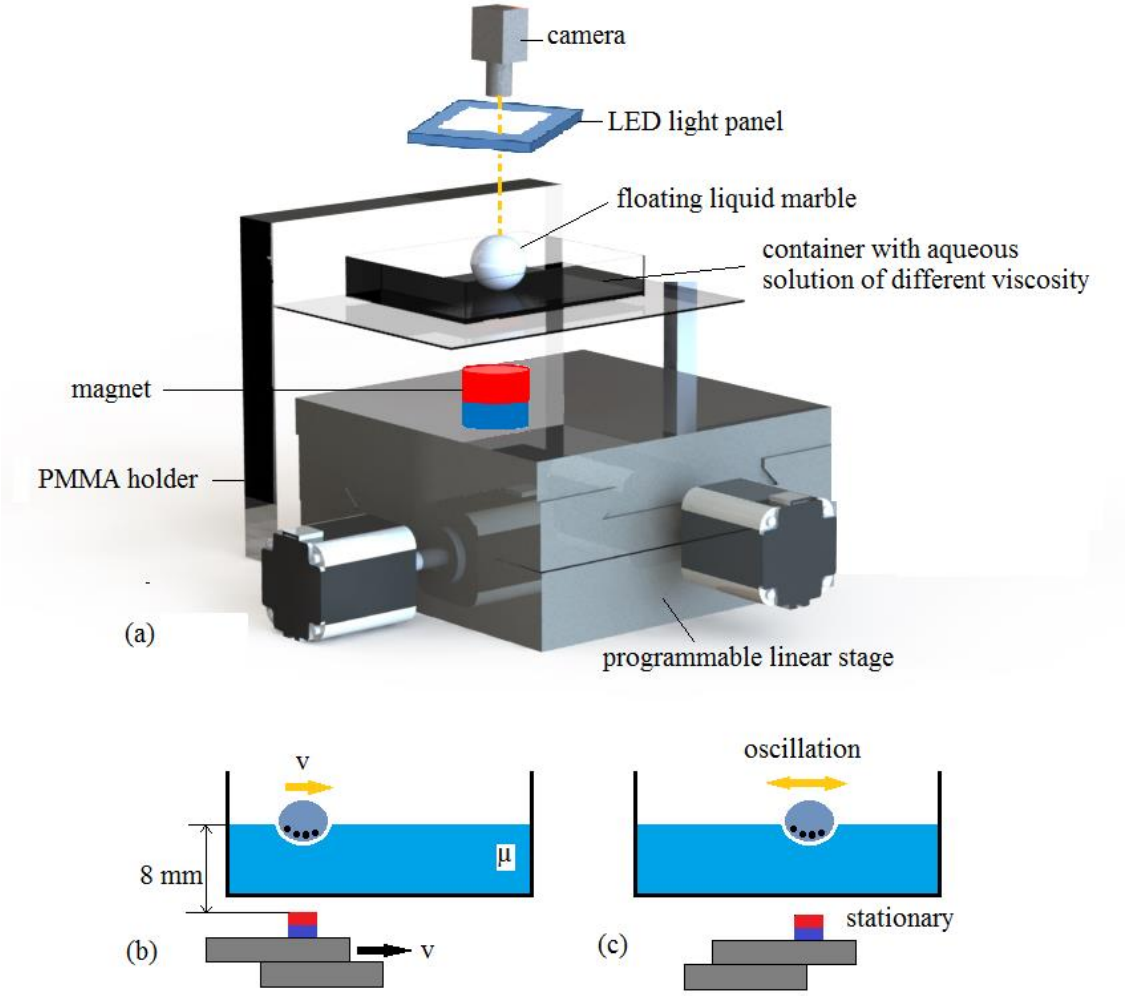

Figure 3.8: (a) Experimental setup; (b) The magnet initiates the movement of the floating liquid marble to the right. The parameters of the experiments are the velocity of the magnet, *v*, viscosity of the medium, μ and the volume of the liquid marble, *V*; (c) The magnet stops and the oscillation of the marble is observed and captured by the camera.

The experimental setup facilitated video capturing of the moving liquid marble. The video of the floating marble was recorded and further processed to examine the damping motion. This time, we placed the camera right above the marble with an attached LED light panel. The floating marble was lit with the LED light source to create a large contrast between the marble and its surrounding. The images were captured by a USB camera (Edmund Optics Inc, Singapore) with an adjustable lens (AF Micro Nikkor 60 mm f/2.8D). The camera software (uEye cockpit, IDS, Germany) was set to record the motion with 33 frames per second (fps) in a single movie file. In the subsequent image-processing step, the frames were separated and evaluated individually using ImageJ (National Institutes of Health, USA) and a custom-written program in Matlab (Mathworks, USA), to obtain an quantitative assessment of the motion (displacement,velocity and acceleration) of the floating marble as shown in Figure 3.9.

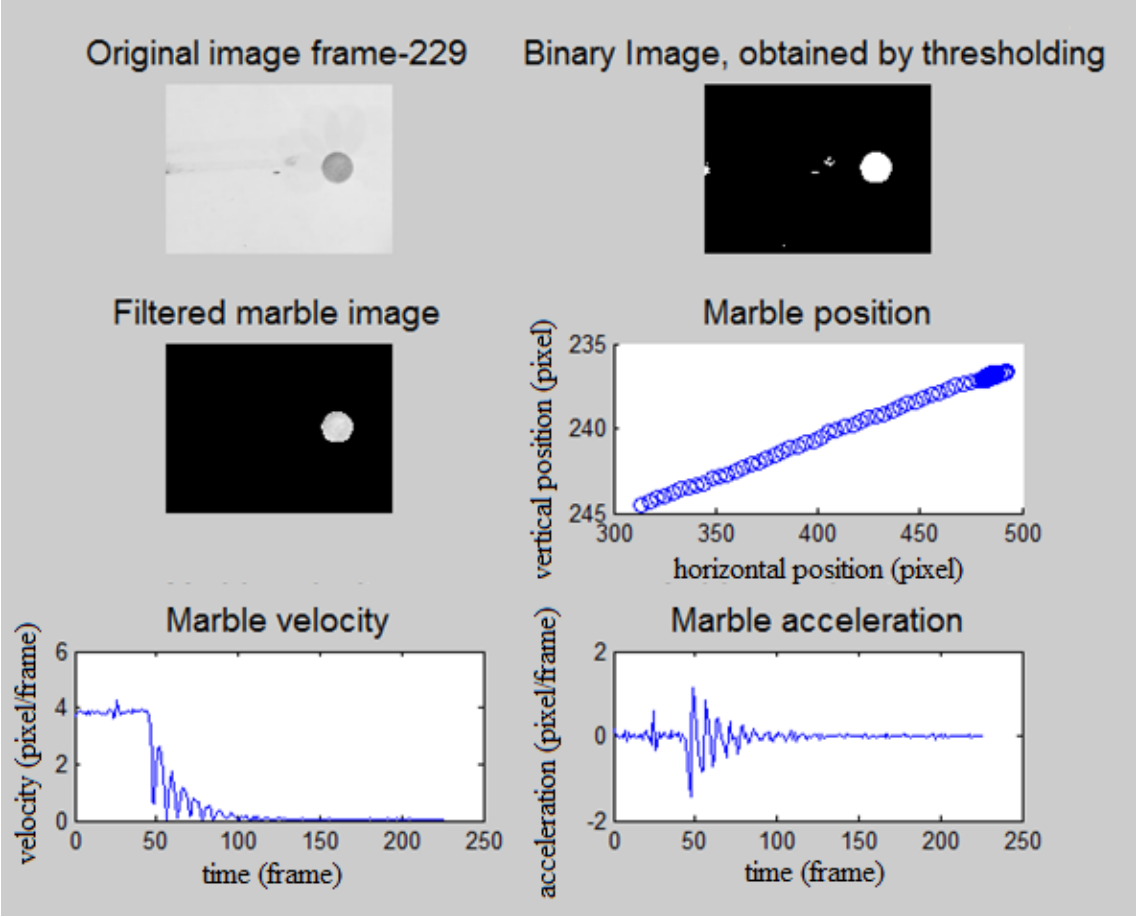

Figure 3.9: Quantitative assessment of the motion (displacement, velocity and acceleration) of the floating marble. Datas on axes are in pixels which will then be converted to the suitable metric units.

In the experiments, solutions of different viscosity were filled into the container till they reached the second marked level, representing 8mm distance from the magnet. The medium used was a mixture of 50 ml deionised water with 5ml, 10ml and 15ml of glycerol respectively. This will make up about 11.24 %, 20.21% and 27.53 % in weight of glycerol. The dynamic viscosities of the solutions were 1.3424 mPa.s, 1.7530 mPa.s and 2.2438 mPa.s respectively. To ensure consistency, all the experiments were performed in a laboratory with an ambient temperature of 20 °C.

A 1μL magnetised liquid marble was carefully placed into the container. The floating liquid marble automatically aligned itself to the centre of the permanent magnet. The magnet was programmed to move in one direction with a pre-set amplitude of 19.84 mm and 4 speeds ranging from 0.93 mm/s to 3.72 mm/s. Then the magnet was stopped and the oscillation of the floating marble was observed. The experiment was repeated for the different volumes of droplet (5 μL and 10 μL) and different viscosity of the medium (11.24 %, 20.21% and 27.53 % in weight of glycerol). The concentration of iron oxide in the droplets was fixed at 0.005 g/ml. The oscillating motions of the floating marble when the magnet was stopped were recorded and

analysed for each volume or viscosity of the medium and its corresponding speed. The Matlab program then processed the video and measured and tracked the centroid of the floating marble as it moved and stopped with the permanent magnet.

3.4.2 Preparation of liquid marble

The preparation was similar to the one described in Section 3.3.2. In this work, we only used liquid marble formed by deionised water containing 0.05 g/ml concentration of iron oxide powder.

3.5 Conclusion

In Section 3.2, we had outlined the magnetically-controlled work on a solid hydrophobic platform. A microdroplet containing hydrogen chloride (HCl) and iron oxide was magnetically-actuated by an external permanent magnet to merge with a stationary sodium hydroxide (NaOH) droplet on a Teflon-coated planar surface. The objective of the work is to study the effect of the volume of droplets, the speed of the external magnet and the iron oxide concentration to the mixing time and the amount of the heat being released. The results are analysed in the next chapter. The enthalpy values will be evaluated based on the measured peak temperature. The outcome of this study will be used for the design of a low-cost droplet-based microcalorimeter.

In Section 3.3, the sliding motion of a magnetically actuated floating marble on water was studied. The magnetic force and the frictional force acting on the floating liquid marble determined the horizontal movement of the marble. We experimentally evaluated the parameters that affect the motion of a floating liquid marble in terms of displacement and velocity such as the volume concentration of magnetic particles, the speed and the flux density of the driving permanent magnet. With these data, we can then determine the suitable operating conditions for the actuation as well as the critical points where the liquid marble no longer follows the permanent magnet. We subsequently can derive the scaling laws for the actuation parameters in the next chapter.

Section 3.4 showed the continuation work on the dynamics of the floating liquid marble in Section 3.3. Instead of water as the carrier liquid, we mixed a volume of glycerol with water with 3 viscosities. We focussed on the damping motion of the marble when the horizontal driving magnetic force was removed. In the next chapter, we will look into the theory of the underdamped harmonic oscillation model to relate the motion of the marbles in our work. We will use the experimental results to determine the viscous damping coefficient and magnetic force constant to evaluate the friction correction factor and damping ratio. With these data, we can estimate the driving magnetic force quantitatively.

Chapter 4: Results and Analysis

4.1 Introduction

In this chapter, the results of the experiments are analysed and presented concisely in the graphs to depict the behaviour of the magnetic actuations for each experimental situation.

4.2 Magnetic actuation of droplet on a hydrophobic platform and merging of acid-base for calorimetric measurement

The platform for this magnetically-controlled work is on a Teflon-coated planar surface. In this experiment, we investigated the mixing time between hydrogen chloride (HCl) filled iron oxide merging with a stationary sodium hydroxide (NaOH) droplet under the influence of the magnetic field. We compared the mixing time of the reactive droplets and the unreactive droplets (using food dye). Different concentrations of iron oxide were tested for the HCl droplet. As the permanent magnet moved towards the stationary droplet, the iron oxide particles followed the magnet and dragged along the HCl droplet to coalesce with the stationary droplet.

In our experiments, three parameters were varied: mixing speeds (1.86 mm/s, 2.79 mm/s, 3.72 mm/s and 4.65 mm/s), concentration of iron oxide (0.010 g/ml, 0.020 g/ml and 0.040 g/ml) and volumes of droplets (1 µL, 5 µL and 10 µL). The effects of these parameters on the mixing time, peak temperature and cooling time were investigated. The objective of the investigation is the optimisation of a suitable condition for micro calorimetric measurements.

4.2.1 Mixing time of reactive and non-reactive droplets

Yeh et al. [45] performed a comparison of the mixing time between passively merging reactive droplets (NaOH and phenolphthalein) and also non-reactive droplets using blue and yellow dye. After merging, non-reactive droplets mixed through slow diffusion and were two orders of magnitudes slower than the reactive droplets. They observed that for reactive droplets, the reaction promoted rapid growth of instabilities within the merged droplet leading to rapid and complete mixing. De Bruyker et al. [30] achieved 10-fold increase in mixing rate through magnetic micro-stirring as compared to the one directional electrostatic mixing.

With the aid of the back and forth movements by magnetic, we expected to improve the mass transport within the merged droplet. Figure 4.1 shows the mixing time of the reactive and non-reactive droplets, respectively. In both cases, the mixing time reduced with the increasing speed of the magnet and the decreasing volume of droplets. Figure 4.1(a) shows that the mixing time reduced when speed increased for droplets of 5 µL and 10 µL. Droplets of 1 µL followed

the same trend except for an outlier at the speed of 3.72 mm/s. Figure 4.1(b) shows that mixing time decreased with increasing speed for all droplet volumes. There was an outlier in the case of the 5 µL droplets at the speed of 2.79 mm/s. The mixing time of the reactive droplets was about 7 to 12 times less than the non-reactive droplets as expected due to hydrodynamic instabilities [43, 44].

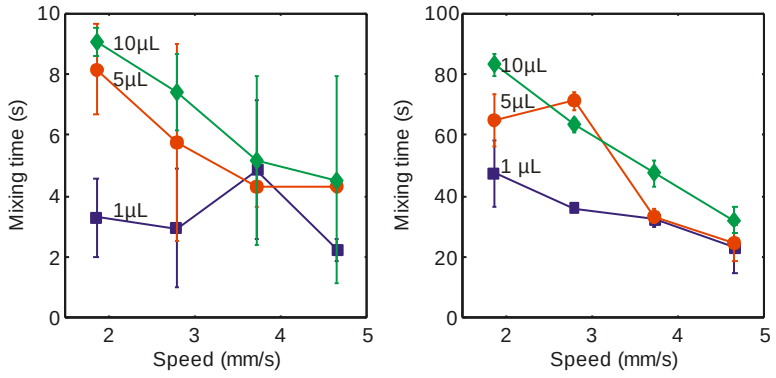

Figure 4.1: Mixing time of two droplets of different volumes: (a) reactive droplets and (b) non-reactive droplets, filled with 0.010 g/ml concentration of iron oxide, moving at four different speeds.

4.2.2 Effects of concentration of iron oxide and mixing speed on temperature rise and cooling time

A micro calorimetric measurement requires the detection of the released heat without significant loss to the surroundings. Yeh et al. [45] concluded that two reactive droplets can accumulate an intense heat of reaction if the coalescence of the droplets occurs in a small interfacial area. The interfacial area is small when both droplets have the same volume. Thus, we selected the same volume for both droplets in this experiment. The concentrations of iron oxide were varied as 0.010 g/ml, 0.020 g/ml and 0.040 g/ml for the HCl droplet to see the effects in the temperature peaks T_0 of the exothermic reaction. Figure 4.2 shows the temperature rise and also the cooling time constant τ of the neutralisation temperature response:

$$T(t) = T_o e^{-\frac{t}{\tau}} \qquad (4.1)$$

where *T(t)* is the instantaneous temperature at time *t*. Figure 4.3 shows that the peak temperature increased with increasing mixing speed for all the concentrations. The cooling time decreased with increasing speed for the concentrations of 0.010 g/ml and 0.020 g/ml but did not show a similar trend for the 0.040 g/ml. The higher content of iron oxide may affect the heat transfer process in the droplet creating cooling fluctuations in the droplet.

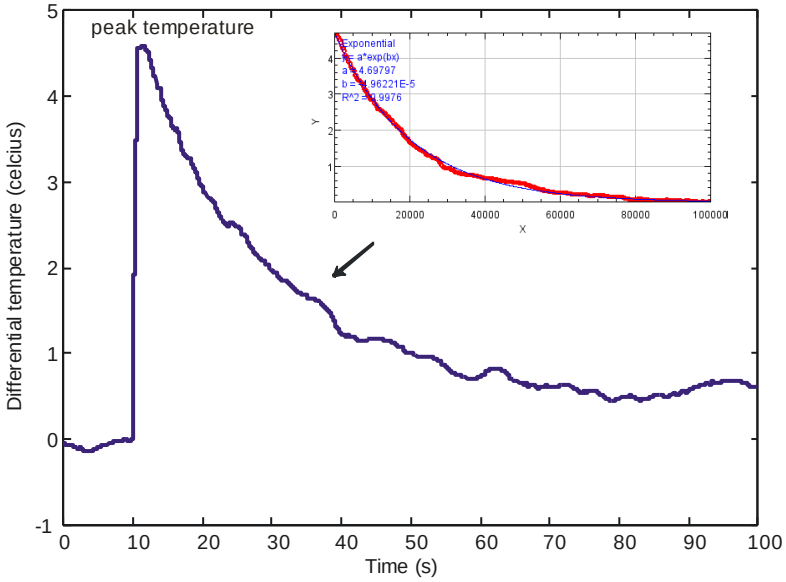

Figure 4.2: Relative temperature over time after the coalescence of two reactive droplets. The inset (red curve): Using the curve fitting tool for exponential datas, the curve of the graph is used to evaluate the peak temperature and the time for the droplets to reach equilibrium after reaction.

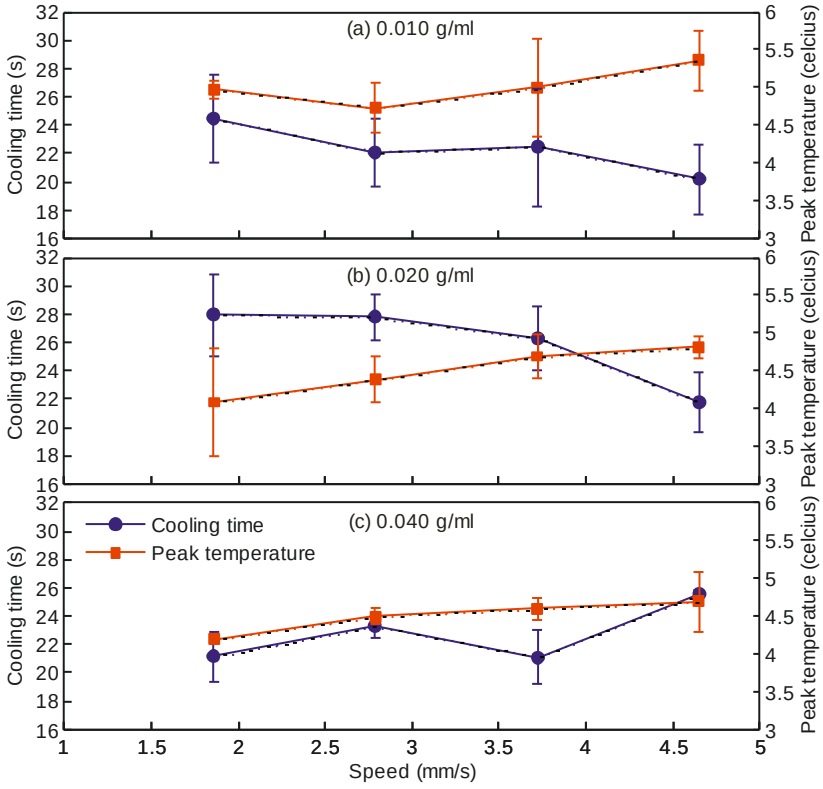

Figure 4.3: Cooling time and peak temperature detected upon coaslescence of 5 µL droplets as a function of speed at a concentration of iron oxide of (a) 0.010 g/ml, (b) 0.020 g/ml and (c) 0.040 g/ml.

We also varied the volume of the HCl and NaOH from 1µL to 10µL, while the concentration of the iron oxide and the speed were kept constant at 0.010 g/ml and 4.65 mm/s,

respectively. Figure 4.4 indicates that a larger droplet took a longer time to cool down. The measured peak temperature stabilised from 5 µL to 10 µL. The peak temperature was directly proportional to the enthalpy of neutralisation. The stable peak temperature obtained for droplets of 5 µL and 10 µL indicated that they were the optimum volumes for the detection of the accumulated heat of neutralisation. Furthermore, the peak temperature did not vary as a function of volume.

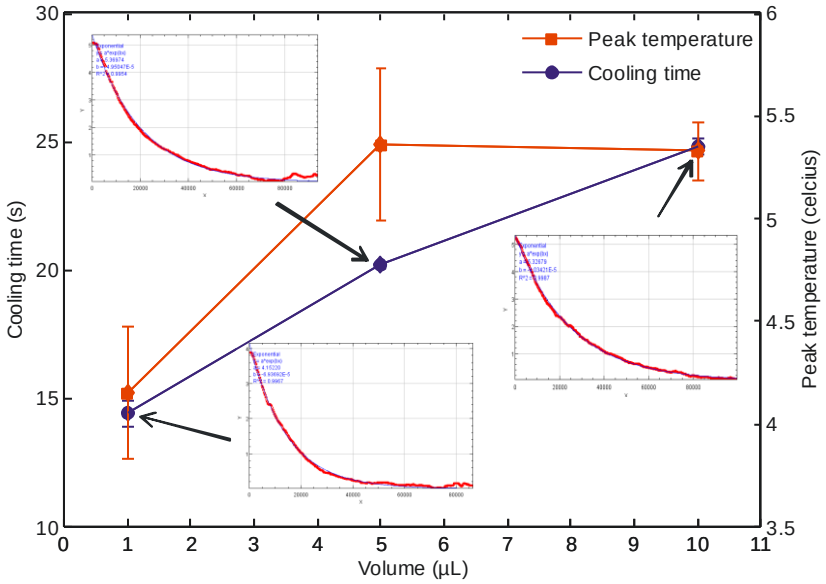

Figure 4.4: Cooling time and peak temperature increase as a function of volume, for droplets with 0.01 g/ml iron oxide concentration and at a speed of 4.65 mm/s.

4.2.3 Determining the enthalpy of neutralisation

We chose HCl and NaOH as the test samples because the reaction is strong and exothermic. Besides giving a highly detectable temperature rise upon reaction, there is sharp colour change in the phenolphthalein between pre-reaction and post-reaction. The chemical equation is given as:

$$HCl + NaOH \rightarrow NaCl + H_2O \qquad (4.2)$$

The classical method of calculating the molar enthalpy of neutralisation ΔH is to measure the temperature rise from the neutralisation of the acid and alkaline. The known enthalpy value for neutralisation of HCl and NaOH is -57.7 kJ/mol at room temperature, as documented by Zalts et al. [124]. However, there will be a net flux of heat dissipated from the experimental setup, which results in enthalpy values with less than expected absolute values. We calculated ΔH using:

$$\Delta H = \frac{-(m_d \cdot c_{sol} + C_{sys})\Delta T}{M_{H_2O}} \qquad (4.3)$$

where m_d is the mass of droplets, c_{sol} is the specific heat capacity of solution, c_{sys} is the heat capacity of the system, ΔT is the temperature change and M_{H2O} is the moles of water produced in the experiment. We assumed the density of each dilute aqueous solution to be equivalent to the density of water (1.00 g/ml) and c_{sol} to be similar to the specific heat capacity of water (4.18 J/^{0}Cg). m_d is 10 mg for droplets of 5 µL volume each. In the net ionic reaction:

$$OH^-_{(aq)} + H^+_{(aq)} \rightarrow H_2O \qquad (4.4)$$

M_{H2O} is calculated to be 5 µmol. We used the known enthalpy value to estimate c_{sys}. Using this value, ΔH was estimated for other measurements.

Figure 4.5 shows the deviation of enthalpy values, δH for different speeds of the permanent magnet and also the concentration of iron oxide in the droplet. The concentration of the iron oxide did not show any trend in particular, confirming that the reaction between iron oxide and HCl was negligible. However, the higher the speed the more heat was released indicating the correlation between better mixing and better reaction.

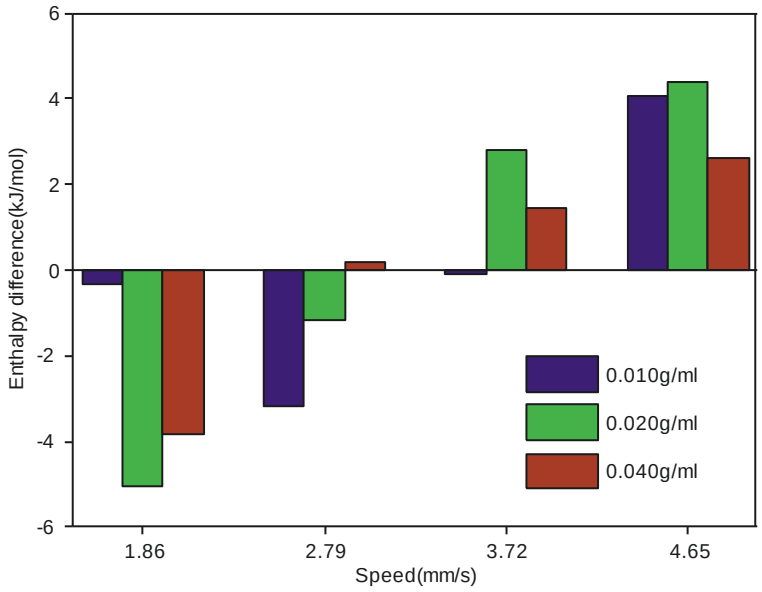

Figure 4.5: Enthalpy difference between measured and known enthalpy of neutralisation for 5 µl droplets of NaOH and HCl

4.3 Magnetic actuation for floating liquid marble on water

In this experiment, the sliding motion of a magnetically actuated floating marble on water was studied. Firstly, we looked into the forces acting on the floating liquid marble that determine the horizontal movement of the marble. Then we evaluated the parameters that affect the motion of the marble such as the volume concentration of magnetic particles, the speed and the flux density of the driving permanent magnet. Suitable operating conditions for the actuation were determined as well as the critical points where the liquid marble lagged behind. We derived the scaling laws for the actuation parameters.

4.3.1 Forces acting on the magnetic floating marble

When the liquid marble was transferred to the water container, it floated on the water surface. The vertical component of the magnetic force and the weight of the liquid marble balance the upward acting buoyancy force and surface tension force. The vertical non-magnetic forces were analysed and discussed in the recent work by Ooi et al.[129]. For the actuation scheme of the present work only horizontal forces were considered.

Assuming the surrounding medium is diamagnetic, the driving force acting on a floating marble within the field of the permanent magnet is given by [42, 130]

$$F_{\mathrm{m}} = \frac{V\chi}{\mu_o} B \frac{\mathrm{d}B}{\mathrm{d}x} \qquad (4.5)$$

where F_{m} is the magnetic force, V is the volume of the iron oxide, χ is the magnetic susceptibility of the floating marble, μ_0 is the permeability of vacuum and B is the magnetic flux density. Since the marble volume in our experiments was fixed, the magnetic force scaled with the flux density and the flux density gradient of the magnetic field and the concentration of iron oxide inside the marble:

$$F_{\mathrm{m}} \propto VB \frac{\mathrm{d}B}{\mathrm{d}x} \qquad (4.6)$$

Thus, in the subsequent experiments, varying the concentration of iron oxide and the distance between the marble and the permanent magnet allowed the adjustment of the magnetic force.

The magnetic flux density of the magnet, B was measured with a handheld commercial gaussmeter (GM07, measurement range from 0 to 3 T, Hirst Magnetic Instruments Ltd, UK). Figure 4.6 shows the measured magnetic flux densities with increasing distance of the gaussmeter probe from the magnet. The magnet was mounted vertical onto a PMMA holder and placed on the x-y stage. Initially, the probe touched the magnet to get the maximum reading. The x-y stage was then programmed to move 0.1 mm away from the probe for each

measurement. The measured result agreed well with the theoretical estimation of the magnetic field:

$$B = \frac{B_r}{\pi}\left[\arctan\left(\frac{LW}{2z\sqrt{4d^2 + L^2 + W^2}}\right) - \arctan\left(\frac{LW}{2(D+d)\sqrt{4(D+d)^2 + L^2 + W^2}}\right)\right] \quad (4.7)$$

where B_r is the remanence field, L is the length, W the width and D the height of the magnet, d is the distance from the magnet surface.

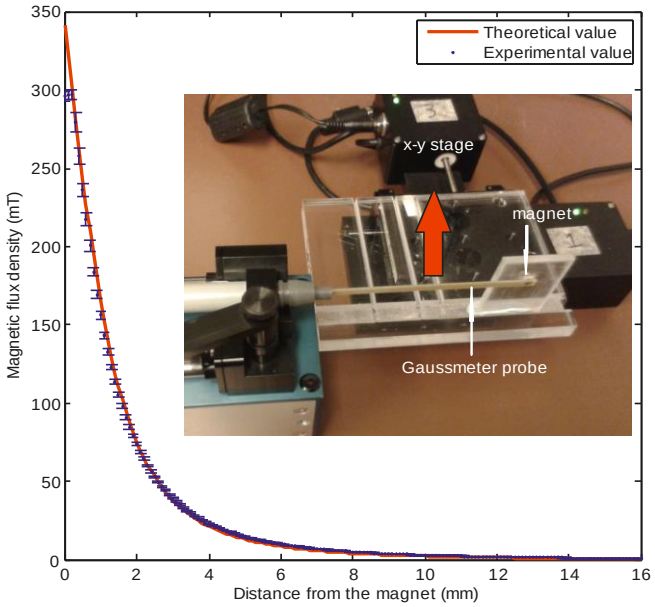

Figure 4.6: Magnetic flux density versus the distance to the permanent magnet. Points with error bars are measurement data, line is the plot of Equation (4.7). Inset: Setup of the measurement.

From the experimental data in Figure 4.6 and equation (4.7), the relationship between flux density B and the distance d can be simplified to the scaling relationship $B \propto \frac{1}{d}$. Thus, the distance of the floating marble from the permanent magnet d as well as the concentration of iron oxide c will affect the driving magnetic force of the marble. We hypothesised that if d increases and c decreases, the magnetic force becomes weaker. As a result, the floating marble will start to lag behind the moving permanent magnet until reaching a limit and dislodge.

For a sphere with a radius r moving on a planar air-water interface, the friction force can be calculated by adding a dimensionless correction factor to the Stokes friction:[131]

$$F_f = 6\beta\pi r\mu v = Cr\mu v \quad (4.8)$$

where β is the correction factor, μ is the dynamic viscosity of water (approximately 1 mPa·s) and v is the instantaneous marble velocity, the friction factor C=6$\beta\pi$ is a product of the

combined dimensionless coefficients. Petkov et al. determined β to be 0.54 for a small hydrophobised glass sphere floating with a large three-phase contact angle [131]. The friction factor C was therefore 10.18 in this case. Ooi et al. indirectly determined $C \approx 10$ as the starting condition for scaling relationships of a self-propelled floating liquid marble within a geometric constraint [24].

Assuming that the contact radii of floating magnetic marbles influenced by the vertical component of the magnetic force have similar orders of magnitude as non-magnetic ones, the marble radius r_0 is in the order of 10^{-4} m for the volumes used. The speed v is in the order of 10^{-4} to 10^{-3} m/s. The viscosity μ is in the order of 10^{-3} Pa·s. The friction factor C is in the order of 10. Therefore, the friction force is estimated to be in the orders of 10^{-9} to 10^{-10} N. The scaling relationship between friction force and the speed is simplified as:

$$F_{\mathrm{f}} \propto v \qquad (4.9)$$

The relationship (4.9) indicated that increasing the speed of the magnet will increase friction force F_{f} causing the floating marble to lag behind the moving permanent magnet and eventually to dislodge.

The impact of the vertical forces can be shown via usage of different magnetite concentration. As the concentration increased, the vertical magnetic force experienced by the marble increased. With an increasing downward force, the effective Bond number Bo_{eff} is expected to increase as well, since:

$$\mathrm{Bo}_{eff} = \frac{\rho_{eff} a(F_v,g) r^2}{\gamma_{eff}} \qquad (4.10)$$

where ρ_{eff} is the effective density of the marble, a is the resultant acceleration caused by the gravitational g and the vertical magnetic force F_v, r is the radius of the undeformed spherical marble, γ_{eff} is the effective surface tension of the marble. Ooi et. al's recent study [129] showed that the dimensionless contact radius $r_0^* = r_0/r$ of a small floating marble approximately scaled with $\mathrm{Bo}^{1/2}$. Therefore, increasing the Bond number will increase the contact radius. For a sphere straddling between two fluids, the Stokes friction force F_{f} scaled with the contact radius r_0. The scaling relationship of friction force to the effective Bond number can be written as:

$$Bo_{eff}^{1/2} \sim r_0^* = \frac{r_0}{r} \therefore r Bo_{eff}^{1/2} \sim r_0 \qquad (4.11)$$

$$F_f \sim r_0 \sim r Bo_{eff}^{1/2} = r^2 \sqrt{\frac{\rho_{eff} a(M(c)B,g)}{\gamma_{eff}}} \qquad (4.12)$$

Hence increasing the magnetite concentration will increase the friction force. However, the horizontal magnetic force also increased with the magnetite concentration which acted to compensate for the increasing friction force. The mutual cancellation reduced the impact of the vertical force.

4.3.2 Sliding of the floating liquid marble

Because the steady motion of the floating marble resulted from the balance between the horizontal component of the magnetic force and the friction force, both magnetic force and friction force were varied in our experiment to determine the operation map. We investigated the movement of the floating marble in terms of displacement and velocity with the variation of each parameter. According to equation (4.6), the magnetic force can be tuned by adjusting the flux density B and the flux density gradient dB/dx through the distance d between the magnet and the marble. The magnetic force will decrease with the increasing distance. Another way to vary the magnetic force was to change the volume V of the iron oxide particles. A higher concentration will result in a larger volume of iron oxide for actuation. According to equation (4.9), the friction force was adjusted with the speed v of the permanent magnet. The higher the speed, the larger was the friction force.

Three parameters were varied in our experiment: five different distances of floating marble from the magnet d ranging from 6 mm to 16 mm, three concentrations of iron oxide c ranging from 0.001 g/ml to 0.005 g/ml and nine magnet velocities v ranging from 0.465 mm/s to 4.19 mm/s.

If the permanent magnet was slow and closed to the marble, the resulting strong magnetic force caused the floating marble to slide and to follow the magnet with the same velocity. For the potential use of this system as a digital microfluidics system, this is the preferred operating condition. Figure 4.7(a) shows a smooth marble movement from stationary to a distance of 4.96 mm before turning back to the other direction, as programmed for the magnet. Figures 4.7(b) and 4.7(c) show the behaviour of the marble with increasing distance from the magnet, while the iron oxide concentration and the velocity were fixed at 0.003 g/ml and 0.465 mm/s, respectively. At d=10 mm, the marble starts to lag behind the magnet. A further distance of d=16 mm, the marble dislodged from the movement of the permanent magnet. Although the initial driving force is big enough to induce a momentum to the marble, however the friction force was dominant and the marble cannot keep up with the magnet.

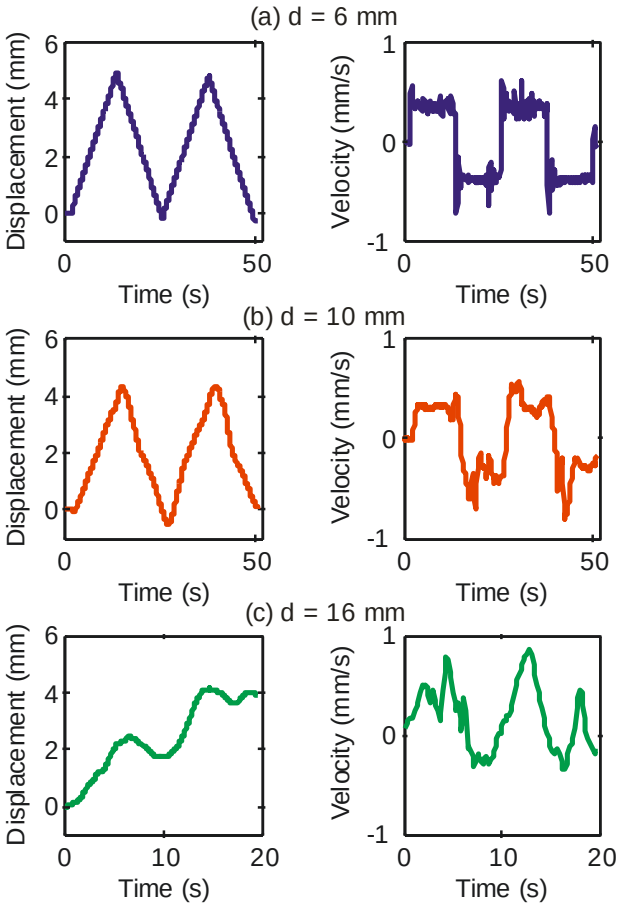

Figure 4.7: Measured displacement and velocity of a 5 μL floating liquid marble with an iron oxide concentration of 0.003 g/ml and a velocity of the permanent magnet of 0.465 mm/s with increasing distance from the magnet; (a) d=6 mm (B=10.1 mT); (b) d=10 mm (B=3.09 mT); and (c) d=16 mm (B=0.96 mT)

Figure 4.8 shows the representative behaviour of the marble with varying concentration of the iron oxide. The distance from the magnet was chosen as d=10 mm, and velocity was fixed at v=1.86 mm/s. The marble slid along with the magnet at the concentrations of 0.003 g/ml and 0.005 g/ml. However, at the concentration of 0.001 g/ml, the floating marble no longer follows the moving magnet.

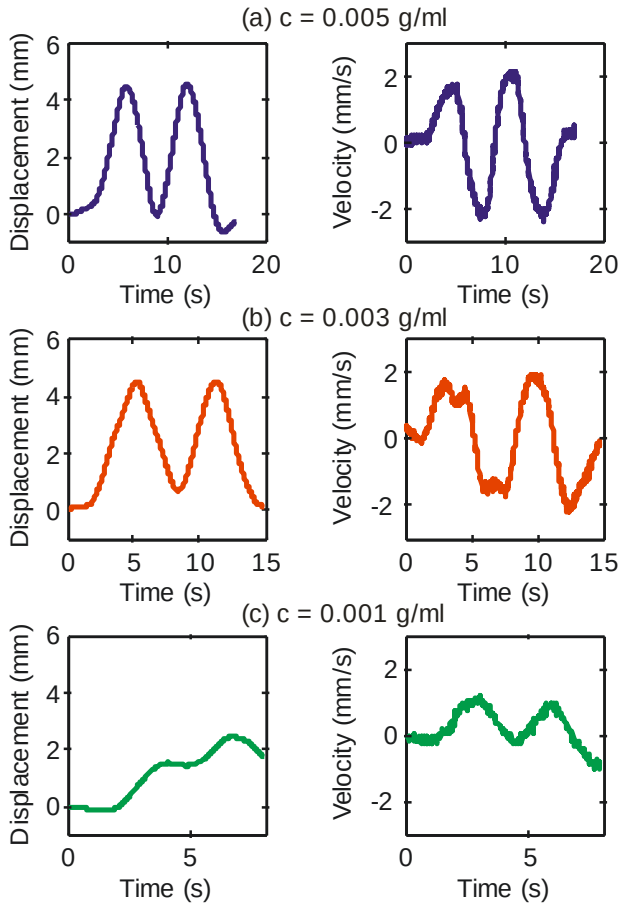

Figure 4.8: Measured displacement and velocity of a 5 µL floating marble at a distance of 10 mm from the permanent magnet and a velocity of the permanent magnet of 1.86 mm/s with decreasing iron oxide concentration; (a) *c*=0.005 g/ml; (b) *c*=0.003 g/ml; and (c) *c*=0.001 g/ml

Figure 4.9 shows the representative behaviour of the marble at the highest velocity 4.19 mm/s. At this high velocity, the friction force became dominant and the marble lagged behind. The marble slid with the magnet with velocity ranging from 0.465 mm/s to 1.86 mm/s. Beyond that, the marble lagged behind until it started to dislodge at 4.46 mm/s.

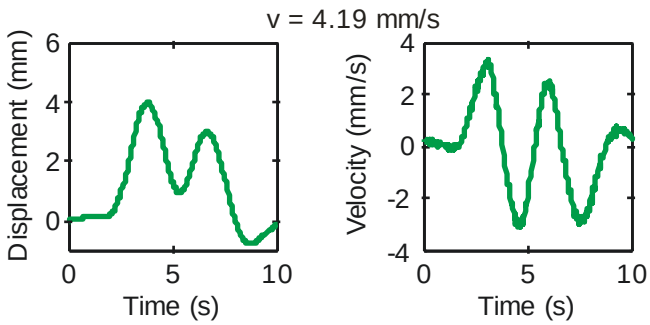

Figure 4.9: Measured displacement and velocity of a 5 µL floating marble at a distance of 10 mm from the permanent magnet and with an iron oxide concentration of 0.003 g/ml at the velocity of 4.19 mm/s

As a summary, Figure 4.10 shows the operating maps of the floating marble in the corresponding *d*-*v* and *c*-*v* spaces. Three zones were identified: sliding, lagging and dislodgment. When $F_m \approx F_f$, the marble slid following the magnet to the preprogramed distance of 4.96 mm with the same velocity as that of the magnet. When $F_m < F_f$, the marble lagged behind and if the maximum velocity was reached, it will dislodge from the influence of the magnet. Figures 4.10(a) and 4.10(b) show the operating map of two different concentrations of iron oxide. A higher concentration showed the better control of the movement when the distance of the marble from magnet and speed increased. As discussed previously, a higher concentration caused a higher friction force due to larger vertical magnetic force and the resulting larger contact radius (equation (4.12)). However, higher concentration also led to a higher driving horizontal magnetic force. As a result, the change in concentration did not significantly affect the operation map in *d*-*v* space. Figure 4.10(c) shows the operation map in the *c*-*v* space, a concentration of 0.001 g/ml and below was not strong enough to let the marble follow the magnet.

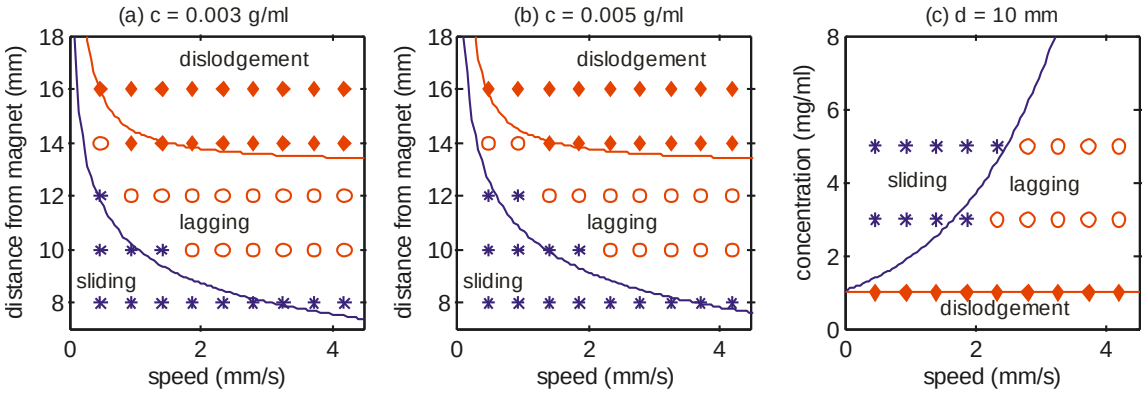

Figure 4.10: Operating map with the three regimes sliding (✸), lagging (♦) and dislodgement (○). (a) Distance from magnet and magnet speed space at *c*=0.003 g/ml; (b) Distance from magnet and magnet speed at *c*=0.005 g/ml; and (c) Iron oxide concentration and speed space.

4.3.3 Scaling Analysis and Operating Regions

At the lowest magnetic flux density B_{min}, the floating marble followed the magnet until the maximum velocity was reached. To simplify the equation for scaling analysis, the force balance in the sliding operating region is

$$F_m = F_f \qquad (4.13)$$

$$\alpha B_{min} = \beta v_{max} \qquad (4.14)$$

$$B_{min} = \frac{\beta}{\alpha} v_{max} \qquad (4.15)$$

where α and β are simply scaling factor. Figure 4.11 replots the sliding region data of Figure 4.10(a) and 4.10(b) with the actual flux density converted from the distance using Figure 4.6. The shaded areas represented the experimentally obtained sliding region of the marble. In this region, the driving magnetic force overcame the frictional force which allowed the marble to follow the permanent magnet where $F_{\mathrm{m}} \geq F_{\mathrm{f}}$.

A linear scaling relationship of equation (4.11) was fitted to the experimental data of Figure 4.11. To get the slope β/α, we chose the critical condition for the sliding regime for both of the concentrations. The minimum magnetic flux density of 1.98 mT and maximum velocity of 0.465 mm/s were chosen for the concentration of 0.003 g/ml. The minimum magnetic flux density of 1.98 mT and maximum velocity of 0.930 mm/s were chosen for the 0.005 g/ml concentration. The slopes were 4.26 Ts/m and 2.13 Ts/m respectively. Referring back to equation (4.6) and taking into account that the concentration of iron oxide is directly proportional to its volume, α represents the term $\frac{c\chi}{\mu_o}\frac{\mathrm{d}B}{\mathrm{d}x}$. Whilst $\frac{\chi}{\mu_o}$ remain the same for both cases, we find the product of the proportional factor and the concentration. The data in Figure 4.11(a) led to B=(4.26×0.003)v=0.013v, while the data in Figure 4.11(b) led to B=(2.13×0.005)v=0.011v. The slight difference may be attributed to the term dB/dx. Thus, discounting the concentration of iron oxide, the data of Figures 4.11(a) and 4.11(b) agreed relatively well.

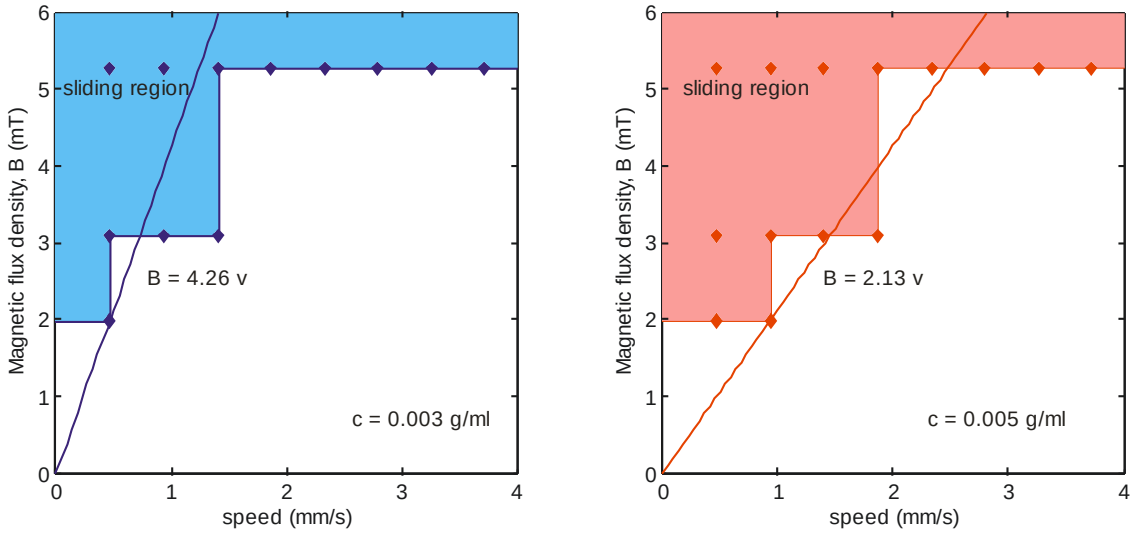

Figure 4.11: Sliding region of the floating marble in our experiments. The blue-shaded area (a) is the sliding region with the floating marble with a concentration of 0.003 g/ml and the red-shaded area (b) is the sliding region with the floating marble with a concentration of 0.005 g/ml.

4.4 Magnetic actuation on the damping of floating liquid marble on aqueous with different viscosity

In this experiment, we also investigated the magnetic actuation of floating liquid marble. This time, we varied the viscosity of the carrier liquid/medium by adding in different concentrations of glycerol to water. We used the magnet to initiate the sliding of the marble on the medium with different viscosities before stopping the magnet. Then, we recorded the horizontal damping motion of the marble when the actuation of the magnet was stopped. We looked into the theory of the underdamped harmonic oscillation model to relate the damping motion of the marbles. Other varied parameters were the volume and speed of the marble. We used the experimental results to determine the viscous damping coefficient and magnetic force constant to evaluate the friction correction factor and damping ratio. We estimated the driving magnetic force.

4.4.1 Theory on the damping effect

When the magnet moved, the liquid marble slid along on the aqueous solution in the same velocity as the magnet. Subsequently, the magnet stopped. Due to inertia and balances of force according to the Newtonian mechanics, the marble will oscillate but the movement will eventually weaken and stops. This damping of the floating liquid marble is analogous with a damped harmonic oscillation model.

The magnet created a forward magnetic force which was greater than the frictional force for the marble to start moving. When the external magnetic force was removed, the velocity of the marble decreased proportionally to the acting frictional force. The frictional force is then known as the viscous damping force. The oscillation of the marble will have exponential decay terms which depend upon a damping coefficient. Equation (4.16) and (4.17) shows the frictional damping force and damping coefficient, γ respectively:

$$F_{friction} = F_{damping} = -c\dot{x} = -cv \quad (4.16)$$

$$\gamma = \frac{c}{2m} \quad (4.17)$$

where c is the viscous damping coefficient, $\dot{x}$ and v (terms are used interchangeably) are the instantaneous marble velocity and m is the mass of the marble. In the balance of forces for a damped harmonic oscillation, Newton's 2nd law of motion stated that:

$$m\ddot{x} + c\dot{x} + kx = 0 \quad (4.18)$$

$$\ddot{x} + \frac{c}{m}\dot{x} + \omega_o^2 x = 0 \quad (4.19)$$

where $\frac{c}{m}$ is the strength of damping, undamped oscillation frequency, $\omega_o = \sqrt{\frac{k}{m}}$, k is the magnetic force constant, x is the position of the marble depending on time, $\dot{x}$ and $\ddot{x}$ are the derivatives representing velocity and acceleration of the marble depending on time. Alternatively, equation (4.19) can be written as:

$$\ddot{x} + 2\zeta\omega_o\dot{x} + \omega_o^2 x = 0 \qquad (4.20)$$

where ζ is the damping ratio. Since the marble oscillated and its amplitude reduced exponentially in time, it fitted the underdamped model. The underdamped response of the marble is then described by:

$$x(t) = ae^{-\gamma t}[\cos(\omega_1 t - \varphi)] \qquad (4.21)$$

Replacing equation (4.17) and the apparent frequency $\omega_1 = \sqrt{\omega_o^2 - \frac{v^2}{4}}$ into equation (4.21), we got

$$x(t) = ae^{-\frac{c}{2m}t}cos\left[\left(\sqrt{\frac{k}{m} - \frac{c^2}{4m^2}}\right)t - \varphi\right] \qquad (4.22)$$

We used equation (4.22) to analyse the damping graphs obtained from the experiments to estimate the value of *c* and *k*. Then we determined the damping ratio, ζ from equation (4.20) and (4.22):

$$\zeta = \frac{c}{2\sqrt{mk}} \qquad (4.23)$$

Subsequently, we evaluated the *Q* factor of the system to be:

$$Q = \frac{1}{2\zeta} \qquad (4.24)$$

Petkov et. al [131] had previously calculated the frictional force of the marble by adding a dimensionless correction factor to the Stokes friction:

$$F_{friction} = 6\beta\pi r\mu v \qquad (4.25)$$

where β is the correction factor and μ is the dynamic viscosity of the medium.

Comparing equation (4.16) and (4.25), we can relate that the viscous damping coefficient, *c*:

$$c = 6\beta\pi r\mu \qquad (4.26)$$

We used the value of the obtained *c* to find the value of β. For a 5µL marble moving on a planar air-water interface, Petkov et. al [131] and Ooi et al. [24] determined β to be 0.54 and 0.53 respectively.

4.4.2 Results and Analysis

In this work, only the horizontal forces were considered. The driving force acting on the floating liquid marble within the magnetic field of the permanent magnet is given by

$$F_{magnetic} = \frac{V\chi}{\mu_o} B \frac{dB}{dx} \qquad (4.27)$$

where *V* is the volume of the iron oxide, χ is the magnetic susceptibility of the liquid marble, μ_o is the permeability of vacuum, *B* is the magnetic flux density and d*B*/d*x* is the flux density gradient. Since the concentration of the iron oxide in a marble was fixed at 0.005 g/ml, the increase in volume/size of the liquid marble will increase the mass of the marble and will not have any significance to the horizontal component of the magnetic force. In all the experiments, the distance of the marble from the permanent magnet was fixed at 8mm. The magnetic flux density of the cylindrical magnet, *B* was measured with a handheld commercial gaussmeter (GM07, Hirst Magnetic Instruments Ltd, UK). At 8mm, *B* is 36.4 mT. Thus, the magnetic force was kept constant when the marble was moving for all experiments.

The interest of this work was to investigate how the frictional force affected the damping of the marble when the magnetic force was removed (when the magnetic actuation stops). From equation (4.25), frictional force is directly proportional to the radius of the marble, *r*, viscosity of the medium, μ and also the speed of the marble, *v* just before it stops. Since the marble was almost spherical when it floated on the medium, varying the volume of the marble changed the radius. Therefore, varying speed of the magnet, *v*, viscosity of the medium, μ and the volume of the liquid marble, *V* allowed the adjustment of the frictional force. The medium that was used to float the marble is as shown in Table 4.1. The glycerol percentage by weight, dynamic viscosity, density [132] and surface tension [133] were calculated.

Table 4.1: Aqueous solution in the container as a medium to float the marble

Medium	**Glycerol % by weight [132]**	**Dynamic viscosity,µ (mPa.s) [132]**	**Density, ρ (kg/m^3) [132]**	**Surface tension, σ (mN/m) [133]**
50ml water + 5ml glycerol	11.24	1.3424	1022.2	~71.30
50ml water + 10ml glycerol	20.21	1.7530	1042.3	70.93
50ml water + 15ml glycerol	27.53	2.2438	1059.4	~70.35

The change in the frictional force can affect the frequency of the damping oscillation, *f*, damping coefficient, *c* and the amplitude of the damping oscillation, *a*. Three parameters were varied in our experiment: four magnet speeds ranging from 0.93 mm/s to 3.72 mm/s, three viscosities of medium ranging from 1.3424 mPa.s to 2.2438 mPa.s and three volumes of liquid marble ranging from 1µL to 10µL.

As we increased the speed of the magnet, the marble slid along the medium at the similar speed. Once we stopped the magnet, the marble was somewhat pulled back by the frictional force and oscillated about the position where the magnet was directly below. We observed that at higher speed, the marble started oscillating at higher amplitude. Figure 4.12 shows the damping graphs of four scenarios with fixed volume and viscosity of the medium. The frequency of the damping and damping coefficient did not depend on the speed.

When we increased the volume of the marble, the amplitude of oscillation also increased. The frequency of damping decreased and it took a longer time to stop oscillating. Thus, we expected the damping coefficient to be higher. Figure 4.13(a) shows the exact representation behaviour of the marble when the volume increased. However, Figure 4.13(b) and 4.13(c) show constant amplitudes and slightly different frequencies for 5µL and 10µL marbles. Figure 4.13(d) shows a slight change in the amplitudes but was not significant as the difference were less than 0.02 mm.

Increasing the viscosity of the medium the marble was floating on resulted in a larger damping coefficient according to the equations (4.17) and (4.26). Figure 4.14 (a-d) shows that the marble damped faster when floating on a more viscous medium. The viscosity had no effect on the initial oscillating amplitude as it all peaked at the same range for the constant speeds. The frequency of damping was the same for 10µL marble moving at the constant speed. However, the frequency for the 1µL and 5µL marbles showed inconsistent trends.

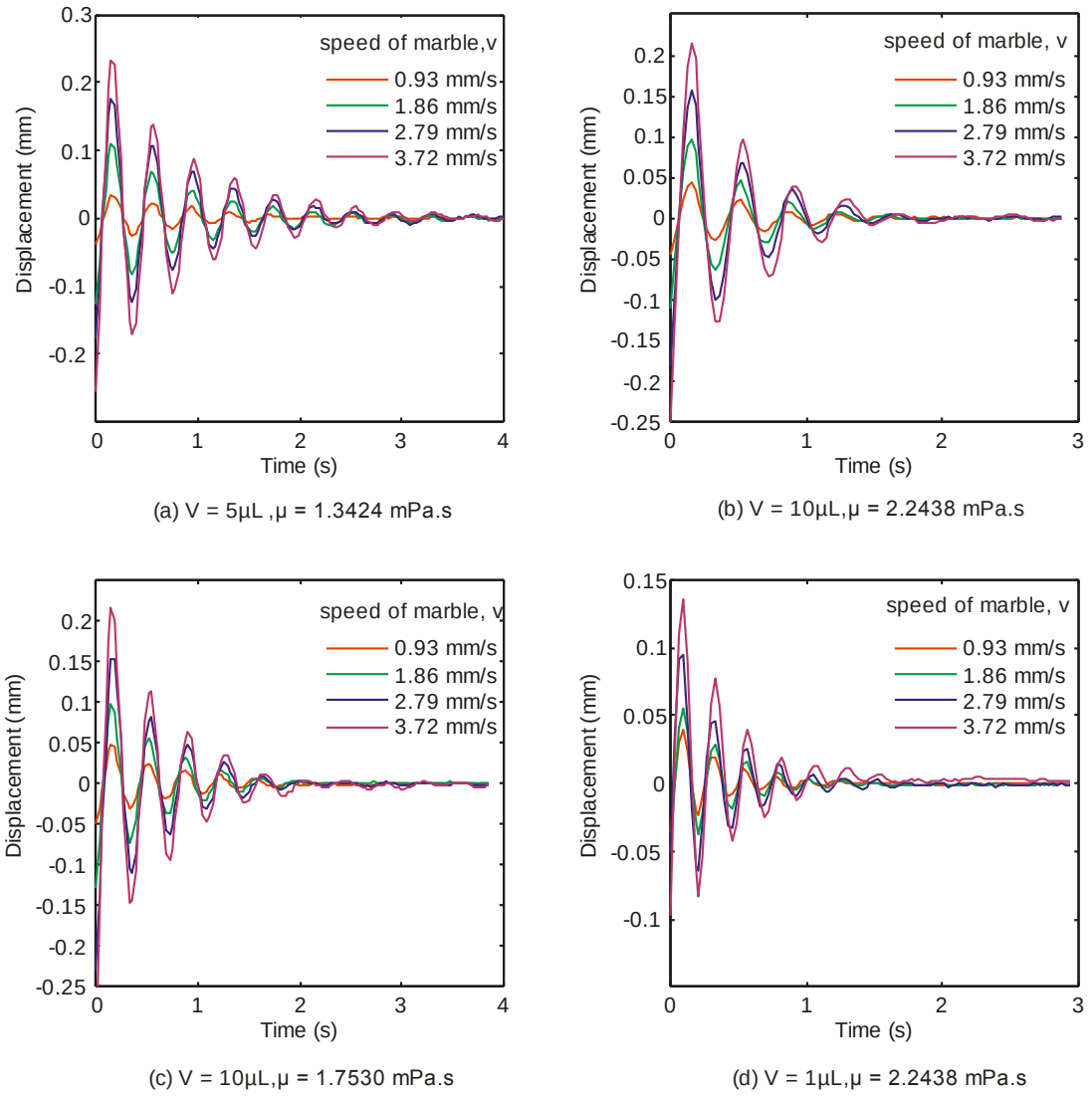

Figure 4.12: Damping graphs for (a) 5µL marble in a medium containing 11.24% glycerol by weight (dynamic viscosity = 1.3424 mPa.s); (b) 10µL marble in a medium containing 27.53% glycerol by weight (dynamic viscosity = 2.2438 mPa.s); (c) 10µL marble in a medium containing 20.21% glycerol by weight (dynamic viscosity = 1.7530 mPa.s) and (d) 1µL marble in a medium containing 27.53% glycerol by weight (dynamic viscosity = 2.2438 mPa.s), with varying speeds of 0.93 mm/s, 1.86 mm/s, 2.79 mm/s and 3.72 mm/s.

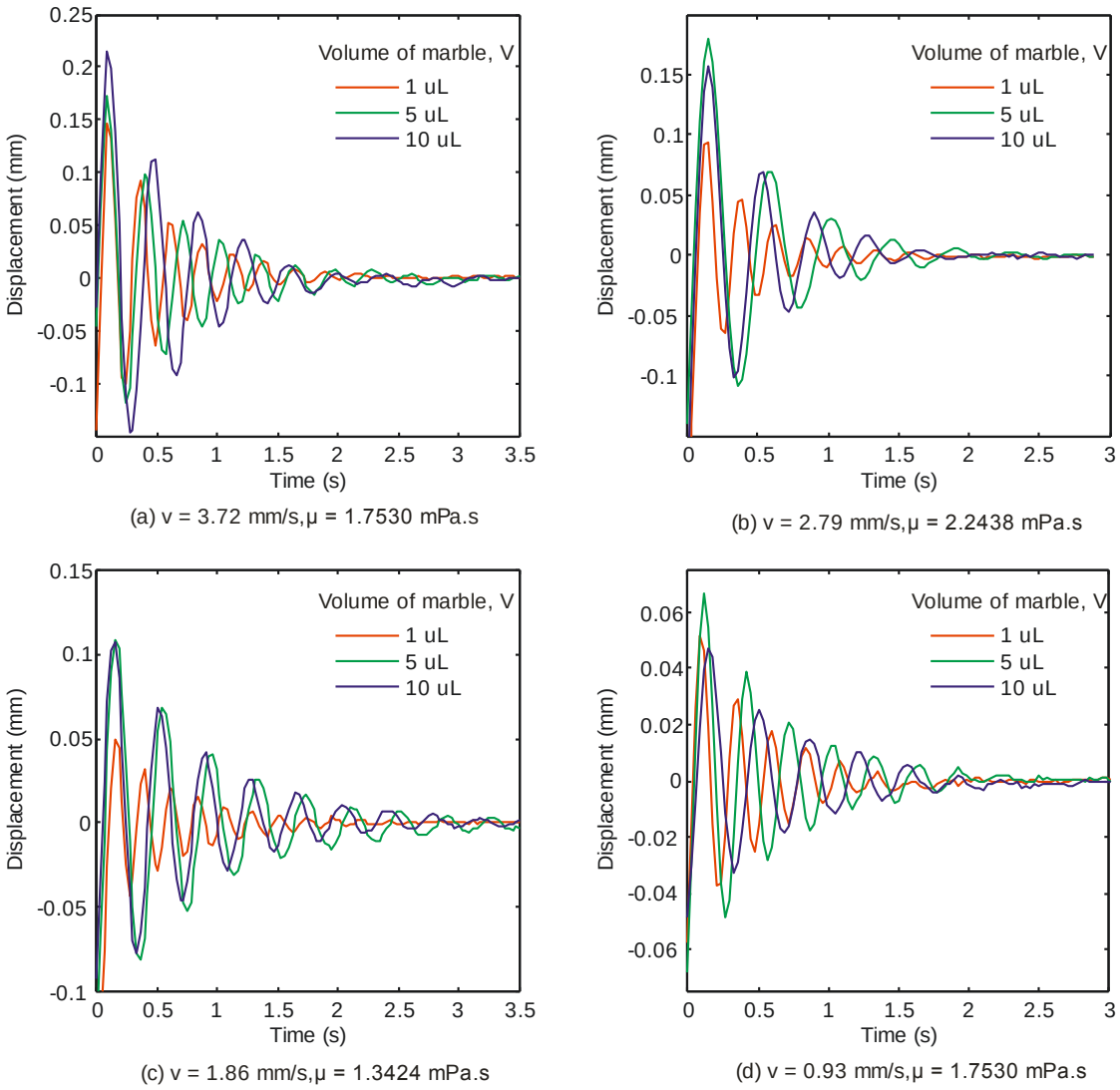

Figure 4.13: Damping graphs for liquid marble moving at (a) 3.72 mm/s in a medium containing 20.21% glycerol by weight (dynamic viscosity = 1.7530 mPa.s); (b) 2.79 mm/s in a medium containing 27.53% glycerol by weight (dynamic viscosity = 2.2438 mPa.s); (c) 1.86 mm/s in a medium containing 11.24% glycerol by weight (dynamic viscosity = 1.3424 mPa.s) and (d) 0.93 mm/s in a medium containing 20.21% glycerol by weight (dynamic viscosity = 1.7530 mPa.s); with varying volumes of 1μL, 5μL and 10μL.

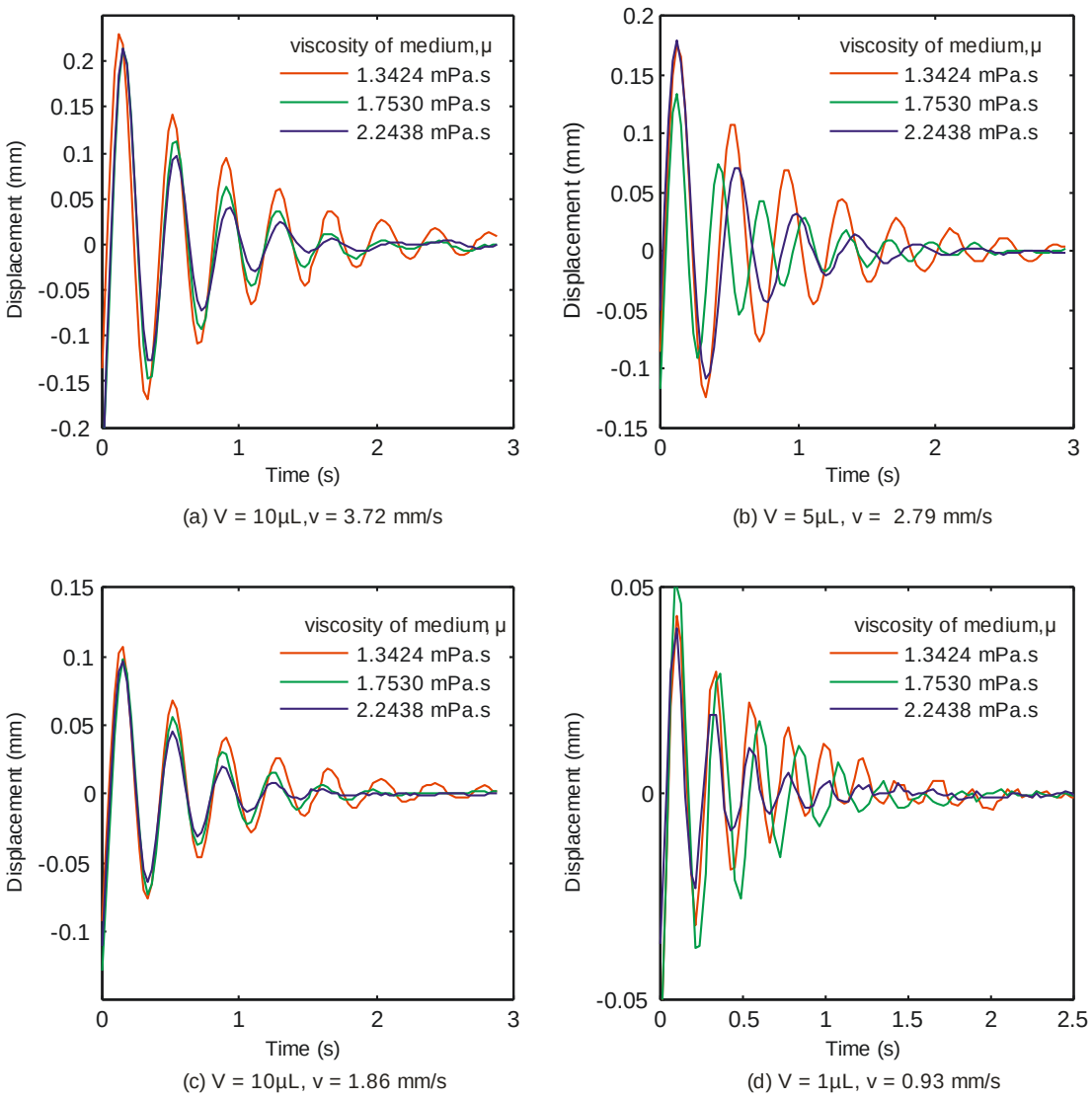

Figure 4.14: Damping graphs for (a) 10μL marble which was moving at 3.72 mm/s; (b) 5μL marble which was moving at 2.79 mm/s; (c) 10μL marble which was moving at 1.86 mm/s and (d) 1μL marble which was moving at 0.93 mm/s before it stops, in a medium with varying viscosity of 1.3424 mPa.s, 1.7530 mPa.s and 2.2438 mPa.s.

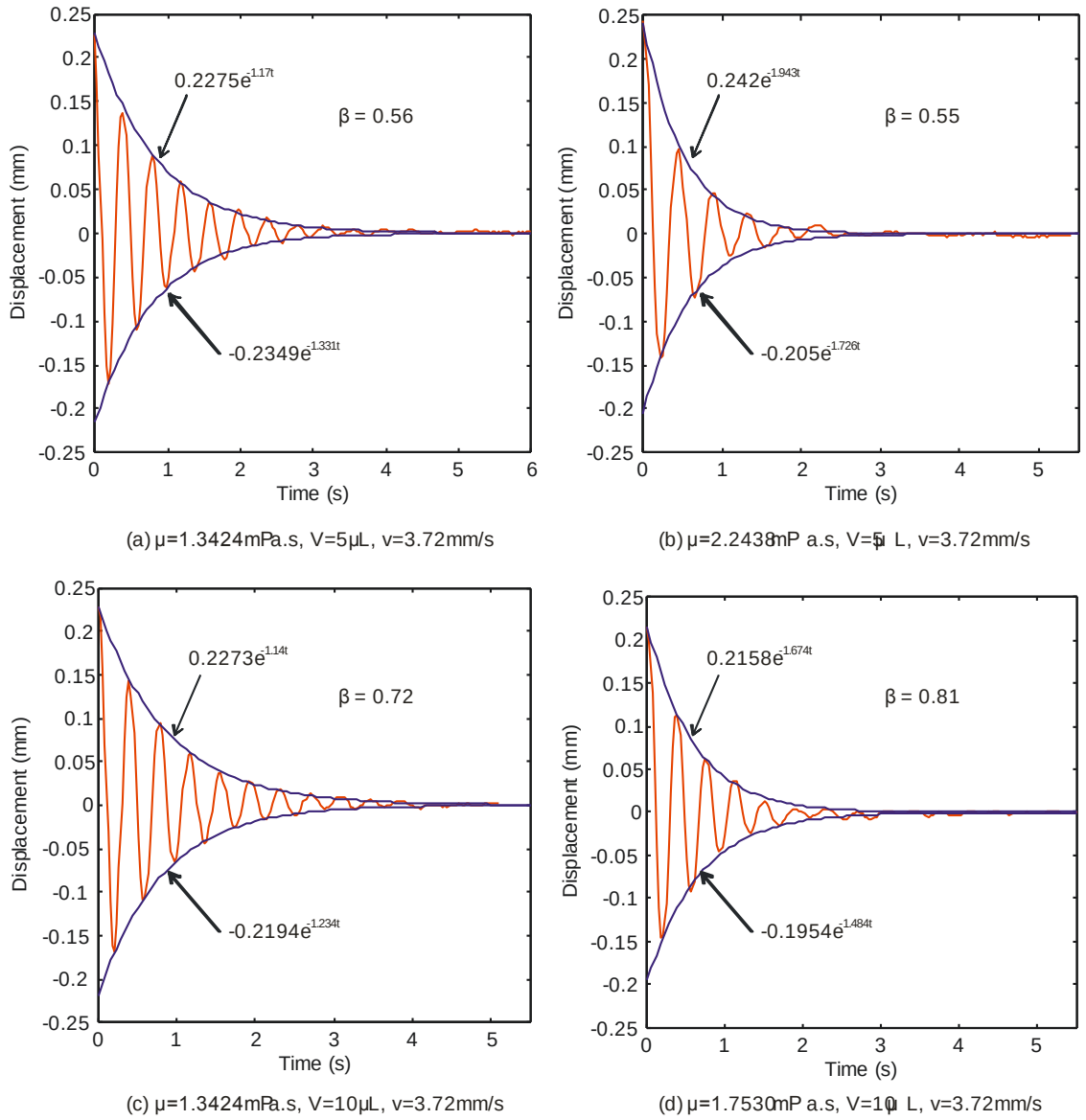

Figure 4.15: (Red): Damping graph of (a) 5μL marble with the speed of 3.72 mm/s floating on a medium with viscosity of 1.3424 mPa.s; (b) 5μL marble with the speed of 3.72 mm/s floating on a medium with viscosity of 2.2438 mPa.s; (c) 10μL marble with the speed of 3.72 mm/s floating on a medium with viscosity of 1.3424 mPa.s and (d) 10μL marble with the speed of 3.72 mm/s floating on a medium with viscosity of 1.7530 mPa.s; (Blue): (a-d) envelope of oscillation with the respective equations. Inset: value of the calculated friction correction factor, β.

Figure 4.15 shows the four damping graphs of a marble initially moving at a speed of 3.72 mm/s before the driving magnetic force was removed and the marble allowed to oscillate. The envelope of oscillation was plotted along the peaks and troughs of the damping graph and the exponential equation of the damping was found. Subsequently, we weighed the marble using a high precision analytical balance (Radwag, USA) with a resolution of 0.1 mg. Table 4.2 shows the measurements.

Table 4.2: Measured mass for three volumes of marble used in the experiments

Volume of marble (µL)	Mass (mg)	Radius (mm)
1	3.95 ± 0.30	1.05 ± 0.015
5	8.02 ± 0.11	1.33 ± 0.012
10	13.03 ± 0.10	1.63 ± 0.009

From equation (4.22), the term $ae^{-\frac{c}{2m}t}$ represents the envelope of oscillation. Thus, the value of *c* is calculated to be 18.77 for a 5 µL marble floating on water with 11.24% glycerol in weight (Figure 4.15(a)). From Table 4.1 and 4.2, given that the dynamic viscosity, μ is 1.3424 mPa.s and radius *r* is 1.33 mm, the values were inserted into equation (4.26). We determined the correction factor, β to be 0.56, which is quite similar to the values by Petkov et.al and Ooi et. al. The respective values of β of the other graphs (Figure 4.15(b-d)) are shown in the inset. By merging the equations (4.17) and (4.26), we got:

$$\beta = \frac{\gamma m}{3\pi r \mu} \qquad (4.28)$$

From equation (4.28), it is shown that the value of β was not dependent on the speed, *v* of the marble. When the viscosity, μ and volume of the marble, *V* are kept constant, the value of β had no significant changes when the speed is increased as shown in Figure 4.16.

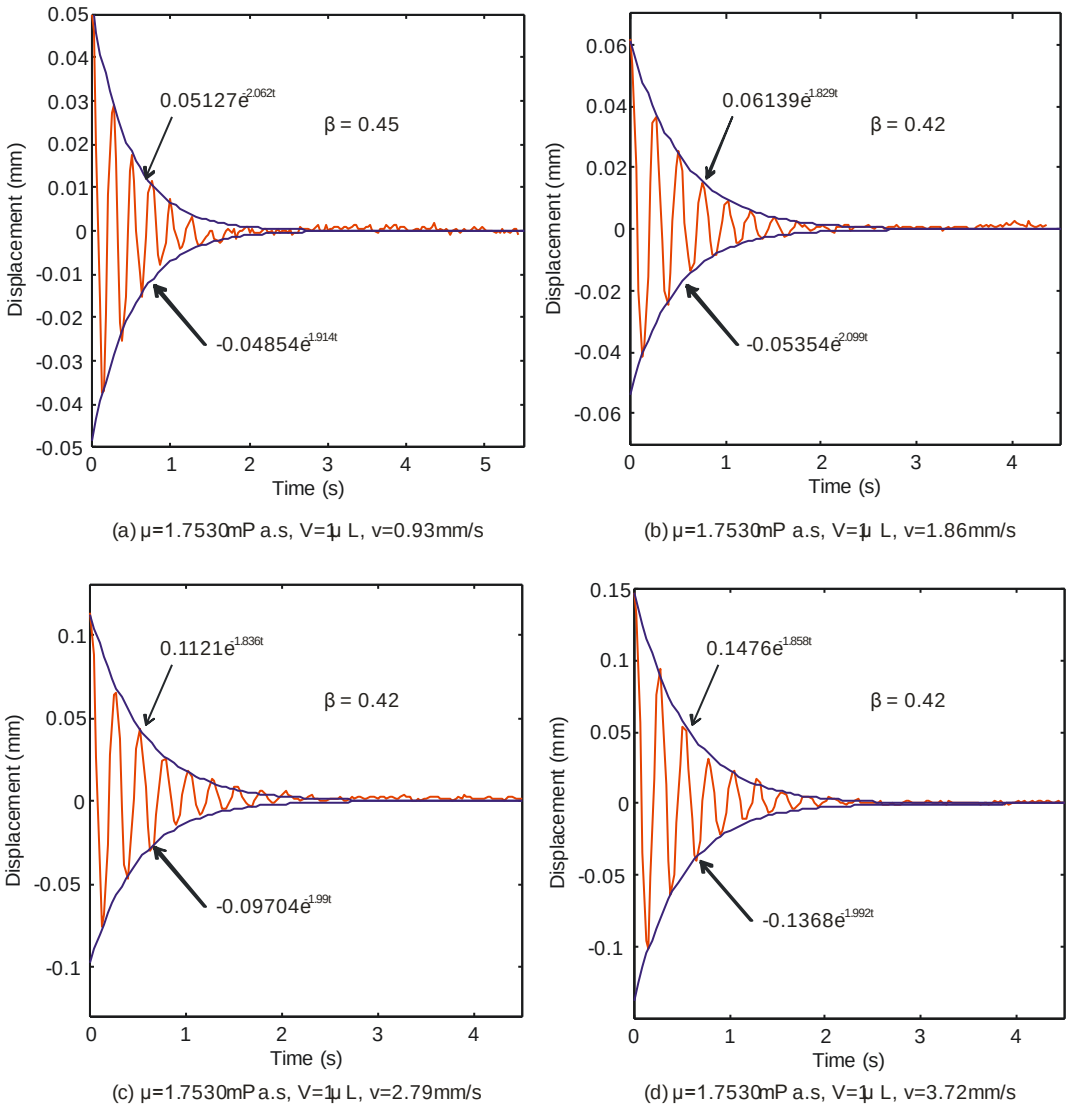

Figure 4.16: (Red): Damping graph of a 1μL marble floating on a medium with viscosity of 1.7530 mPa.s with a speed of (a) 0.93 mm/s; (b) 1.86 mm/s; (c) 2.79 mm/s and (d) 3.72 mm/s. (Blue): (a-d) envelope of oscillation with the respective equations. Inset: value of the calculated correction factor, β.

Using Fast Fourier transform for the analysis of the damping graphs in Matlab, the apparent frequencies, f and ω_1, were found. Figure 4.17 shows the graph obtained from the Fast Fourier transform and the value of the frequencies were shown. The magnetic force constant k was evaluated by inserting the value of ω_1 into equation (4.22). The average value of k of the system is 0.0030 N/m. As we had fixed the iron oxide concentration and the distance of the marble from the magnet in this experiment, we estimated quantitatively the value of the magnetic force by taking the driving force component from equation (4.18):

$$F_{magnetic} = kx \quad (4.29)$$

where x is the maximum amplitude of the oscillation. The magnetic force is estimated to be 0.34μN. From equations (4.23) and (4.24), the overall average damping ratio, ζ is 0.092 and the Q factor of the system is 5.46. The value of $\zeta < 0$ confirmed that the system is underdamped.

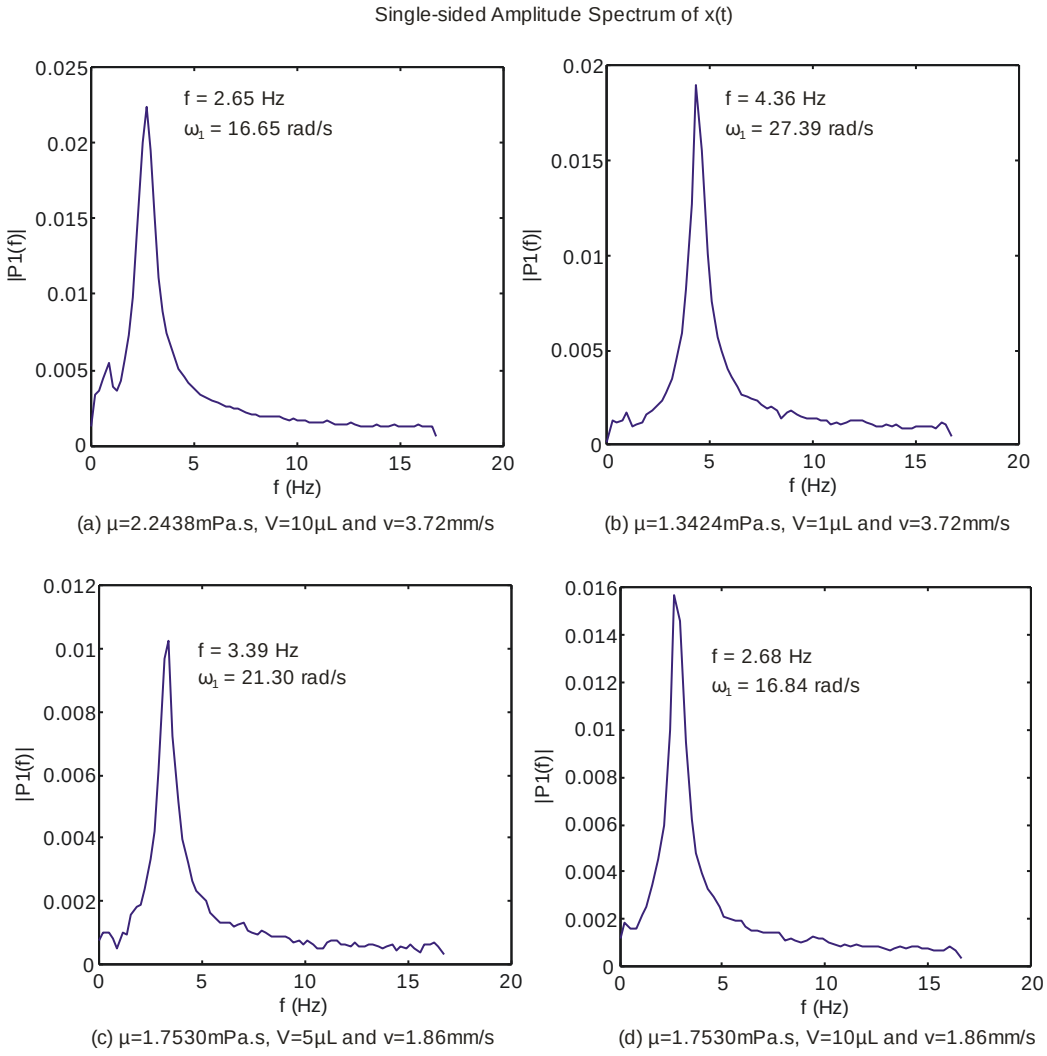

Figure 4.17: Apparent frequencies (f and ω_1) for marble with various viscosity, volume and speed.

The dynamics of the floating liquid marbles were governed by dimensionless numbers such as Bond number, Bo and capillary number, Ca. The Bond number compared the effects of gravity to surface tension forces. The Bond number of the marble is defined as:

$$Bo = \frac{\rho g r^2}{\sigma} \qquad (4.30)$$

where ρ is the density of marble containing deionised water (1000 kg/m^3), g is the gravitational acceleration, r is the radius of the marble and σ is the surface tension of the marble. Table 4.3 shows the calculated values.

Table 4.3: Bond number for three different volumes of the marble

Volume of marble, V (µL)	**Surface tension, σ (N/m) [129]**	**Radius of marble, r (m)**	**Bond number, Bo**
1	0.066	0.00105	0.16
5	0.078	0.00133	0.22
10	0.080	0.00163	0.33

The capillary number (*Ca*) represents viscous forces versus surface tension acting across the medium interface. The capillary number (*Ca*) is given by:

$$Ca = \frac{\mu v}{\sigma} \qquad (4.31)$$

where μ is the viscosity of the medium, v is the characteristic velocity/marble velocity and σ is the surface tension of the medium. Table 4.4 shows the calculated values.

Table 4.4: Capillary number for 3 different viscosities of the medium and 4 speeds of the marble

Viscosity, μ (mPa.s)	**Surface tension of the medium, σ (mN/m)**	**Characteristic velocity, v (mm/s)**	**Capillary number, Ca (x10^{-5})**
1.3424	71.30	0.93	1.75
		1.86	3.50
		2.79	5.25
		3.72	7.00
1.7530	70.93	0.93	2.30
		1.86	4.60
		2.79	6.90
		3.72	9.19
2.2438	70.35	0.93	2.97
		1.86	5.93
		2.79	8.90
		3.72	11.86

We relate the correction factor, β and the frequency of the damping system, f with the Bond number of the marble, *Bo* as shown in Figure 4.18(a) and 4.19(a). The fitting lines were estimated using the fitting functions (cftool from Matlab). The correction factor linearly

increased with *Bo*. This trend is consistent for all viscosities of the medium. However, the frequency decayed with the Bond number. From Figure 4.18(b) and 4.19(b), β and f remained almost constant with increasing speed or capillary numbers.

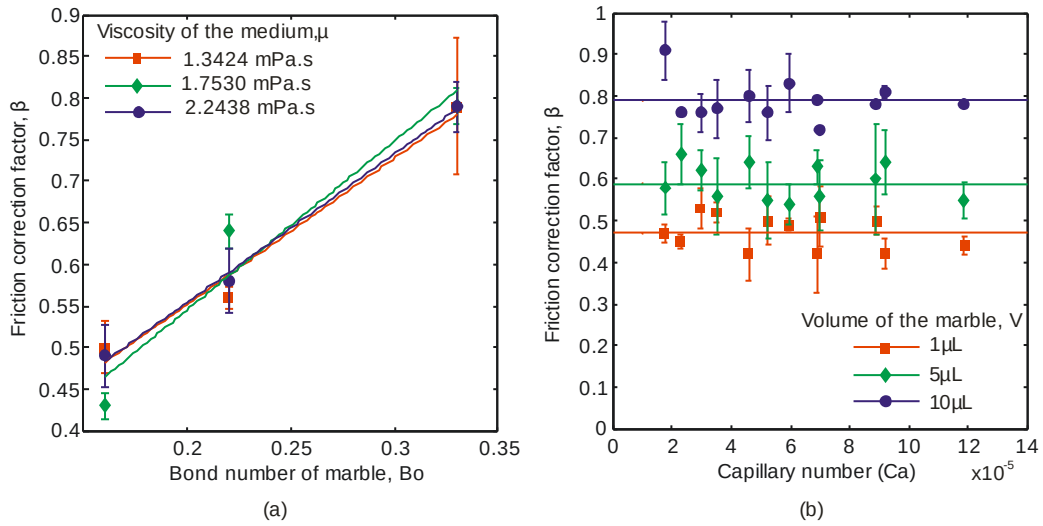

Figure 4.18: Relationship between the correction factor, β versus the Bond number, *Bo* and capillary number, *Ca*.

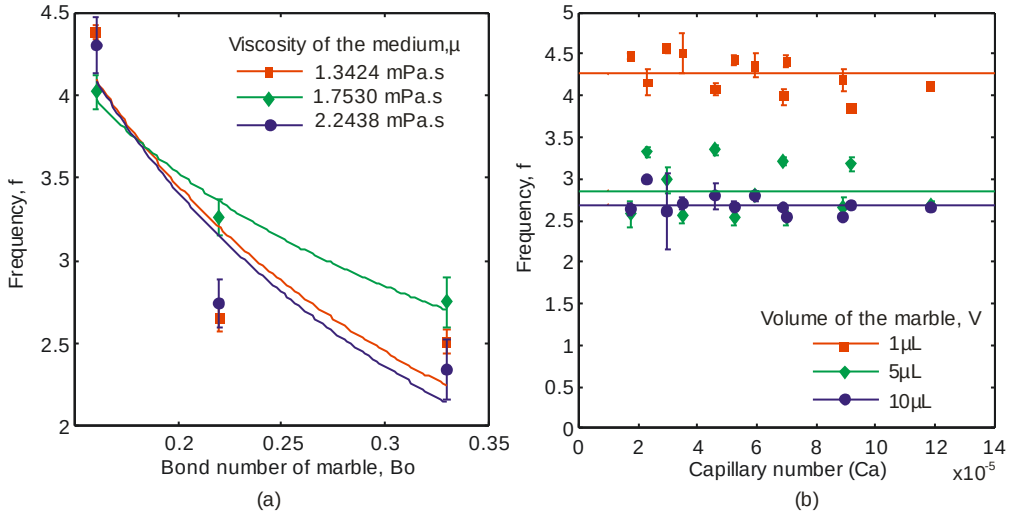

Figure 4.19: Relationship between the frequency of damping, *f* versus the Bond number, *Bo* and capillary number, *Ca*.

4.5 Conclusion

In this chapter, we had processed the raw data from the recording of the videos on the magnetic actuation of the droplets. Subsequently, significant graphs were plotted to summarise the motion of the droplets in relation to the theories that have been discussed. We will discuss the key findings of the experiments in Chapter 5.

Chapter 5: Discussions

5.1 Introduction

In Chapter 3, we had discussed about the experimental setups and methods for our experiments; one about mixing of reactive and unreactive droplets on a hydrophobic solid surface and another two were about the dynamics of floating liquid marbles on an aqueous solution. From the results and analyses of the graphs in Chapter 4, we will discuss about our findings in the following sections.

5.2 Magnetic actuation of droplet on a hydrophobic platform and merging of acid-base for calorimetric measurement

This work demonstrated the calorimetric measurement of magnetically actuated droplets. The mixing time of the two coalesced microdroplets were affected by the speed and the volume of the microdroplets. Based on the experimental data, the mixing time of HCl and NaOH reduced with increasing speed from 1.86 mm/s to 4.65 mm/s. The mixing time of the reactive microdroplets also decreased when the volume was reduced. These trends were similar for the non-reactive droplets. However, non-reactive droplets mixed at 7 to 12 times longer than the acid-base droplets. This finding is consistent with the work by Yeh et al. [45] in which their 0.2 µL- 0.5 µL reactive droplets mixing were 100 times more efficient than the nonreactive dye droplets. We also found that the peak temperature increased with speed and stabilised at the droplet size of 5 µL and 10 µL. The enthalpy values were calculated from the measured peak temperatures and were compared with the known HCl-NaOH enthalpy value of -57.7 kJ/mol [124]. There was a clear trend between increasing speed and the rise in δH. Moreover, the concentration of iron oxide in the movable droplet did not show any recognizable trend in relation to δH. From this micro calorimetric system, we conclude that the best conditions for the magnetically actuated mixing of two droplets that produce the exothermic reactions are a droplet volume of 5 µL and a high actuation speed of 4.65 mm/s.

5.3 Magnetic actuation for floating liquid marble on water

This work investigated experimentally the sliding motion of a magnetically actuated floating liquid marble. Using a permanent magnet, the movement of a floating liquid marble consisting of iron oxide was able to be controlled. While the shape and size of the permanent magnet were fixed, the concentration of iron oxide in the marble and the distance of the marble from the permanent magnet were varied. The key to a controlled movement is to supply adequate actuation force to oppose its frictional force, which are contributed by the velocity of the pulling

permanent magnet. In general, the suitable sliding condition is a low speed of the permanent magnet, a high magnetic flux density and a high concentration of magnetic particles in the floating liquid marble. The critical magnetic parameters and velocities derived from the scaling analysis fitted well to the experimental data describing the sliding region. Long et al. [29] and Nguyen et al. [42] have done similar studies on these motions but their platform were on an open hydrophobic surface.

5.4 Magnetic actuation on the damping of floating liquid marble on aqueous with different viscosity

This work studied the damping motion of a magnetically actuated floating liquid marble on aqueous of different viscosity. Using a stronger permanent magnet, the floating liquid marble was driven to move up to a specific speed before it was abruptly stopped. We observed the horizontal motion of the marble which was exponentially slowing down until it eventually stopped. While maintaining the vertical distance of the marble from the permanent magnet and iron oxide concentration in each liquid marble, the viscosity of the medium, speed and volume of the marble were varied. Experimental graphs showed a relation to the underdamped harmonic oscillation model. All the marbles oscillated and slowly return to its equilibrium and the amplitude decreased over time. At higher speed, the marble oscillated at higher amplitude and had no effect on the frequency of damping and the damping coefficient. At higher volume, the marble oscillated at higher amplitude, lower frequency of damping and higher damping coefficient. At higher viscosity of the medium, the marble oscillated at a higher damping coefficient and had no effect on the amplitude and the frequency of damping. Subsequently, we used the experimental data to evaluate the viscous damping coefficient, c, magnetic force constant, k to determine the friction correction factor, β and damping ratio, ζ. We determined the correction factor, β to be 0.56 at the volume of 5 μL, which is quite similar to the values by Petkov et.al [131] and Ooi et. al [24]. The average value of k of the system is 0.0030 N/m, the overall average damping ratio, ζ is 0.092 and the Q factor of the system is 5.46. We used the values to estimate the driving magnetic force. The magnetic force is estimated to be 0.34μN. We also related β and frequency of damping, f with the Bond number of the marble, Bo and capillary number of the medium, Ca. β linearly increased with Bo for all viscosities of the medium. However, f decayed with the Bond number. β and f remained almost constant with increasing speed or Ca.

Chapter 6: Conclusion and future works

The main study of this thesis is the magnetic actuation of droplets for digital microfluidic applications. We have done magnetic-actuation of droplets on two main platforms; superhydrophobic solid surface and droplet as a liquid marble floating on water and aqueous solutions of various viscosities.

In the literature, we have seen that magnetic actuation is an excellent controlled actuation choice because of the simplicity of using external magnetic field for a non-contact and non-invasive control over magnetised droplets. The facts that the magnetic field can penetrate through biological material, does not induce heating and is not affected by environmental chemical factors makes it more practical to be adopted in many biosensing and biomedical applications.

We can apply the findings of our experiment on the reactive microdroplet mixing on solid superhydrophobic surface as a conceptual model for an open chamber microcalorimeter. Due to the limitations of our laboratory, we could not investigate further on the thermodynamics of small molecule protein and ligand binding as part of the process in the fragment-based drug discovery. However, in our work, we found out that the parameters; speed and volume of the droplets, affected the mixing time and detection of heat of two coalesced reactive microdroplets. The concentration of magnetic particles in the droplets did not play a role in the improvement of the mixing time. We use this knowledge as a preliminary work to introduce a possible open chamber microcalorimeter platform. With a more precise and sensitive thermometry sensing, a good microcalorimeter platform could be materialised.

Floating liquid marble has a lot of potential in digital microfluidics due to its lower rate of evaporation and suitability of cell culture being its carrier liquid in the droplet. We studied about the horizontal forces; magnetic force and frictional force, which governed the dynamics of the floating liquid marble. We varied parameters such as magnetic flux density, flux density gradient, concentration of magnetic particles in the marble, speed of marble, volume of marble and viscosity of the medium to explain the relationship between the acting forces. By the estimation of the values of the forces, defining the operating regions for the sliding of the floating marble and deriving scaling laws, we can adopt the same rules for any magnetic manipulation with any system similar to our experimental platform.

For future work, we can look into incorporating a variety of manufactured magnetic particles into the floating liquid marble and study the effect of the particles with various carrier liquid such as chemical solutions and biological cultures.

References

[1] X.-M. Zhao, Y. Xia, and G. M. Whitesides, "Soft lithographic methods for nano-fabrication," *Journal of Materials Chemistry*, vol. 7, pp. 1069-1074, 1997.

[2] G. Luka, A. Ahmadi, H. Najjaran, E. Alocilja, M. DeRosa, K. Wolthers, *et al.*, "Microfluidics integrated biosensors: A leading technology towards lab-on-a-chip and sensing applications," *Sensors*, vol. 15, pp. 30011-30031, 2015.

[3] K. Choi, A. H. Ng, R. Fobel, and A. R. Wheeler, "Digital microfluidics," *Annual review of analytical chemistry*, vol. 5, pp. 413-440, 2012.

[4] M. Abdelgawad and A. R. Wheeler, "The digital revolution: a new paradigm for microfluidics," *Advanced Materials*, vol. 21, pp. 920-925, 2009.

[5] Y. Fouillet, D. Jary, C. Chabrol, P. Claustre, and C. Peponnet, "Digital microfluidic design and optimization of classic and new fluidic functions for lab on a chip systems," *Microfluidics and Nanofluidics*, vol. 4, pp. 159-165, 2008.

[6] W. Barthlott and C. Neinhuis, "Purity of the sacred lotus, or escape from contamination in biological surfaces," *Planta*, vol. 202, pp. 1-8, 1997.

[7] M. Nosonovsky and B. Bhushan, "Biologically inspired surfaces: broadening the scope of roughness," *Advanced Functional Materials*, vol. 18, pp. 843-855, 2008.

[8] P. Roach, N. J. Shirtcliffe, and M. I. Newton, "Progess in superhydrophobic surface development," *Soft matter*, vol. 4, pp. 224-240, 2008.

[9] E. Bormashenko, T. Stein, G. Whyman, Y. Bormashenko, and R. Pogreb, "Wetting properties of the multiscaled nanostructured polymer and metallic superhydrophobic surfaces," *Langmuir*, vol. 22, pp. 9982-9985, 2006.

[10] W. H. Koh, K. S. Lok, and N.-T. Nguyen, "A digital micro magnetofluidic platform for lab-on-a-chip applications," *Journal of Fluids Engineering*, vol. 135, p. 021302, 2013.

[11] P. Aussillous and D. Quéré, "Liquid marbles," *Nature*, vol. 411, pp. 924-927, 2001.

[12] E. Bormashenko, Y. Bormashenko, A. Musin, and Z. Barkay, "On the mechanism of floating and sliding of liquid marbles," *ChemPhysChem*, vol. 10, pp. 654-656, 2009.

[13] E. Bormashenko, R. Pogreb, Y. Bormashenko, A. Musin, and T. Stein, "New investigations on ferrofluidics: ferrofluidic marbles and magnetic-field-driven drops on superhydrophobic surfaces," *Langmuir*, vol. 24, pp. 12119-12122, 2008.

[14] E. Bormashenko, Y. Bormashenko, R. Grynyov, H. Aharoni, G. Whyman, and B. P. Binks, "Self-propulsion of liquid marbles: Leidenfrost-like levitation driven by Marangoni flow," *The Journal of Physical Chemistry C*, vol. 119, pp. 9910-9915, 2015.

[15] E. Bormashenko, Y. Bormashenko, and A. Musin, "Water rolling and floating upon water: marbles supported by a water/marble interface," *Journal of colloid and interface science*, vol. 333, pp. 419-421, 2009.

[16] M. Dandan and H. Y. Erbil, "Evaporation rate of graphite liquid marbles: comparison with water droplets," *Langmuir*, vol. 25, pp. 8362-8367, 2009.

[17] A. Tosun and H. Erbil, "Evaporation rate of PTFE liquid marbles," *Applied Surface Science*, vol. 256, pp. 1278-1283, 2009.

[18] J. Tian, N. Fu, X. D. Chen, and W. Shen, "Respirable liquid marble for the cultivation of microorganisms," *Colloids and Surfaces B: Biointerfaces*, vol. 106, pp. 187-190, 2013.

[19] R. K. Vadivelu, C. H. Ooi, R.-Q. Yao, J. T. Velasquez, E. Pastrana, J. Diaz-Nido, *et al.*, "Generation of three-dimensional multiple spheroid model of olfactory ensheathing cells using floating liquid marbles," *Scientific reports*, vol. 5, 2015.

[20] T. Arbatan, A. Al-Abboodi, F. Sarvi, P. P. Y. Chan, and W. Shen, "Tumor inside a pearl drop," *Advanced healthcare materials*, vol. 1, pp. 467-469, 2012.

[21] F. Sarvi, K. Jain, T. Arbatan, P. J. Verma, K. Hourigan, M. C. Thompson, *et al.*, "Cardiogenesis of Embryonic Stem Cells with Liquid Marble Micro-Bioreactor," *Advanced healthcare materials*, vol. 4, pp. 77-86, 2015.

[22] J. Tian, T. Arbatan, X. Li, and W. Shen, "Liquid marble for gas sensing," *Chemical Communications*, vol. 46, pp. 4734-4736, 2010.

[23] J. Tian, T. Arbatan, X. Li, and W. Shen, "Porous liquid marble shell offers possibilities for gas detection and gas reactions," *Chemical Engineering Journal*, vol. 165, pp. 347-353, 2010.

[24] C. H. Ooi, A. Van Nguyen, G. M. Evans, O. Gendelman, E. Bormashenko, and N.-T. Nguyen, "A floating self-propelling liquid marble containing aqueous ethanol solutions," *RSC Advances*, vol. 5, pp. 101006-101012, 2015.

[25] M. Paven, H. Mayama, T. Sekido, H. J. Butt, Y. Nakamura, and S. Fujii, "Light-Driven Delivery

and Release of Materials Using Liquid Marbles," *Advanced Functional Materials,* vol. 26, pp. 3199-3206, 2016.

[26] F. E. Torres, P. Kuhn, D. De Bruyker, A. G. Bell, M. V. Wolkin, E. Peeters, *et al.*, "Enthalpy arrays," *Proc Natl Acad Sci U S A,* vol. 101, pp. 9517-22, Jun 29 2004.

[27] M. I. Recht, D. De Bruyker, A. G. Bell, M. V. Wolkin, E. Peeters, G. B. Anderson, *et al.*, "Enthalpy array analysis of enzymatic and binding reactions," *Analytical Biochemistry,* vol. 377, pp. 33-39, Jun 1 2008.

[28] T. Roy, A. Sinha, S. Chakraborty, R. Ganguly, and I. K. Puri, "Magnetic microsphere-based mixers for microdroplets," *Physics of Fluids (1994-present),* vol. 21, p. 027101, 2009.

[29] Z. Long, A. M. Shetty, M. J. Solomon, and R. G. Larson, "Fundamentals of magnet-actuated droplet manipulation on an open hydrophobic surface," *Lab on a Chip,* vol. 9, pp. 1567-1575, 2009.

[30] D. De Bruyker, M. I. Recht, A. A. S. Bhagat, F. E. Torres, A. G. Bell, and R. H. Bruce, "Rapid mixing of sub-microlitre drops by magnetic micro-stirring," *Lab on a Chip,* vol. 11, pp. 3313-3319, 2011.

[31] L.-H. Lu, K. S. Ryu, and C. Liu, "A magnetic microstirrer and array for microfluidic mixing," *Microelectromechanical Systems, Journal of,* vol. 11, pp. 462-469, 2002.

[32] A. Egatz-Gómez, S. Melle, A. A. García, S. Lindsay, M. Márquez, P. Domínguez-García, *et al.*, "Discrete magnetic microfluidics," *Applied Physics Letters,* vol. 89, pp. 34106-34106, 2006.

[33] A. A. Garcia, A. Egatz-Gómez, S. A. Lindsay, P. Dominguez-Garcia, S. Melle, M. Marquez, *et al.*, "Magnetic movement of biological fluid droplets," *Journal of Magnetism and Magnetic Materials,* vol. 311, pp. 238-243, 2007.

[34] J. Schneider, A. Egatz-Gómez, S. Melle, S. Lindsay, P. Dominguez-Garcia, M. Rubio, *et al.*, "Motion of viscous drops on superhydrophobic surfaces due to magnetic gradients," *Colloids and Surfaces A: Physicochemical and Engineering Aspects,* vol. 323, pp. 19-27, 2008.

[35] S. K. Saroj, M. Asfer, A. Sunderka, and P. K. Panigrahi, "Two-fluid mixing inside a sessile micro droplet using magnetic beads actuation," *Sensors and Actuators A: Physical,* vol. 244, pp. 112-120, 2016.

[36] T. Ohashi, H. Kuyama, N. Hanafusa, and Y. Togawa, "A simple device using magnetic transportation for droplet-based PCR," *Biomedical microdevices,* vol. 9, pp. 695-702, 2007.

[37] N.-T. Nguyen, K. M. Ng, and X. Huang, "Manipulation of ferrofluid droplets using planar coils," *Applied Physics Letters,* vol. 89, p. 052509, 2006.

[38] N.-T. Nguyen, A. Beyzavi, K. M. Ng, and X. Huang, "Kinematics and deformation of ferrofluid droplets under magnetic actuation," *Microfluidics and Nanofluidics,* vol. 3, pp. 571-579, 2007.

[39] A. Beyzavi and N.-T. Nguyen, "Programmable two-dimensional actuation of ferrofluid droplet using planar microcoils," *Journal of micromechanics and microengineering,* vol. 20, p. 015018, 2009.

[40] A. Beyzavi and N.-T. Nguyen, "One-dimensional actuation of a ferrofluid droplet by planar microcoils," *Journal of Physics D: Applied Physics,* vol. 42, p. 015004, 2008.

[41] Y. Sun, Y. C. Kwok, and N.-T. Nguyen, "A circular ferrofluid driven microchip for rapid polymerase chain reaction," *Lab on a Chip,* vol. 7, pp. 1012-1017, 2007.

[42] N.-T. Nguyen, G. Zhu, Y.-C. Chua, V.-N. Phan, and S.-H. Tan, "Magnetowetting and sliding motion of a sessile ferrofluid droplet in the presence of a permanent magnet," *Langmuir,* vol. 26, pp. 12553-12559, 2010.

[43] C. Almarcha, P. M. Trevelyan, P. Grosfils, and A. De Wit, "Chemically driven hydrodynamic instabilities," *Physical review letters,* vol. 104, p. 044501, 2010.

[44] K. Tsuji and S. C. Müller, "Chemical reaction evolving on a droplet," *The journal of physical chemistry letters,* vol. 3, pp. 977-980, 2012.

[45] S.-I. Yeh, H.-J. Sheen, and J.-T. Yang, "Chemical reaction and mixing inside a coalesced droplet after a head-on collision," *Microfluidics and Nanofluidics,* vol. 18, pp. 1355-1363, 2015.

[46] J. Voldman, M. L. Gray, and M. A. Schmidt, "Microfabrication in biology and medicine," *Annual review of biomedical engineering,* vol. 1, pp. 401-425, 1999.

[47] L. J. Lee W, Koh J, "Development and applications of chip calorimeters as novel biosensors," *Nanobiosensors in Disease Diagnosis,* vol. 2012:1, pp. 17-29, 2012.

[48] M. W. Freyer and E. A. Lewis, "Isothermal titration calorimetry: Experimental design, data analysis, and probing Macromolecule/Ligand binding and kinetic interactions," *Biophysical Tools for Biologists: Vol 1 in Vitro Techniques,* vol. 84, pp. 79-113, 2008.

[49] T. Maskow and H. Harms, "Real time insights into bioprocesses using calorimetry: state of the art and potential," *Engineering in Life Sciences,* vol. 6, pp. 266-277, 2006.

[50] E. A. Johannessen, J. M. Weaver, L. Bourova, P. Svoboda, P. H. Cobbold, and J. M. Cooper,

"Micromachined nanocalorimetric sensor for ultra-low-volume cell-based assays," *Analytical chemistry*, vol. 74, pp. 2190-2197, 2002.

[51] J. Lerchner, A. Wolf, and G. Wolf, "Recent developments in integrated circuit calorimetry," *Journal of thermal analysis and calorimetry*, vol. 57, pp. 241-251, 1999.

[52] J. Xu, R. Reiserer, J. Tellinghuisen, J. P. Wikswo, and F. J. Baudenbacher, "A microfabricated nanocalorimeter: design, characterization, and chemical calibration," *Analytical chemistry*, vol. 80, pp. 2728-2733, 2008.

[53] E. Chancellor, J. Wikswo, F. Baudenbacher, M. Radparvar, and D. Osterman, "Heat conduction calorimeter for massively parallel high throughput measurements with picoliter sample volumes," *Applied physics letters*, vol. 85, pp. 2408-2410, 2004.

[54] W. Lee, W. Fon, B. W. Axelrod, and M. L. Roukes, "High-sensitivity microfluidic calorimeters for biological and chemical applications," *Proceedings of the National Academy of Sciences*, August 24, 2009 2009.

[55] Y. Zhang and S. Tadigadapa, "Calorimetric biosensors with integrated microfluidic channels," *Biosensors and Bioelectronics*, vol. 19, pp. 1733-1743, 2004.

[56] V. Baier, R. Födisch, A. Ihring, E. Kessler, J. Lerchner, G. Wolf, *et al.*, "Highly sensitive thermopile heat power sensor for micro-fluid calorimetry of biochemical processes," *Sensors and Actuators A: Physical*, vol. 123, pp. 354-359, 2005.

[57] M. Zieren, R. Willnauer, and J. Köhler, "Flow-through chip calorimeter based on BiSb/Sb-thin-film thermopiles with a thermopower of 64 mV/K," in *Micro Total Analysis Systems 2000*, 2000, pp. 71-74.

[58] L. Wang, D. M. Sipe, Y. Xu, and Q. Lin, "A MEMS thermal biosensor for metabolic monitoring applications," *Microelectromechanical Systems, Journal of*, vol. 17, pp. 318-327, 2008.

[59] B. Davaji, H. J. Bak, W.-J. Chang, and C. H. Lee, "A novel on-chip three-dimensional micromachined calorimeter with fully enclosed and suspended thin-film chamber for thermal characterization of liquid samples," *Biomicrofluidics*, vol. 8, p. 034101, 2014.

[60] B.-S. Kwak, B.-S. Kim, H.-H. Cho, J.-S. Park, and H.-I. Jung, "Dual Micro-Thermopile Based Biocalorimeter for Enzyme-Substrate Reaction," in *Sensors, 2007 IEEE*, 2007, pp. 740-743.

[61] H. Huth, A. Minakov, and C. Schick, "Differential AC-chip calorimeter for glass transition measurements in ultrathin films," *Journal of Polymer Science Part B: Polymer Physics*, vol. 44, pp. 2996-3005, 2006.

[62] G. Höhne, W. Hemminger, and H.-J. Flammersheim, *Differential scanning calorimetry*: Springer, 2003.

[63] P. Gill, T. T. Moghadam, and B. Ranjbar, "Differential scanning calorimetry techniques: applications in biology and nanoscience," *Journal of biomolecular techniques: JBT*, vol. 21, p. 167, 2010.

[64] H. Esfandyarpour and R. Davis, "An Integrated Differential Nanocalimeter with On-Chip Microfluidic Multiplexing for High Throughput Genomics and Proteomics," in *14th Int'l Conf. on Miniaturized Systems for Chem. And Life Sciences*, pp. 3-7.

[65] E. Zhuravlev and C. Schick, "Fast scanning power compensated differential scanning nano-calorimeter: 1. The device," *Thermochimica Acta*, vol. 505, pp. 1-13, 2010.

[66] B. Xie, M. Mecklenburg, B. Danielsson, O. Öhman, P. Norlin, and F. Winquist, "Development of an integrated thermal biosensor for the simultaneous determination of multiple analytes," *Analyst*, vol. 120, pp. 155-160, 1995.

[67] J. Lerchner, A. Wolf, G. Wolf, V. Baier, E. Kessler, M. Nietzsche, *et al.*, "A new micro-fluid chip calorimeter for biochemical applications," *Thermochimica Acta*, vol. 445, pp. 144-150, Jun 15 2006.

[68] L. M. Ahmad, B. Towe, A. Wolf, F. Mertens, and J. Lerchner, "Binding event measurement using a chip calorimeter coupled to magnetic beads," *Sensors and Actuators B-Chemical*, vol. 145, pp. 239-245, Mar 4 2010.

[69] J. Lerchner, T. Maskow, and G. Wolf, "Chip calorimetry and its use for biochemical and cell biological investigations," *Chemical Engineering and Processing: Process Intensification*, vol. 47, pp. 991-999, 2008.

[70] L. Wang, B. Wang, and Q. Lin, "Demonstration of MEMS-based differential scanning calorimetry for determining thermodynamic properties of biomolecules," *Sensors and Actuators B: Chemical*, vol. 134, pp. 953-958, 2008.

[71] B. Kwak, B. Kim, H. Cho, J. Park, and H. Jung, "Dual thermopile integrated microfluidic calorimeter for biochemical thermodynamics," *Microfluidics and Nanofluidics*, vol. 5, pp. 255-262, 2008.

[72] K. Verhaegen, K. Baert, J. Simaels, and W. Van Driessche, "A high-throughput silicon

microphysiometer," *Sensors and Actuators A: Physical*, vol. 82, pp. 186-190, 2000.
[73] C. Liu, "Recent developments in polymer MEMS," *Advanced Materials*, vol. 19, pp. 3783-3790, 2007.
[74] G. Voskerician, M. S. Shive, R. S. Shawgo, H. v. Recum, J. M. Anderson, M. J. Cima, *et al.*, "Biocompatibility and biofouling of MEMS drug delivery devices," *Biomaterials*, vol. 24, pp. 1959-1967, 2003.
[75] A. Neumann, T. Reske, M. Held, K. Jahnke, C. Ragoss, and H. Maier, "Comparative investigation of the biocompatibility of various silicon nitride ceramic qualities in vitro," *Journal of Materials Science: Materials in Medicine*, vol. 15, pp. 1135-1140, 2004.
[76] N.-T. Nguyen, "5 Fabrication Issues of Biomedical Micro Devices," in *BioMEMS and Biomedical Nanotechnology*, ed: Springer, 2007, pp. 93-115.
[77] J. R. Dorvee, A. M. Derfus, S. N. Bhatia, and M. J. Sailor, "Manipulation of liquid droplets using amphiphilic, magnetic one-dimensional photonic crystal chaperones," *Nat Mater*, vol. 3, pp. 896-9, Dec 2004.
[78] A. Del Campo and C. Greiner, "SU-8: a photoresist for high-aspect-ratio and 3D submicron lithography," *Journal of Micromechanics and Microengineering*, vol. 17, p. R81, 2007.
[79] S. K. Mitra and S. Chakraborty, *Microfluidics and Nanofluidics Handbook: fabrication, implementation, and applications* vol. 2: CRC Press, 2011.
[80] T.-Q. Truong and N.-T. Nguyen, "SU-8 On Pmma-A New Technology For Microfluidics," *International Journal of Computational Engineering Science*, vol. 4, pp. 667-670, 2003.
[81] H.-S. Noha, Y. Huangb, and P. J. Hesketha, "Parylene micromolding, a rapid and low-cost fabrication method for parylene microchannel," *Sensors and Actuators B: Chemical*, vol. 102, pp. 78-85, 2004.
[82] M. C. Bélanger and Y. Marois, "Hemocompatibility, biocompatibility, inflammatory and in vivo studies of primary reference materials low-density polyethylene and polydimethylsiloxane: A review," *Journal of biomedical materials research*, vol. 58, pp. 467-477, 2001.
[83] H. Bourbaba and B. Mohamed, "Mechanical behavior of polymeric membrane: comparison between PDMS and PMMA for micro fluidic application," *Energy Procedia*, vol. 36, pp. 231-237, 2013.
[84] H. Lorenz, M. Despont, N. Fahrni, N. LaBianca, P. Renaud, and P. Vettiger, "SU-8: a low-cost negative resist for MEMS," *Journal of Micromechanics and Microengineering*, vol. 7, p. 121, 1997.
[85] P. Abgrall, V. Conedera, H. Camon, A. M. Gue, and N. T. Nguyen, "SU-8 as a structural material for labs-on-chips and microelectromechanical systems," *Electrophoresis*, vol. 28, pp. 4539-4551, 2007.
[86] F. E. Torres, M. I. Recht, J. E. Coyle, R. H. Bruce, and G. Williams, "Higher throughput calorimetry: opportunities, approaches and challenges," *Current Opinion in Structural Biology*, vol. 20, pp. 598-605, Oct 2010.
[87] D. De Bruyker, M. Wolkin, M. Recht, F. Torres, A. Bell, G. Anderson, *et al.*, "MEMS-based enthalpy arrays," in *Solid-State Sensors, Actuators and Microsystems Conference, 2007. TRANSDUCERS 2007. International*, 2007, pp. 1757-1760.
[88] T. Instruments, "Nano ITC."
[89] D. De Bruyker, M. Recht, F. E. Torres, A. G. Bell, and R. H. Bruce, "Vanadium oxide thermal microprobes for nanocalorimetry," in *Sensors, 2010 IEEE*, 2010, pp. 2358-2362.
[90] A. Van Herwaarden and P. Sarro, "Thermal sensors based on the Seebeck effect," *Sensors and Actuators*, vol. 10, pp. 321-346, 1986.
[91] T. Hashimoto, J. Morikawa, T. Kurihara, and T. Tsuji, "Frequency dependent thermal diffusivity of polymers by temperature wave analysis," *Thermochimica acta*, vol. 304, pp. 151-156, 1997.
[92] J. Morikawa, C. Leong, T. Hashimoto, T. Ogawa, Y. Urata, S. Wada, *et al.*, "Thermal conductivity/diffusivity of Nd3+ doped GdVO4, YVO4, LuVO4, and Y3Al5O12 by temperature wave analysis," *Journal of Applied Physics*, vol. 103, p. 063522, 2008.
[93] D. G. Cahill, "Thermal conductivity measurement from 30 to 750 K: the 3ω method," *Review of Scientific Instruments*, vol. 61, pp. 802-808, 1990.
[94] L. Mahadevan, "Non-stick water," *Nature*, vol. 411, pp. 895-896, 2001.
[95] P. Aussillous and D. Quéré, "Properties of liquid marbles," in *Proceedings of the Royal Society of London A: Mathematical, Physical and Engineering Sciences*, 2006, pp. 973-999.
[96] G. McHale, D. Herbertson, S. Elliott, N. Shirtcliffe, and M. Newton, "Electrowetting of nonwetting liquids and liquid marbles," *Langmuir*, vol. 23, pp. 918-924, 2007.
[97] L. Gao and T. J. McCarthy, "Ionic liquid marbles," *Langmuir*, vol. 23, pp. 10445-10447, 2007.
[98] M. K. Khaw, C. H. Ooi, F. Mohd-Yasin, R. Vadivelu, J. St John, and N.-T. Nguyen, "Digital

microfluidics with a magnetically actuated floating liquid marble," *Lab on a Chip,* vol. 16, pp. 2211-2218, 2016.
[99] N. Eshtiaghi, J. S. Liu, W. Shen, and K. P. Hapgood, "Liquid marble formation: spreading coefficients or kinetic energy?," *Powder Technology,* vol. 196, pp. 126-132, 2009.
[100] E. Bormashenko, R. Pogreb, G. Whyman, and A. Musin, "Surface tension of liquid marbles," *Colloids and Surfaces A: Physicochemical and Engineering Aspects,* vol. 351, pp. 78-82, 2009.
[101] P. McEleney, G. Walker, I. Larmour, and S. Bell, "Liquid marble formation using hydrophobic powders," *Chemical Engineering Journal,* vol. 147, pp. 373-382, 2009.
[102] Y. Zhao, J. Fang, H. Wang, X. Wang, and T. Lin, "Magnetic liquid marbles: manipulation of liquid droplets using highly hydrophobic Fe3O4 nanoparticles," *Advanced materials,* vol. 22, pp. 707-710, 2010.
[103] E. Bormashenko, Y. Bormashenko, R. Pogreb, and O. Gendelman, "Janus droplets: liquid marbles coated with dielectric/semiconductor particles," *Langmuir,* vol. 27, pp. 7-10, 2010.
[104] G. McHale and M. I. Newton, "Liquid marbles: principles and applications," *Soft Matter,* vol. 7, pp. 5473-5481, 2011.
[105] G. McHale and M. Newton, "Liquid marbles: topical context within soft matter and recent progress," *Soft Matter,* vol. 11, pp. 2530-2546, 2015.
[106] E. Bormashenko, "Liquid marbles: properties and applications," *Current Opinion in Colloid & Interface Science,* vol. 16, pp. 266-271, 2011.
[107] E. Bormashenko, "New insights into liquid marbles," *Soft Matter,* vol. 8, pp. 11018-11021, 2012.
[108] C. H. Ooi and N.-T. Nguyen, "Manipulation of liquid marbles," *Microfluidics and Nanofluidics,* vol. 19, pp. 483-495, 2015.
[109] M. Newton, D. Herbertson, S. Elliott, N. Shirtcliffe, and G. McHale, "Electrowetting of liquid marbles," *Journal of Physics D: Applied Physics,* vol. 40, p. 20, 2006.
[110] E. Bormashenko, R. Balter, and D. Aurbach, "Micropump based on liquid marbles," *Applied Physics Letters,* vol. 97, p. 091908, 2010.
[111] M. Inoue, S. Fujii, Y. Nakamura, Y. Iwasaki, and S.-i. Yusa, "pH-responsive disruption of 'liquid marbles' prepared from water and poly (6-(acrylamido) hexanoic acid)-grafted silica particles," *Polymer journal,* vol. 43, pp. 778-784, 2011.
[112] S. Fujii, S. i. Yusa, and Y. Nakamura, "Stimuli-Responsive Liquid Marbles: Controlling Structure, Shape, Stability, and Motion," *Advanced Functional Materials,* vol. 26, pp. 7206-7223, 2016.
[113] E. Bormashenko, R. Pogreb, G. Whyman, A. Musin, Y. Bormashenko, and Z. Barkay, "Shape, vibrations, and effective surface tension of water marbles," *Langmuir,* vol. 25, pp. 1893-1896, 2009.
[114] E. Bormashenko and A. Musin, "Revealing of water surface pollution with liquid marbles," *Applied Surface Science,* vol. 255, pp. 6429-6431, 2009.
[115] E. Bormashenko, R. Pogreb, T. Stein, G. Whyman, M. Schiffer, and D. Aurbach, "Electrically deformable liquid marbles," *Journal of Adhesion Science and Technology,* vol. 25, pp. 1371-1377, 2011.
[116] Y. Zhao, Z. Xu, M. Parhizkar, J. Fang, X. Wang, and T. Lin, "Magnetic liquid marbles, their manipulation and application in optical probing," *Microfluidics and nanofluidics,* vol. 13, pp. 555-564, 2012.
[117] C. H. Ooi, E. Bormashenko, A. V. Nguyen, G. M. Evans, D. V. Dao, and N.-T. Nguyen, "Evaporation of ethanol-water binary mixture sessile liquid marbles," *Langmuir,* 2016.
[118] J. R. Dorvee, A. M. Derfus, S. N. Bhatia, and M. J. Sailor, "Manipulation of liquid droplets using amphiphilic, magnetic one-dimensional photonic crystal chaperones," *Nature Materials,* vol. 3, pp. 896-899, 2004.
[119] Y. Xue, H. Wang, Y. Zhao, L. Dai, L. Feng, X. Wang, *et al.*, "Magnetic liquid marbles: a "precise" miniature reactor," *Advanced materials,* vol. 22, pp. 4814-4818, 2010.
[120] L. Zhang, J. Wu, Y. Wang, Y. Long, N. Zhao, and J. Xu, "Combination of bioinspiration: a general route to superhydrophobic particles," *Journal of the American Chemical Society,* vol. 134, pp. 9879-9881, 2012.
[121] Y. Zhao, Z. Xu, H. Niu, X. Wang, and T. Lin, "Magnetic liquid marbles: Toward "lab in a droplet"," *Advanced Functional Materials,* vol. 25, pp. 437-444, 2015.
[122] N.-T. Nguyen, "Deformation of ferrofluid marbles in the presence of a permanent magnet," *Langmuir,* vol. 29, pp. 13982-13989, 2013.
[123] X. Han, H. K. Lee, W. C. Lim, Y. H. Lee, G. C. Phan-Quang, I. Y. Phang, *et al.*, "Spinning Liquid Marble and Its Dual Applications as Microcentrifuge and Miniature Localized

Viscometer," *ACS Applied Materials & Interfaces,* vol. 8, pp. 23941-23946, 2016.
[124] A. Zalts, C. El Hasi, D. Rubio, A. Urena, and A. D'Onofrio, "Pattern formation driven by an acid-base neutralization reaction in aqueous media in a gravitational field," *Physical Review E,* vol. 77, p. 015304, 2008.
[125] W. Sigmund, H. El-Shall, D. O. Shah, and B. M. Moudgil, *Particulate systems in nano-and biotechnologies*: CRC Press, 2008.
[126] D. E. Talbot and J. D. Talbot, *Corrosion Science and Technology*: CRC Press, 2010.
[127] T. R. Dulski, "A manual for the chemical analysis of metals," 1996.
[128] R. Cheng, G.-q. Li, C. Cheng, L. Shi, X. Zheng, and Z. Ma, "Catalytic oxidation of 4-chlorophenol with magnetic Fe 3 O 4 nanoparticles: mechanisms and particle transformation," *RSC Advances,* vol. 5, pp. 66927-66933, 2015.
[129] C. H. Ooi, C. Plackowski, A. V. Nguyen, R. K. Vadivelu, J. A. S. John, D. V. Dao, *et al.*, "Floating mechanism of a small liquid marble," *Scientific reports,* vol. 6, 2016.
[130] S. S. Shevkoplyas, A. C. Siegel, R. M. Westervelt, M. G. Prentiss, and G. M. Whitesides, "The force acting on a superparamagnetic bead due to an applied magnetic field," *Lab on a chip,* vol. 7, pp. 1294-1302, 2007.
[131] J. T. Petkov, N. D. Denkov, K. D. Danov, O. D. Velev, R. Aust, and F. Durst, "Measurement of the drag coefficient of spherical particles attached to fluid interfaces," *Journal of colloid and interface science,* vol. 172, pp. 147-154, 1995.
[132] N.-S. Cheng, "Formula for the viscosity of a glycerol-water mixture," *Industrial & engineering chemistry research,* vol. 47, pp. 3285-3288, 2008.
[133] G. P. Association, *Physical properties of glycerine and its solutions*: Glycerine Producers' Association, 1963.